THEORETICAL ANALYSIS OF ELECTRONIC, THERMAL, AND MECHANICAL
PROPERTIES IN GALLIUM OXIDE

By

Marco Domenico Santia

A DISSERTATION

Submitted to
Michigan State University
in partial fulfillment of the requirements
for the degree of

Electrical Engineering – Doctor of Philosophy

2019

ABSTRACT

THEORETICAL ANALYSIS OF ELECTRONIC, THERMAL, AND MECHANICAL PROPERTIES IN GALLIUM OXIDE

By

Marco Domenico Santia

In recent years, Ga_2O_3 has proven to be a promising semiconductor candidate for a wide array of power electronics and optoelectronics devices due to its wide bandgap, high breakdown voltage, and growth potential. However, the material suffers from a very low thermal conductivity and subsequent self-heating issues. Additionally, the complexity of the crystal structure coupled with the lack of empirical data, has restricted the predictive power of modelling material properties using traditional methods. The objective of this dissertation is to provide a detailed theoretical characterization of material properties in the wide bandgap semiconductor Ga_2O_3 using first-principles methods requiring no empirical inputs. Lattice thermal conductivity of bulk $\beta - Ga_2O_3$ is predicted using a combination of first-principles determined harmonic and anharmonic force constants within a Boltzmann transport formalism that reveal a distinct anisotropy and strong contribution to thermal conduction from optical phonon modes. Additionally, the quasiharmonic approximation is utilized to estimate volumetric effects such as the anisotropic thermal expansion.

To evaluate the efficacy of heat removal from $\beta - Ga_2O_3$ material, the thermal boundary conductance is computed within a variance-reduced Monte-Carlo framework utilizing first-principles determined phonon-phonon scattering rates for layered structures containing chromium or titanium as an adhesive layer between a $\beta - Ga_2O_3$ substrate and Au contact. The effect of the adhesive layer improves the overall thermal boundary conductance significantly with the maximum value found using a 5 nm layer of chromium, exceeding the more traditional titanium adhesive layers by a factor of 2. This indicates the potential of heatsink-based thermal management as an effective solution to the self-heating issue.

Additionally, this dissertation provides a detailed characterization of the effect of strain on fundamental material properties of $\beta-\mathrm{Ga_2O_3}$. Due to the highly anisotropic nature of the crystal, the effect strain can have on electronic, mechanical, and optical properties is largely unknown. Using the quasi-static formalism within a DFT framework and the stress-strain approach, the effect of strain can be evaluated and combined with the anisotropic thermal expansion to incorporate an accurate temperature dependence. It is found that the elastic stiffness constants do not vary significantly with temperature. The computed anisotropy is unique and differs significantly from similar monoclinic crystal structures, indicating the important role of the polyhedral linkage to the reported anisotropy in material properties. Lastly, the dependence of the dielectric function with respect to strain is evaluated using a modified stress-strain approach. This elasto-optic, or photoelastic, effect is found to be significant for sheared crystal configurations. This opens up a potential unexplored application space for $\mathrm{Ga_2O_3}$ as an acousto-optic modulation device.

TABLE OF CONTENTS

LIST OF TABLES

LIST OF FIGURES

CHAPTER 1

INTRODUCTION

In recent decades, there has been a tremendous surge of interest in the development of semiconducting material for use in a wide range of applications where silicon is not ideal. The majority of these applications consist of optoelectronics and high power electronics, where nanoscale devices are often implemented in integrated environments. Due to the limited performance of traditional semiconductors in these environments, the focus has shifted to wider band gap materials. The intrinsic electrical, thermal, and optical properties of wide bandgap materials provide several advantages for the engineering and minituarization of cutting edge electronic devices.

1.1   Ultra Wide Bandgap Semiconductors

The most popular materials for use in power electronic devices have been wide band gap (WBG) semiconductors such as the nitrides (GaN, AlN, InN, etc.) as well as SiC and ZnO. Wide band gaps are generally preferred for electronics applications as the large energy separation between valence and conduction band allow for higher temperatures of operation at higher voltages. Additionally, they can be used for many optical applications due to their large band gap which renders them transparent to visible light and often near-UV as well. While the traditional WBG semiconductors exhibit excellent properties in many instances they have several limitations in practice as well as in cost-effective fabrication [1]. This coupled with the increasing desire to find maximally large bandgap semiconductors has facilitated the development of ultra-wide bandgap materials which surpass the maximum breakdown voltages of even the nitrides. Leading this effort has been diamond, AlGaN, cubic BN, and Ga_2O_3 , the latter being the primary focus of this work. These materials surpass in many cases a 5 eV bandgap and can potentially allow for significantly improved performance for high power devices. An overview of the power and frequency ranges each
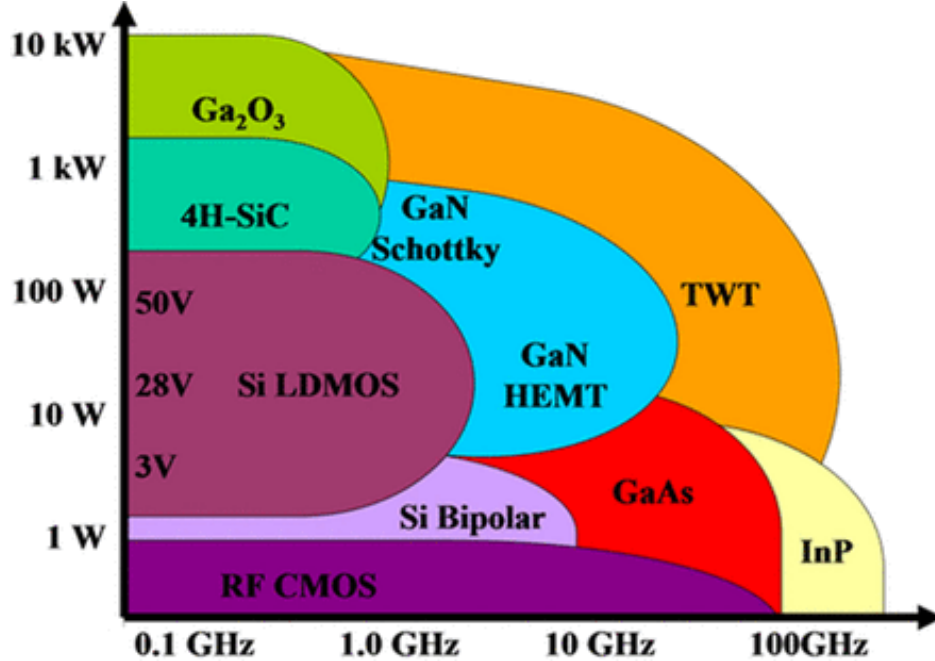
Figure 1.1: Application space for various frequencies of operation for common wide bandgap materials

Figure-of-Merit	Ge	Si	GaAs	4H-SiC	GaN	AlN	Diamond	Ga2O3
Johnson	1	5	7	63	83	375	167	200
Keyes	1	3	1	7	5	17	20	1
Baliga	1	7	106	2429	6220	459736	176282	24615
Huang (chip-area)	1	4	18	192	340	6053	2462	1109
Huang (high-temp)	1	0.35	0.07	0.01	0.01	0.00	0.00	0.00
Huang (material)	1	2	6	13	18	76	72	22

Table 1.1: Figure-of-Merit (FOM) numbers for a selection of primary semiconductor candidates used in electronic devices. All FOMs normalized to Ge. Data collected from [2].

material may provide optimal performance in, is presented in Figure 1.1

This trend is further characterized by one of many possible 'figure-of-merit' (FOM) parameters that can be used to estimate a semiconductors performance for a specific application. These FOM numbers are used to predict the future performance of a material in a new class of device technologies. The FOM numbers for the most prevalent candidates for semiconductor materials in future device designs are presented in Table 1.1. The focus of the work presented in this dissertation is on the last column, or Ga_2O_3 based devices. This
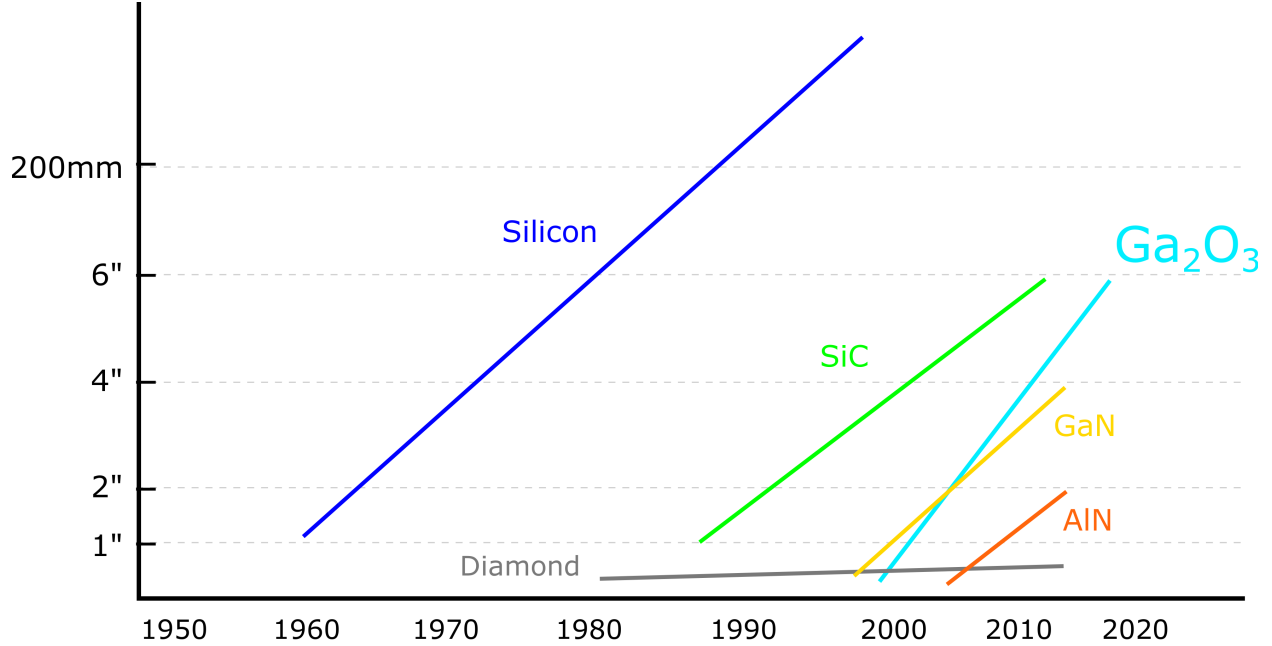
Figure 1.2: Timeline of crystal growth wafer sizes achieved for primary semiconductor materials used in device engineering.

material excels especially in the Baliga FOM, which characterizes the ability to minimize conduction losses and is expressed by,

$$\text{BFOM} = \epsilon \mu E_G^3 \tag{1.1}$$

The material claims a BFOM that is a factor of 3443 improved from silicon for example and a factor of 4 improvement over GaN. The primary advantage to Ga_2O_3 as a semiconductor over the other high-performing materials in the table such as Diamond and AlN, is the potential for commercial scalable growth beyond what any other wide bandgap material has achieved. Although the use of Ga_2O_3 in electronic devices only began within the last couple of decades, the progress made in developing larger wafers is unmatched. This trend is visualized in Figure 1.2. This compares favorably to other UWBG semiconductors such as Diamond which is generally considered to possess the most desirable material properties for electronics application. However, diamond still suffers from very limited growth potential with the largest wafers available only spanning a matter of millimeters even after many decades of research.

1.2 Gallium Oxide

Ga$_2$O$_3$ has long been studied due to its close relationship with sapphire and other poly-morphs of aluminum oxide. Interest in the material among the electronic device community has increased significantly in recent years, due to the wide array of applications. Some of these include power electronic devices, solar-blind UV photodetectors, gas sensors, and transparent conducting films of optoelectronic devices. Many of the applications stem from the wide bandgap and large window of optical transparency. The successful development of Ga$_2$O$_3$ transistors, such as MOSFETs and MESFETs [2], coupled with the low-cost and scalable growth using melt growth techniques has led to a surge of interest in this material.

The primary phase of interest has been the thermodynamically most stable phase, which is the monoclinic β phase. However there are actually five commonly identified polymorphs, labeled $\alpha, \beta, \gamma, \delta$ and ϵ. In this dissertation, I will focus primarily on the β phase but will also begin to explore the α phase as it has recently had success as an electronic device material in a metastable state. It also has exhibited some growth advantages over $\beta-$ Ga$_2$O$_3$, primarily owing to its higher degree of symmetry as will be discussed later. In both phases, the potential application space is large and the material has found success in nearly all the cases outlined in the previous section. Generally speaking, most of the critically important semiconductor device properties scale approximately exponentially with band gap and thus the 4.9eV band gap of Ga$_2$O$_3$ can find useful applications nearly anywhere that GaN or GaAs could. For example, Ga$_2$O$_3$ is optically transparent up to 250nm while remaining electrically conductive so it has found use as a window on optical devices [2]. In this section, I will briefly review the material properties of the α and β phases.

1.2.1   Beta Phase

Comparing to other commonly used wide bandgap (WBG) semiconductor materials, $\beta-$ Ga$_2$O$_3$ has a relatively complex crystal structure with low symmetry. The crystal structure
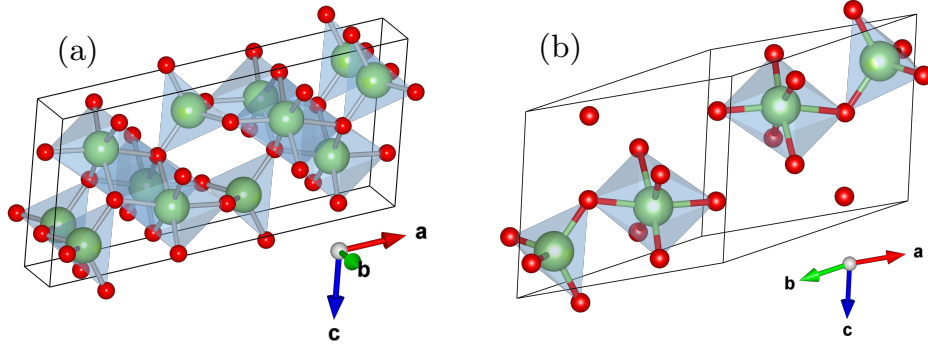
Figure 1.3: (left) Conventional monoclinic unit cell of $\beta - Ga_2O_3$ containing 20 atoms compared to the reduced primitive cell (right) containing 10 atoms. Note there exist two types of gallium atoms corresponding to the tetrahedral coordination and octahedral coordination which simultaneously exist in both unit cells.

for both the conventional unit cell and the reduced primitive cell are given in Figure 1.3. The β phase is base centered monoclinic (space group C2/m) with 20 atoms in the conventional cell and 10 in the primitive cell. In this symmetry, there are 3 unique crystallographic directions ($\vec{a}, \vec{b}$, and $\vec{c}$) as well as a monoclinic angle β between the $\vec{a}$ and $\vec{c}$ axes..

Interestingly, the β phase contains two unique species of gallium possessing different coordination numbers. There are both tetrahedral and octahedral coordinations labeled Ga(I) and Ga(II) respectively. This, in addition to the unique crystallographic directions, leads to anisotropy in the material properties. This anisotropy is important to characterize and will be considered throughout this work. Because of the reduced coordination of half the metal ions comparing to the α phase for example, which contains only octahedrally coordinated cations, the interatomic distances are relatively large. The closest nearest-neighbor length between two gallium cations is 3.04 Å.

To achieve electronic conduction, numerous types of dopants have been successfully used in $\beta - Ga_2O_3$ to achieve N-type conduction. Most commonly Si and Sn have been good shallow donors with small activation energies. Electron densities can be controlled between $10^{15} - 10^{19} cm^{-3}$ [2]. There has not however been any reported success with p-type doping, so hole conduction has not been realized which remains to be one of the materials largest bottlenecks. It is not generally expected that hole conduction will be improved by doping

due to the difficulty in finding acceptors with small activation energy given the very large bandgap of $\beta - \text{Ga}_2\text{O}_3$. This is a relatively common trend in WBG oxides such as ZnO, MgO, Ga_2O_3 and Al_2O_3 where the conduction band states come from metal atoms and the valence band states from O 2p orbitals. These orbitals present very large effective masses and small dispersion. Holes have been found to prefer localization in the form of polarons rather than in the form of free holes in the valence band [3].

The largest bottleneck $\beta - \text{Ga}_2\text{O}_3$ faces is the well known low thermal conductivity, or a high thermal resistance. This large thermal resistance coupled with the high temperatures of device operation in power electronics will lead to a localized thermal effects known as "self-heating". While the phenomena of self-heating is not a new concept, it has become an increasingly impassable obstacle in recent years due to the minituarization of devices. Unfortunately, $\beta - \text{Ga}_2\text{O}_3$ has a thermal conductivity an order of magnitude lower some of the other wide bandgap materials such as GaN, AlN and SiC. Comparing to another ultra wide bandgap material like diamond, which claims the highest known thermal conductivity, the issue can make the use of Ga_2O_3 very difficult in practice. This problem has gained much attention in the device engineering community as of recently and characterizing the details of the thermal behavior has become a crucial task for further improvements of Ga_2O_3 devices. The thermal conductivity has been a difficult quantity to measure in full due to the anisotropy of the crystal structure and subsequent material property tensors. Many precisely cut crystal orientations of high quality must be available for measurement to resolve a highly anisotropic tensor. This can be prohibitive due to the infancy of the crystals growth processes for Ga_2O_3 and the likely existence of residual strains that may effect the material properties.

1.2.2   Alpha Phase

The α phase of Ga_2O_3 is of rhombohedral, corundum, symmetry and is iso-structural to sapphire. The conventional unit cell presented in Figure 1.4. In this configuration, the oxygen ions are hexagonally closed-packed while gallium occupies two-thirds of the octahedral sites.
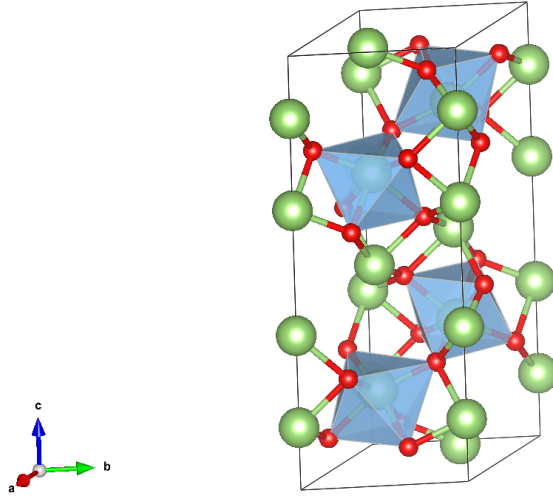
Figure 1.4: Crystal structure of conventional unit cell of $\alpha - \mathrm{Ga_2O_3}$

There are two independent lattice parameters $a = 4.98\,\text{Å}$ and $c = 13.43\,\text{Å}$. Recently, the α phase of $\mathrm{Ga_2O_3}$ has begun to be explored as a possible solution for limitations $\beta-\mathrm{Ga_2O_3}$ faces in device engineering. As mentioned previously, there has not been success in developing bipolar $\beta-\mathrm{Ga_2O_3}$ devices that can be manipulated from n-type to p-type. However, there has been success in other similar oxide semiconductors for use in pn junction heterostructures. Namely, $\alpha-\mathrm{Ir_2O_3}$ and $\alpha-\mathrm{Rh_2O_3}$, which both have exhibited p-type conductivity by the Seebeck effect [4] and possess the same symmetry as the α phase of $\mathrm{Ga_2O_3}$. Additionally, the bandgap of this phase is even larger than the β phase which leads to a larger breakdown voltage. This has motivated and led to preliminary success at device fabrication of bipolar $\alpha - \mathrm{Ga_2O_3}$ transistors [3].

Material properties of $\alpha - \mathrm{Ga_2O_3}$ are generally better than its $\beta - \mathrm{Ga_2O_3}$ counterpart for electronics applications. The bandgap of $\alpha - \mathrm{Ga_2O_3}$ is the largest of all the polymorphs of $\mathrm{Ga_2O_3}$ with a value of 5 eV increasing to over 5.16 eV for tin doped thin films [1]. Unlike the β phase, $\alpha-\mathrm{Ga_2O_3}$ is only metastable, however it can be maintained under ambient conditions unlike the other metastable phases of $\mathrm{Ga_2O_3}$. This phase can be produced by a transition of
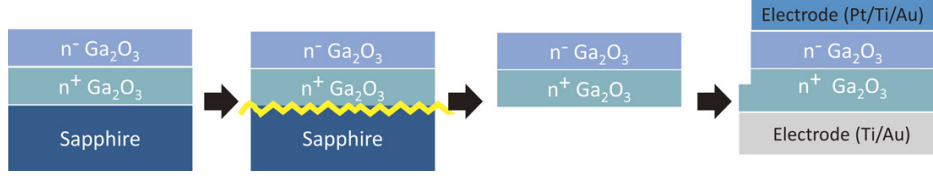
Figure 1.5: MIST Epitaxy of $\alpha - Ga_2O_3$ layers. Growth occurs on sapphire substrate and then is lifted-off [5]

the β phase under hydrostatic pressures at higher temperature. Experimentally, the phase transition has been observed at $P = 4.4$ GPa at high temperatures and at $P = 19.2$ GPa at cold compression [1]. Because of this, the ability to fabricate bulk crystals is prohibitive. All applications of $\alpha - Ga_2O_3$ are in thin-film form, grown in epitaxial layers on a sapphire substrate which then can be lifted off and isolated, or layered with another substrate, as illustrated in Figure 1.5. This offers a unique possibility to control thermal heat flux by means of more efficient heatsink thermal energy extraction. The thinner the layer and the lower the mismatch between layer and substrate, the more likely it becomes that a high thermal conductivity substrate will more rapidly dissipate heat. The sapphire Al_2O_3 substrate has the same crystal structure with only 4% lattice mismatch.

Overall, this phase is less understood than the β phase. Although the high bandgap is appealing, the difficult growth process can be prohibitive especially for measurements of bulk crystalline properties. Theoretical predictions of the material properties are the only option when the crystal cannot be easily isolated. Thus far, very few theoretical works have been performed for any optical, thermal or electronic properties of $\alpha - Ga_2O_3$.

1.3   Summary of Objectives

As mentioned previously, perhaps the most appealing benefits of several polymorphs of Ga_2O_3 is the potential for readily scalable bulk crystal growth by several possible methods. This has been the primary factor leading to the massive increase in Ga_2O_3 research in recent years [6]. However there is still not a clear picture of what the limitations of the material are and how they can be overcome. This leaves many open questions about how Ga_2O_3 compares

to other WBG semiconductors and how effective it could be in practice.

Experimentally, it is difficult to characterize thermal properties of ternary or doped structures due to the need to fabricate specific structures meant solely for thermal measurements. Additionally, a highly anisotropic material also can prove to be a challenge to accurately analyze due to the necessity of several high quality crystals grown in specific orientations to resolve the entire thermal conductivity tensor. Fortunately, there has been rapid developments in computational modelling of thermal transport properties in recent years. Reliable theoretical models that can extract spatial and temporal distributions of thermal gradients are beginning to become computationally feasible without any empirical inputs. First-principles methods of determining harmonic and anharmonic phonon properties in crystals systems of all symmetry classes is now possible [7]. This dissertation will seek to apply these new methods to Ga_2O_3 to further understand the thermal conductivity behavior and breakdown the origins of the high resistance. Additionally, the topic of thermal boundary conductance will be analyzed using recently developed Monte-Carlo methods to assess the viability of forming effective thermal contacts with Ga_2O_3 using higher thermal conductivity metals to reduce the self-heating effects. At the time of writing, these methods have not been rigorously tested for realistic device models, so this work will additionally serve to set a benchmark of the robustness of the variance reduced Monte-Carlo algorithm.

Understanding the origins of the reportedly low thermal conductivity is an essential tool for further refinement and management of the thermal properties. This has been a challenge for $\beta - Ga_2O_3$ due to the lack of fundamental knowledge of material mechanical and thermodynamic properties. For example, the elastic properties are mostly unknown for all phases of Ga_2O_3 . In general, elastic properties can reveal a significant amount of information about the material and can be linked to heat capacity, thermal expansion, phonon dispersion, Gruneisen parameters, melting points, etc. When engineering devices operating in a high temperature environment, the characterization of thermal expansion and overall thermodynamic stability is important to ensure reliability and efficiency. In this

9

dissertation, first-principles methods are used to evaluate the thermodynamic properties within a quasiharmonic approximation for phonons for a series of volumes of the unit cell. This methodology allows for a robust and accurate determination of fully anisotropic material properties which would otherwise be difficult to measure. Additionally, the effect that strain has on these fundamental properties can be more directly evaluated. Similarly, a significant portion of this work will focus on the predicted optical response properties such as dielectric function to supplement the understanding of the anisotropic properties of Ga_2O_3 -based opto-electronic devices such as solar-blind photo-detectors. Using this, the effect of mechanical strain on the system can be included and used to determine photo-elastic behavior of $\beta - Ga_2O_3$. The photo-elasticity is a difficult to measure quantity that provides a useful estimate of the optical behavior in a material known to undergo significant strain. These strains can appear as residual strains during crystal growth for example, and can lead to a high degree of birefringence even in the ideal bulk crystal.

CHAPTER 2

ELECTRONIC STRUCTURE

Understanding and predicting the properties of semiconductors through electronic transport requires an accurate description of the electronic band structure of the material. Historically, computation has relied on empirical models such as tight-binding and empirical pseudopotential methods which utilize experimentally determined parameters. These methods become infeasible as crystal complexity increases, as the necessary parameters are generally unavailable and difficult to extract from measurements. The alternative, and more predictive, approach is to utilize first-principles atomistic calculations to determine band structure and other transport properties. Specifically, density functional theory (DFT) using a planewave pseudopotential basis has demonstrated high accuracy with reasonable computational requirements. Although these methods have vastly increased computational overhead to empirical methods, they have proven themselves in recent years to be highly accurate without any need for measured data for considerably complex systems. This is especially important for a material as new and unrefined as Ga_2O_3 , where an improved understanding of the electronic properties at the atomic level can aid in the engineering of transport properties which directly influence device performance. The amount of information available on the electronic structure of this material is surprisingly limited and the exact nature of the bandgap is still not well understood. This is in part due to the complexity of the Brillouin zone which contains a very complex high symmetry path. Furthermore, $\beta - Ga_2O_3$ is known to possess a significant anisotropy in both electrical and optical properties, with the former largely attributed to an anisotropic effective mass and the latter due to band-to-band selection rules.

Throughout this work the QuantumEspresso [8] package will be utilized for the electronic structure calculations. The majority of the DFT calculations utilize the generalized gradient approximation (GGA) with projector augmented wave (PAW) potentials. At times however

the local density approximation (LDA) is also utilized and compared to as the former is known to overestimate the lattice constant and subsequently the cell volume. For specifically electronic structure, GGA is generally considered more accurate [8] and will be used for the exchange-correlation functional with the PAW potentials used to represent the interaction between ionic cores and valence electrons. The kinetic energy cutoff for Kohn-Sham planewave basis is 125 Ry and typical Brillouin zone integrations are performed on a 8x8x4 grid. Structural relaxation is performed on a more dense grid with 16x16x8 to ensure the forces between atoms are properly minimized. This step is important when extending the DFT calculation to phonons, where there is a greater sensitivity to residual forces.

2.1 Atomic Structure

In the case of $\beta - \mathrm{Ga_2O_3}$ there is a mixed bonding character between the gallium ions as mentioned previously. They occupy both tetrahedral and octahedral sites while the oxygen ions form a distorted cubic packing structure with the unique sites comprising two threefold coordinated and one fourfold coordinated [9]. This mixed bonding character leads to chemical bonds which exhibit both covalent and ionic bonding characteristics and are heavily directionally-dependent (anisotropic). This anisotopy has been realized geometrically and in measurements of the electrical conductivity tensor [2].

The geometry of the β phase is more complex and can be represented by its monoclinic conventional cell or reduced primitive cell with lattice parameters a, b, c and β which is the angle between a and c. The lattice vectors for the conventional unit cell are expressed in the traditional form [9] by

$$\mathbf{a}_1^{\mathrm{conv}} = a\hat{\mathbf{x}} + 0\hat{\mathbf{y}} + 0\hat{\mathbf{z}}$$

$$\mathbf{a}_2^{\mathrm{conv}} = 0\hat{\mathbf{x}} + b\hat{\mathbf{y}} + 0\hat{\mathbf{z}}$$

$$\mathbf{a}_3^{\mathrm{conv}} = c\cos\beta\hat{\mathbf{x}} + 0\hat{\mathbf{y}} + c\sin\beta\hat{\mathbf{z}}$$

and the primitive cell transformation is mapped in the following way

$$\mathbf{a}_1^{\text{prim}} = (\mathbf{a}_1^{\text{conv}} + \mathbf{a}_2^{\text{conv}})/2$$

$$\mathbf{a}_2^{\text{prim}} = (-\mathbf{a}_1^{\text{conv}} + \mathbf{a}_2^{\text{conv}})/2$$

$$\mathbf{a}_3^{\text{prim}} = \mathbf{a}_3^{\text{conv}}$$

The detailed parameters of the crystal structures after geometric relaxation for both LDA and GGA functionals for the β-phase is provided in Table 2.1.

	Expt[10]	GGA	LDA
a	12.23	12.41	12.26
b	3.04	3.07	3.04
c	5.80	5.86	5.81
β	103.82	103.72	103.75

Table 2.1: Lattice parameters for $\beta - \text{Ga}_2\text{O}_3$ used in DFT calculations for LDA and GGA compared with experimental values

It is crucial to provide clarity on the shape of the Brillouin zone (BZ) as there has not been a consistent convention adopted in past literature [9]. This is attributed to the flexibility in how the axes of a monoclinic crystal are assigned. This topic was recently clarified in detail in [9] where it was determined that some inconsistency has arisen due to the non interchangeable BZs of the primitive and conventional cells. Essentially, it was found that the smallest parallelpiped of the reciprocal lattice vectors of the conventional cell actually contain a smaller volume than the analog in the primitive cell. This is a non-intuitive result that leads to an irreducible BZ of the primitive cell which does not fully span reciprocal space when performing calculations on the conventional cell. This is contrary to higher symmetry crystal structures and here, the BZ of the primitive and conventional cell must be considered independently of one another for consistency. In general the monoclinic system can be represented by one of five unique BZ shapes depending on the choice of base-centering (*c*-base centered or *b*-base centered). In this work, the *b*-axis is used as the dyadic axis so it is *b*-base centered, leading to the spacegroup symbol C2/m. The full BZ is presented in
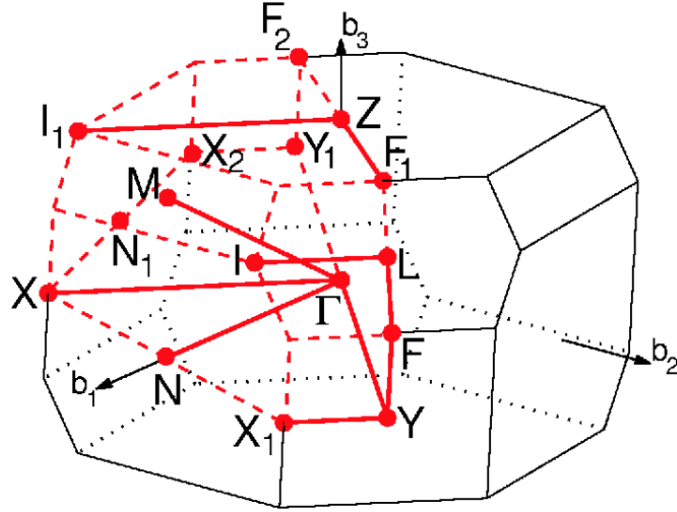
Figure 2.1: Brillouin zone for monoclinic $\beta-\text{Ga}_2\text{O}_3$ (spacegroup C2/m) with high symmetry points labelled

Figure 2.1 with high symmetry points and path labelled for clarity. The high-symmetry path used in this BZ was constructed in [9] intentionally to ensure a high symmetry path which avoids discontinuities.

The α phase of Gallium Oxide is a simpler crystal structure possessing a trigonal symmetry in the form of a rhombohedral lattice, spacegroup $R3c$ which can also be expressed in hexagonal coordinates. The conventional unit cell can be composed as a series of six formula units totalling 30 atoms of nearly closed packed ABAB stacking of the oxygen anions. The gallium ions meanwhile occupy two-thirds of the octahedral interstitial along the [0001] direction. The primitive unit cell can be simplified to two formula units totalling ten atoms as shown in Figure 2.2. The crystal has the same structure as sapphire, which is the α phase of Aluminum Oxide (Al_2O_3). This structure is well known and has been researched extensively so there is significantly more literature to compare to than $\beta - \text{Ga}_2\text{O}_3$. The form of the lattice which is typically adopted requires the z axis to be aligned parallel to the rhombohedral $\langle 111 \rangle$ direction which is the c-axis if using the hexagonal representation
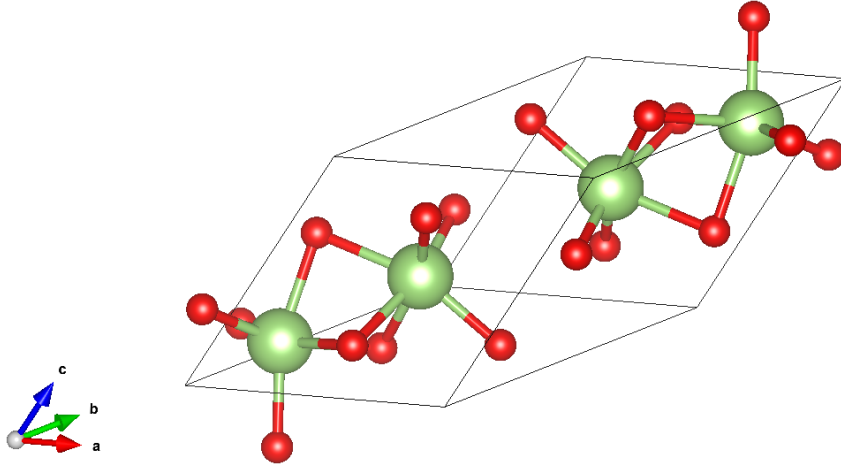
Figure 2.2: Rhombohedral primitive unit cell for $\alpha - \mathrm{Ga_2O_3}$ consisting of 10 atoms. All gallium cations in this phase are octahedrally coordinated.

of the rhombohdral lattice. The lattice vectors can be expressed as

$$
\begin{aligned}
\mathbf{a}_1 &= \left(0, \sqrt{3}a_{\mathrm{hex}}/3, c_{\mathrm{hex}}/3\right) \\
\mathbf{a}_2 &= \left(-a_{\mathrm{hex}}/2, -\sqrt{3}a_{\mathrm{hex}}/6, c_{\mathrm{hex}}/3\right) \\
\mathbf{a}_3 &= \left(a_{\mathrm{hex}}/2, -\sqrt{3}a_{\mathrm{hex}}/6, c_{\mathrm{hex}}/3\right)
\end{aligned}
\tag{2.1}
$$

In this definition, the lattice parameters can be defined in terms of the rhombohedral lattice constant a and subsequent angle α,

$$
\begin{aligned}
a_{\mathrm{hex}} &= a\sqrt{2(1 - \cos\alpha)} \\
c_{\mathrm{hex}} &= a\sqrt{3(1 + 2\cos\alpha)}
\end{aligned}
$$

The lattice parameters for this phase are provided in Table 2.2 with a corresponding Brillouin zone given by the shape in Figure 2.3.

15

	Expt.[10]	GGA	LDA
a	5.321	5.4	5.31
a_{hex}	4.97	5.10	4.99
c_{hex}	13.43	13.64	13.41
$\alpha(°)$	55.79	55.87	55.93

Table 2.2: Lattice parameters in the hexagonal phase for $\alpha-Ga_2O_3$ used in DFT calculations for LDA and GGA compared with experimental values. All values provided in Angstroms.
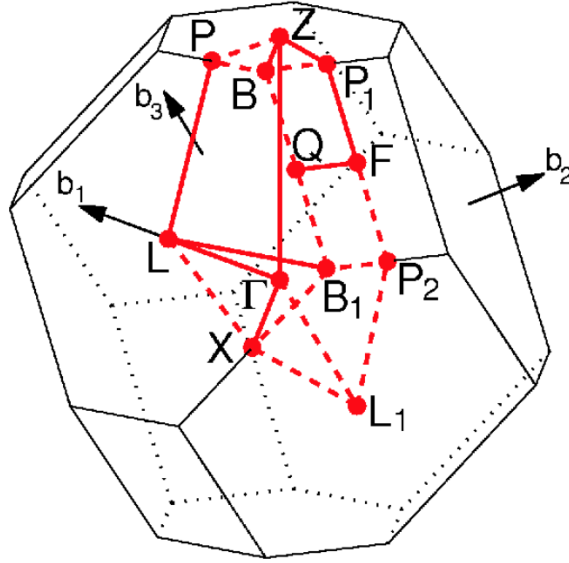
Figure 2.3: Rhombohedral Brillouin zone for $\alpha - Ga_2O_3$ with high symmetry points

2.2 Band Structure

It is well known that planewave DFT computations of electronic structure fail to resolve an accurate bandgap between the lowest conduction band and highest valence band. This is due to the inability of traditional DFT to incorporate the electron number density dependence in the exchange-correlation functional term. The details of this restriction are beyond the scope of this work and are explained in detail in [11]. However, as the materials of interest are semiconducting, the bandgap is a key parameter and must be kept in mind when comparing measurements to DFT calculations. The experimental room-temperature
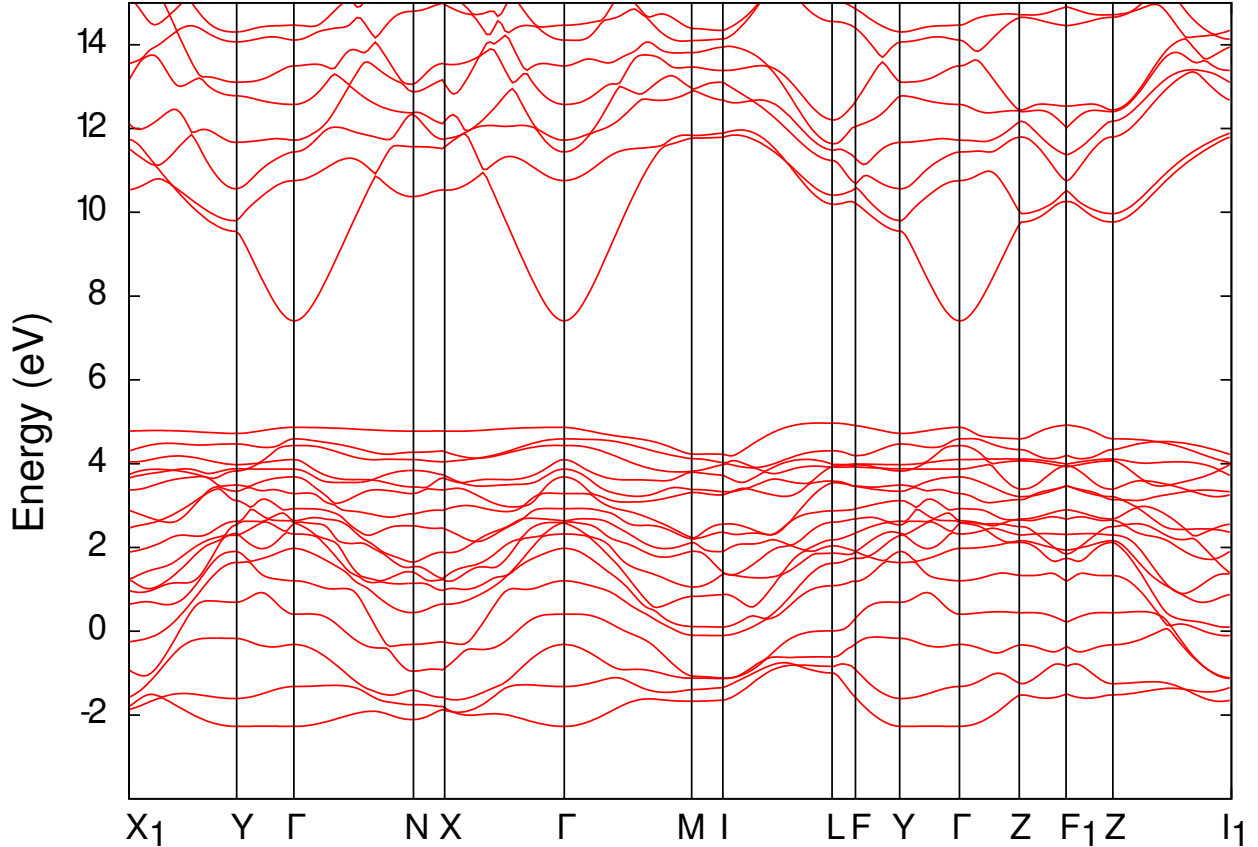
Figure 2.4: Electronic bandstructure for $\beta - \text{Ga}_2\text{O}_3$ from DFT calculations (GGA)

band-gap has been reported to be around 4.9 eV [12]. In general, oxides of post-transition metals such as Ga_2O_3 and Al_2O_3 have an $(n-1)d^{10}ns^2$ electronic configuration with densely packed metal ions. The bonding and non-bonding O $2p$ states give rise to the valence band while the conduction band arises from the Gas-Op interactions [13]. It is these Gas-Op interactions that lead to the band gap as well as the dispersion of the conduction band. As a result, these are the orbitals that will participate in charge transport upon doping.

The computed bandstructure is given in Figure 2.4 along the high-symmetry path which coincides with the BZ given previously. Notably, there is very little dispersion in the valence bands which indicates a low hole mobility. Additionally, it is interesting to note the conduction band minimum is located at Γ, but the valence band maximum is not located at this position as was previously speculated thus causing the semiconductor to technically be an indirect bandgap. In the work of [9] it was realized that the valence band maximum
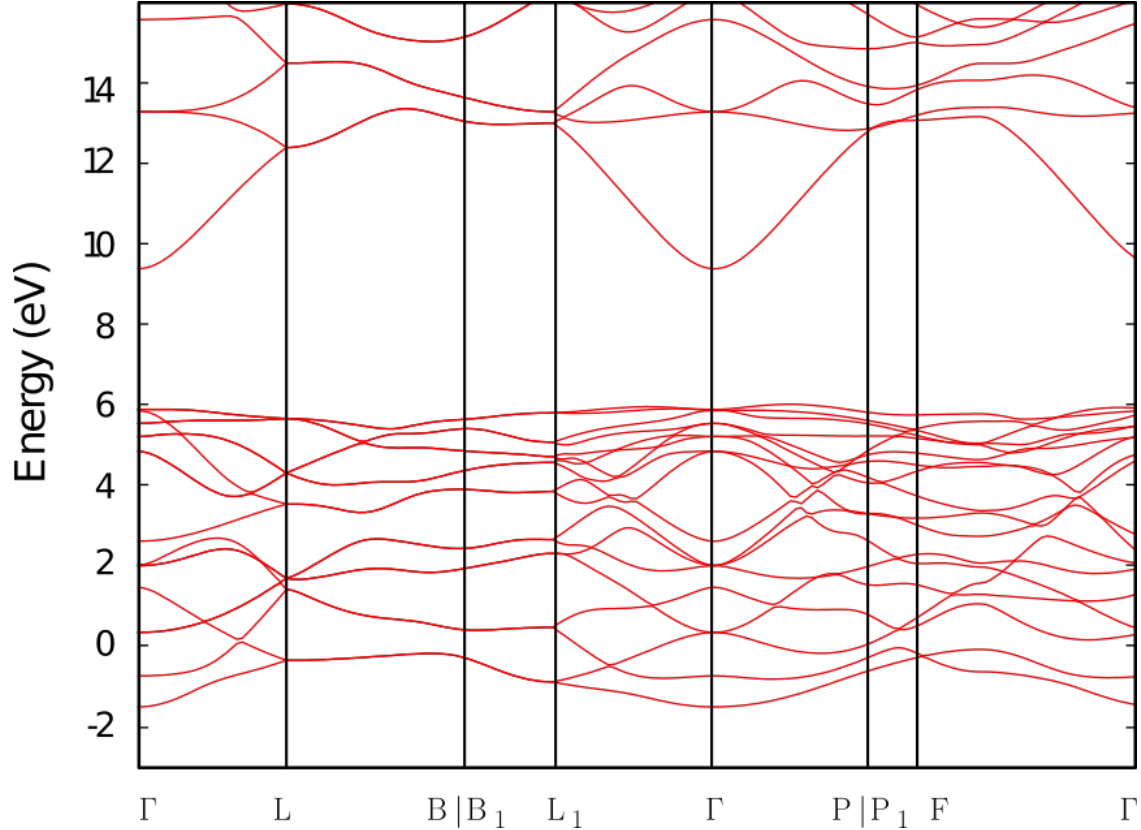
Figure 2.5: Electronic bandstructure for $\alpha - Ga_2O_3$ from DFT calculations (GGA)

is actually located at the I_1 point of the BZ which was not previously reported on. It does not in fact have a significant impact on the overall behavior however due to the dispersion of the valence bands being very small. Other valleys appear at the Z, Y, N and X points. Given the significantly anisotropy in within the crystal axes, it is relatively surprising to note the lack of corresponding anisotropy in this electronic structure. For this reason, it could reasonably be predicted that the electrical transport properties express a three-dimensional character to them and are not largely anisotropic. This property will be analyzed in further detail using effective mass calculations.

For the α phase, similar behavior is seen to the β phase and is presented in Figure 2.5, both show small dispersion in the valence bands and possess a conduction band minimum (CBM) at the BZ center (Γ-point). The computed bandgap is about 1eV larger than the β. The uppermost valence bands from the O $2p$ orbital are mostly flat and display little

dispersion. This leads to a valence band minimum which is more sensitive to the precise arrangement of atoms. Interestingly, in the α phase, the existence of an indirect bandgap is more pronounced with the indirect gap being off the high symmetry axes somewhere along Γ to P a VBM 0.3 eV higher than at Γ. In both cases, the bandgap is somewhere in the range of 2.5-3.5 eV which is lower than the experimentally determined values by a large margin. This is expected and is a limitation of DFT without using hybrid functionals that can correct the exchange-correlation term.

To correct for this inaccuracy, the use of hybrid functionals has been adopted in several works [9, 14, 15] using the Heyd, Scuseria, and Ernzerhof (HSE) [16] potential however this has consistently shown a bandgap which still underestimates the bandgap to around 4eV. To correct the bandgap in this work, the relatively new Gau-PBE functional [17] functional is adopted for its accuracy and computational efficiency. This functional approximates the Coulomb term in the Hartree-Fock potential to a Gaussian function. The results for the bandgaps compared to the GGA and experimental values is provided in Table 2.3. Excellent

	$\Delta_g^{\exp}$	Δ_g^{GGA}	$\Delta_g^{\mathrm{gauPBE}}$
$\alpha - \mathrm{Ga_2O_3}$	5.3-5.6	3.29	5.66
$\beta - \mathrm{Ga_2O_3}$	4.7-4.9	2.54	4.69

Table 2.3: Comparison to experimental bandgaps of $\alpha - \mathrm{Ga_2O_3}$ [4] and $\beta - \mathrm{Ga_2O_3}$ [1] using both GGA and hybrid functional

agreement is found with the experimental bandgaps in both phases when using the hybrid gauPBE functional. It is important to note however, due to the computational complexity of hybrid functional calculations, the ability to perform the calculation for a dense mesh in reciprocal space is limited. Computing the full band structure along the high symmetry path would require significant computational resources.

2.3 Effective Mass

Traditional electron transport computations are most commonly performed using a drift-diffusion or hydrodynamic model. Due to the complexity of these calculations, the ability to incorporate a full electronic band structure without any loss of detail is limited. Instead, an analytic approximation to the conduction band minimum (CBM) and valence band maximum (VBM) are usually used in conjunction with an effective mass approximation to analytically represent the energy dispersion for the important valleys. This approximation allows for a model of how an electron in a periodic potential will respond to external perturbation by representing the electron as a free-electron with a renormalized mass, i.e the effective mass. There is an increasing need to investigate these approximations in $\beta - \mathrm{Ga_2O_3}$ where little data is available both the electronic structure and the effective masses. This type of analysis is most commonly performed simply by evaluating the curvature of the CBM/VBM within a simple harmonic oscillator expression,

$$\frac{1}{m_\mathrm{c}} = \frac{1}{\hbar^2} \frac{\partial^2 E}{\partial k^2} \tag{2.2}$$

The most common model of band structure used in transport solvers is the parabolic band model. This method assumes a fully parabolic representation of energy dispersion where the effective mass parameter generates the entirety of the band structure about a given valley,

$$E(k) = \frac{\hbar^2 k^2}{2m_\mathrm{c}} \tag{2.3}$$

which is often valid for semiconductors where the carrier concentration is low and the electron energy is near the band minimum. The effective mass can be measured experimentally or determined from first-principles calculations where a full band-structure is used. This approximation is an efficient method of computing electronic properties, but makes the fundamental assumption that bands are parabolic in nature. As semiconductors used in electronics becomes more sophisticated and less silicon-like, the need to consider non-parabolicity becomes increasingly important. In a material at elevated temperatures, or with a higher

carrier concentrations for example, the electrons are excited to higher up in the band where there is a distinct non-parabolic character typically. This non-parabolicity can be modelled in a variety of different methods but generally introduces another representation of the artificial mass known as the "transport mass" m_t. The transport mass will be equivalent to the effective mass for completely parabolic bands. The simplest approach to characterizing non-parabolicity is derived [18] with the relationship between momentum and velocity of an electron wavepacket $mv = \hbar k$ and gives,

$$\frac{1}{m_t} = \frac{1}{\hbar^2 k} \frac{\partial E}{\partial k} \tag{2.4}$$

One of the more robust and common approaches however is to use an expansion in energy which introduces non-linearity,

$$\frac{\hbar^2 k^2}{2m_{t,0}} = \gamma(E) = E + \alpha E^2 + \beta E^3 + \dots \tag{2.5}$$

where the transport mass is expressed at the band edge, $m_{t,0}$. Taking this expression to the first order results in the Kane quasi-linear dispersion relation [18]

$$\frac{\hbar^2 k^2}{2m_{t,0}} = E(1 + \alpha E) \tag{2.6}$$

where the transport effective mass then can be determined through differentiation,

$$m_t(E) = m_{t,0}(1 + 2\alpha E) \tag{2.7}$$

Using this expression, the non-parabolicity of the bands can be characterized through the parameter α. It corresponds to the flattening of the bands as the energy moves away from the band edge. The flattening results in a larger overall transport mass. This is shown in Figure 2.6 The non-parabolicity α will be $\alpha = 0$ for a perfectly parabolic band, and will be positive or negative for conduction and valence bands respectively. Computing the curvature and Kane dispersion parameter is done in this work for $\beta - Ga_2O_3$ and compared to the recent effective mass measurements [19]. It is important to note the effect that the exchange-correlation term will have on the overall curvature. As previously shown, the

21
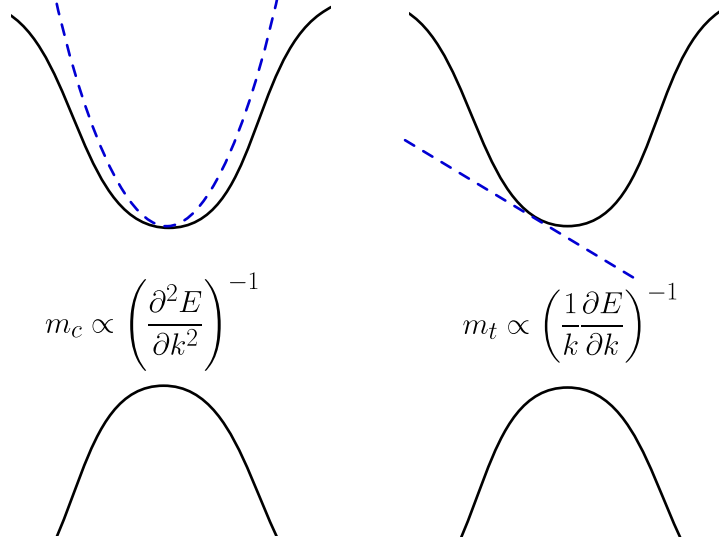
Figure 2.6: Curvature effective mass (left) is defined by the parabolicity of the band while the transport effective mass (right) depends on the gradient of the dispersion

band gap is significantly underestimated with the LDA/GGA functionals. Here the hybrid Gau-PBE functional is once again used to correct not just for the width of the bandgap, but also the curvature and anisotropy. The same bandstructure previously given is utilized and the curvature is computed along 1D slices of the BZ, i.e high-symmetry paths along the crystallographic directions. The curvature can be computed using a finite-difference approach or a quadratic-least squares approach. The non-parabolicity in the Kane-dispersion is computed using a 6th order polynomial to the eigenvalues computed in DFT for up to 0.25eV from the band edge. The transport mass is then computed through differentiation as previously noted. It is important to sample very densely near the CBM as the finite-difference method will amplify any numerical noise that comes with the energy eigenvalues from DFT. For this reason the least-squares approach is generally considered more robust. For $\beta - Ga_2O_3$, energy band reconstruction was very accurate with respect to the DFT results, this is shown for the [100] direction of the lowest conduction band in Figure 2.7. For the non-parabolic fits, the transport masses corresponding to these fits are given in Figure 2.8 as a function of energy from the band-edge. The transport masses show relatively little anisotropy in the conduction band which is surprising considering the geometric anisotropy

22
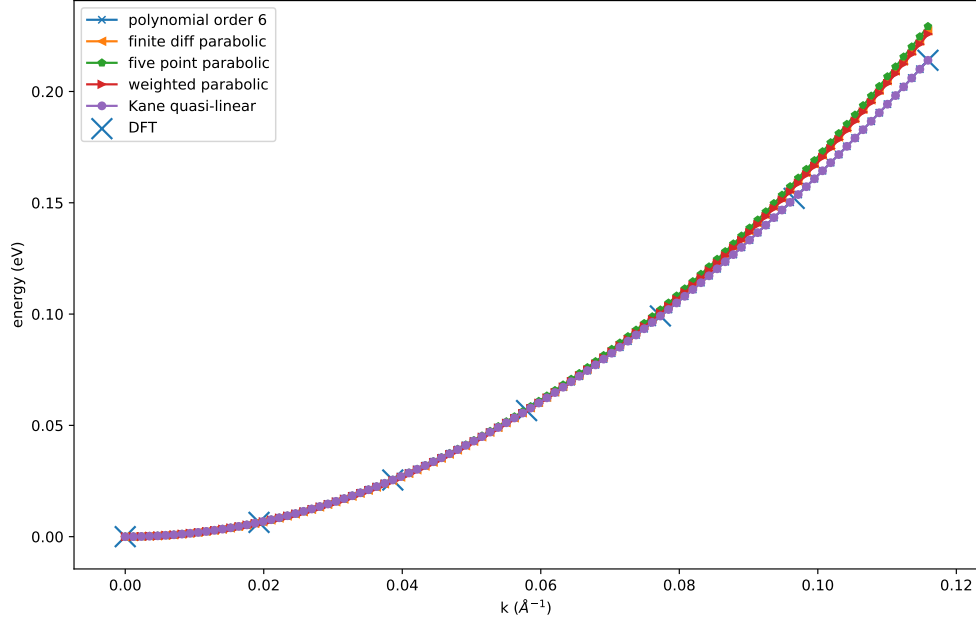
Figure 2.7: Polynomial fits of energy of the lowest conduction band near CBM compared to DFT data for $\beta - \mathrm{Ga_2O_3}$.

of the crystallographic axes. The effective mass parameters computed for both $\beta - \mathrm{Ga_2O_3}$ and $\alpha - \mathrm{Ga_2O_3}$ are presented in Table 2.4 and compared to the measured data available.

	$\alpha - \mathrm{Ga_2O_3}$			$\beta - \mathrm{Ga_2O_3}$		
	[100]	[010]	[001]	[100]	[010]	[001]
m^*_{GGA}	0.133	0.133	0.141	0.126	0.140	0.131
m^*_{hybrid}	0.261	0.261	0.272	0.223	0.301	0.292
α	0.33	0.33	0.34	0.38	0.41	0.40
Exp				0.288	0.283	0.286

Table 2.4: Computed effective mass values along crystallographic directions using GGA and hybrid functionals. Kane non-parabolicity parameters are also computed. Measured data for $\beta - \mathrm{Ga_2O_3}$ taken from [19].

It is important to note the little variance in effective mass between the two phases, this implies the effect of the oxygen coordination on the mass is minimal. Additionally, the anisotropy is relatively low, under 5%, implying the geometric anisotropy does not have a significant impact on effective mass.
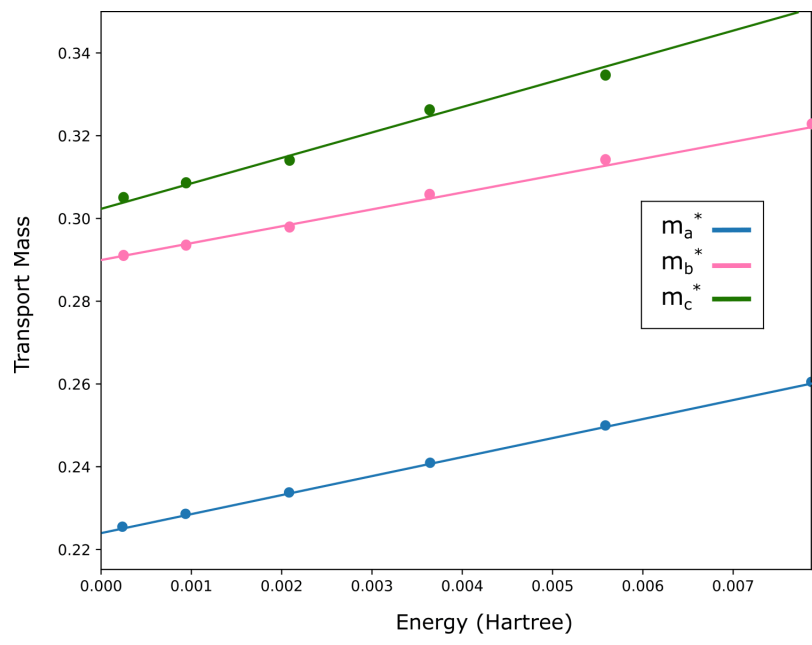
Figure 2.8: Transport mass of $\beta - \mathrm{Ga_2O_3}$ as a function of energy from the band edge along the primary crystallographic directions

CHAPTER 3

THERMAL TRANSPORT

The most prevalent bottleneck in power electronics development is often the ability to manage the very large thermal accumulation. This issue becomes more severe as the device scales down in size, resulting in a great challenge for engineering on-chip electronics. This self-heating of devices can drastically reduce lifetime of the device. For example a 50 K increase in temperature can reduce the time to failure of a device by an entire order of magnitude. Additionally, there can often be a significant influence of the thermal build-up on electronic properties of a system. Hence, a proper assessment of the thermal transport becomes an essential component to predicting a materials response properties. The effect of heat on the system can play an indirect but important role as well. For example, the complexity of the crystal structure in Ga_2O_3 naturally results in anharmonicity in thermal expansion, and this phenomena can play a significant role in the evolution of thermal stresses and growth defects such as cracks. Growth behavior is still a rapidly evolving field for Ga_2O_3 and hence thermal characteristics are of equal or greater interest in this environment, so the need for characterization is great. This need further increases when considering the known low thermal conductivity of Ga_2O_3 is considered the greatest bottleneck of the material for engineering purposes.

There are few reports of experimentally measured values for the thermal conductivity κ [20–22]. The majority of the data has been measured along the [100] and [010] crystallographic directions, yielding room temperature values of around 13 and 21 W/mK, respectively and exhibiting significant anisotropy. These low overall conductivity values have largely been attributed to scattering dominated by phonon-phonon Umklapp processes, however the exact mechanisms have yet to be explored. In this chapter, a first principles calculation of the thermal conductivity tensor (κ) is presented with a detailed analysis of the scattering contributions by phonon mode.

The need for sophisticated methods of computing thermal transport properties is relatively new and stems from the length-scales of modern power electronics devices and transistors. Macroscopic systems can appropriately apply the well-known Fouriers Law of heat and set up the system as a partial differential equation in a more traditional finite-element type framework. This style of modelling heat breaks down at the nanoscale where simultaneous ballistic and diffusive phonon transport can be occurring. Additionally these phonons can interact and scatter significantly with dislocations, vacancies, interfaces, etc. The only reasonable solution to the problem is to perform more complete solutions of the boltzmann transport equation with detailed attention to the force-interactions of atoms and their surroundings, i.e vibrational frequencies at a microscopic level.

Historically, the predictive power of computational tools for thermal transport properties involving complicated underlying mechanisms such as thermal conductivity, have been limited. Computational models generally have relied on significant empirical data to parameterize to, and even when empirical data has been available, the underlying models assume a degree of simplicity in the crystal structure. The low symmetry space group of $\beta - \text{Ga}_2\text{O}_3$ does not adhere to the required simplicity of such models. For example the "gray model" of phonon dispersion that assumes one acoustic phonon mode with a single group velocity and one optical mode of zero velocity. This approximation is often utilized and is effective for simple systems in which optical modes are known to contribute very little thermal transport. Generally, this model proves to be surprisingly effective as most thermal transport is within the acoustic phonon modes which possess the highest group velocities. For a complex crystal with many atoms in the unit cell and a large number of corresponding phonon modes however, this assumption is not guaranteed to suffice. This theoretical limitation, coupled with the complexity of taking detailed measurements of anisotropic thermal properties of ideal bulk material has hindered the predictive capabilities of Ga_2O_3 device design. Using recently developed first-principles methods however, it is possible to determine not only macroscopic thermal properties of materials but also prove a deeper insight into

the underlying mechanisms.

3.1 Boltzmann Equation

Thermal conduction at the nanoscale is dictated by the interaction and diffusive motion of the phonons of the system. Expressing this transport phenomena is handled in a variety of different ways depending on the type of carrier, the conservation laws it must adhere to, and the interplay between the mean-free path and life-time of the particle. For the case of particles in which the characteristic length-scale of relevant phenomena far exceeds the mean-free path, the transport is called diffusive. In other words, the particles on average will collide with other particles before interacting with a boundary. Quantitatively this is characterized by the Knudsen parameter

$$\text{Kn} = \frac{\Lambda}{L} \tag{3.1}$$

where Λ represents the mean-free path (MFP). Transport is considered ballistic when Kn far exceeds 1 and carrier scattering events are negligible compared to boundary effects. For realistic systems of phonon transport in an electronic device, the length scales tend to lead to Knudsen parameters between Kn = 0.1 and Kn = 10. This is considered a transitional transport regime which is the most complex to model and requires a more general transport equation to be solved which incorporates ballistic and diffusive transport. The evolution of such a system is described by a Boltzmann-type equation describing the diffusion and scattering of phonons:

$$\frac{\partial f}{\partial t} + \nabla_k \omega(k, p) \cdot \nabla_x f = [\frac{\partial f}{\partial t}] \text{ collisions} \tag{3.2}$$

where the frequency of the phonon is represented by ω, the polarization (mode index) by p, the wave-vector by k and the phonon distribution function by f. The key to any solver chosen to model this formula is in how the right-hand side is taken into account, i.e the scattering terms. Unlike the electron gas models, phonons obey Bose-Einstein statistics rather
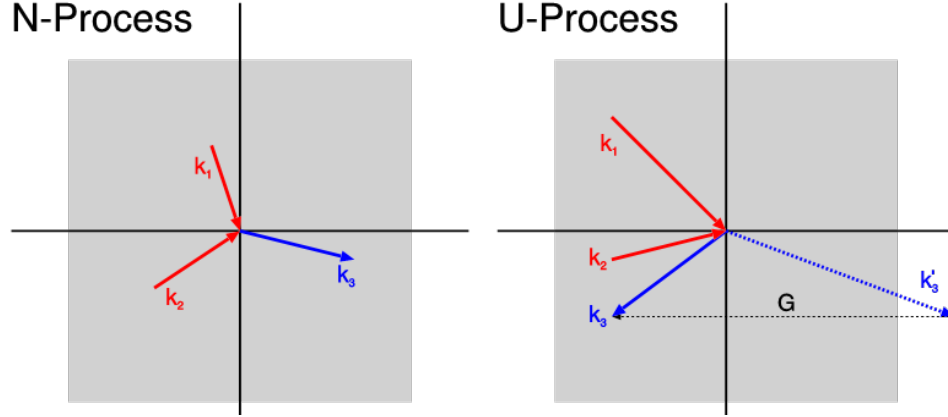
Figure 3.1: Umklapp and normal phonon-phonon scattering processes. The latter do not contribute to thermal resistance directly, and only effect scattering. They are improperly considered as resistive in the RTA and can lead to a poor estimation of thermal conductivity in materials such as Diamond which possess a large number of normal scattering events.

than Fermi-Dirac. This means they do not need to adhere to particle number conservation, which leads to many forms of interactions which can occur within the phonon population in isolation. This is also neglecting the many external scattering mechanisms which often take place in reality, which will have varying degrees of importance. Although higher-order interactions are possible, in most cases the primary interaction giving rise to thermal resistance is the three-phonon interaction, where two phonons combine to a single phonon or one phonon decays into two. Both of these processes conserve energy and total momentum accordingly. These scattering events are illustrated in Figure 3.1.

These two are classified more succinctly as:

Type I (absorption) :

$$k + k' = k'' + H$$

$$\omega + \omega' = \omega''$$

Type II (emission) :

$$k - k' = k'' + H$$

$$\omega - \omega' = \omega''$$

where $H = \vec{G}$ is the reciprocal lattice vector for Umklapp processes and $H = 0$ for normal processes. Umklapp processes are those which do not conserve local momentum due to the transference of momentum to the lattice, and hence slow the phonons down. This loss of momentum from the reference frame of the phonon gives rise to a thermal resistance, as the slowing down of the heat-carrying phonons will lead to less rapid heat dissipation. Normal processes on the other hand fully conserve momentum and thus do not directly provide resistance, but they must be considered in the BTE regardless as they do change the overall phonon occupation.

3.1.1 Phonon Boltzmann-Transport Equation

The difficulty in solving the BTE in general lies in the form of the collision operator, or the right-hand side of the BTE. In the most general form, this could be expressed as [23],

$$[\frac{\partial f}{\partial t}]_{\text{coll}} = \sum_{k',p'} \{f_{k'p'}(f_{kp}+1) - f_{kp}(f_{k'p'}+1)\}Q_{kp}^{k'p'} \tag{3.3}$$

$$+ \sum_{k'p',k''p''} \{(f_{kp}+1)(f_{k'p'}+1)f_{k''p''} - f_{kp}f_{k'p'}(f_{k''p''}+1)\}Q_{kp,k'p}'' \tag{3.4}$$

$$+ \frac{1}{2}\sum_{k'p',k'p''} \{(f_{kp}+1)f_{k'p'}f_{k''p''} - f_{kp}(f_{k'p'}+1)(f_{k''p'}+1)\}Q_{kp}^{k'p',k''p} \tag{3.5}$$

where Q is defined as the transition probability matrix which is determined by the Hamiltonian of interaction given relevant physical conservation laws. This form leads to a significantly non-linear integro-differential equation for even the simplest of geometries and is in most cases unrealistic to solve in full. Traditionally, the problem can be solved by assuming a relaxation time approximation (RTA) is valid [23]. This assumes that all momentum destroying processes tend toward an equilibrium Planck distribution and in many cases is sufficient for determining thermal conductivity. However, this assumption does not accurately incorporate normal scattering events and treats them as momentum non-conserving. In situations where normal scattering events dominate the thermal conduction, such as in low temperature environments, this approximation is not sufficient.

Recently, a more robust solution has been introduced which allows for a more realistic treatment of phonon interactions [24] which utilizes a linearized form of the BTE and has been implemented in the ShengBTE software package [24]. This approximation assumes the temperature gradient is small enough such that the distribution function f_{kp} can be expanded to first order in ΔT. The resulting form of the BTE then can be determined from the phonon dispersion, group velocities, and relaxation time determined in an iterative procedure. In this linearized BTE form, the difficult part of the calculation then becomes the determination of relaxation times τ_λ^0 for a phonon mode λ,

$$\frac{1}{\tau_\lambda^0} = \frac{1}{N}(\sum_{\lambda'\lambda''}^{+}\Gamma_{\lambda\lambda'\lambda''}^{+} + \sum_{\lambda'\lambda''}\frac{1}{2}\Gamma_{\lambda\lambda'\lambda''}^{-} + \sum_{\lambda'}\Gamma_{\lambda\lambda'}) \tag{3.6}$$

where N represents the grid density of sampled reciprocal space in the BZ and λ has been used to simplify notation and represent a (kp) pair with the scattering rates Γ^+ and Γ^- for absorption and emission being expressed as,

$$\Gamma_{\lambda\lambda'\lambda''}^{+} = \frac{\hbar\pi}{4}\frac{f_0' - f_0''}{\omega_\lambda\omega_{\lambda'}\omega_{\lambda''}}|V_{\lambda\lambda'\lambda''}^{+}|^2\delta(\omega_\lambda + \omega_{\lambda'} - \omega_{\lambda''}) \tag{3.7}$$

$$\Gamma_{\lambda\lambda'\lambda''}^{-} = \frac{\hbar\pi}{4}\frac{f_0' + f_0'' + 1}{\omega_\lambda\omega_\lambda(\omega_{\lambda''}}|V_{\lambda\lambda'\lambda''}^{-}|^2\delta(\omega_\lambda - \omega_{\lambda'} - \omega_{\lambda''}) \tag{3.8}$$

Here, conservation laws are considered by the dirac delta functions representing Fermi's golden rule combined with the collision matrix elements $V_{\lambda\lambda'\lambda''}^{\pm}$[23],

$$V_{\lambda\lambda'\lambda''}^{\pm} = \sum_{i\in u.c.}\sum_{j,k}\sum_{\alpha\beta\gamma}\Phi_{jik}^{\alpha\beta\gamma}\frac{e_\lambda^\alpha(i)e_{p',\pm q'}^\beta(j)e_{p''}^\gamma(k)}{\sqrt{M_iM_jM_k}} \tag{3.9}$$

Given this form of collision matrix, only the phonon eigenvectors e_λ^α and anharmonic interatomic force constants (IFC) are needed,

$$\Phi_{ijk}^{\alpha\beta\gamma} = \frac{\partial^3 E}{\partial r_i^\alpha \partial r_j^\beta \partial r_k^\gamma} \tag{3.10}$$

Anharmonic IFCs describe the atomic force interactions between atoms within a crystal lattice to a third order approximation to the interatomic potential. Analogously, a second order approximation to the interatomic potential would yield harmonic forces such as those found in phonons where restoring forces among atomic bonds behave harmonic oscillator like. Computing the third-order anharmonic IFCs is non-trivial. Primarily this owes to the fact that most empirical potential models found via force-matching methods are not fitted to parameters which capture the relevant anharmonic behaviors. This in part is due to the limited physical parameters which actually results from the anharmonicity in interatomic potential. Gruneisen parameters can make a good fitting parameter however they are difficult to characterize experimentally [23]. For simple systems such as silicon there has been some success with Stillinger-Weber potentials but not in a robust fashion [25]. There is no theoretical restriction for the use of an empirical force-field potential in this computation, if one could construct one that captures anharmonic force-interactions. But this remains a challenging task where the predictive power of such models becomes questionable and requires extensive validation. Alternatively, the ability to perform these calculations using first-principles methods has become feasible for most systems given enough computational resources [26].

To account for this inaccurate representation of normal modes, a full linearized BTE can be solved for bulk material subjected to a temperature gradient which accounts for all scattering terms. The details of this formulation are described in detail in [24]. Essentially, the linear system takes the form

$$\mathbf{AF} = \mathbf{B} \tag{3.11}$$

where $\mathbf{F}$ is a solution variable for a phonon mode k, $\mathbf{F}_k = (F_{k,x}, F_{k,y}, F_{k,z})$. They represent a cartesian vector of generalized mean free paths which are used in the expression

for thermal conductivity,

$$\kappa_{\alpha,\beta} = \sum_k C_k v_{k,\alpha} F_{k,\beta} \tag{3.12}$$

This is solved starting from the simpler RTA solution $\mathbf{F}_{k,\alpha} = \tau_k v_{k,\alpha}$ as the initial guess and then an iterative procedure is performed until the solution to this linear system is converged. This method is considerably more expensive but necessary for predicting thermal conductivity in systems possessing a large number of normal scattering events such as Diamond.

3.2 Methods of Computing Interatomic Force-Constants

Recent advances in ab-initio modeling have led to rigorous methods of computing harmonic and anharmonic interatomic force constants from first-principles energy calculations [26–28] on a series of displaced supercell configurations. Knowledge of the anharmonic real-space force constants allows for the phonon-phonon interactions to be computed for a given reciprocal space mesh. Significant prior work has focused on the three-phonon scattering processes and this has led to the development of accurate numerical methods of solving the phonon Boltzmann Transport Equation (BTE) to compute lattice thermal conductivity through phonon scattering.[24, 27]

3.2.1 Finite-Displacement Supercell Approach

Density Functional Theory (DFT) total energy calculations are required for the computation of interatomic force constants (IFCs). For anharmonic as well as harmonic force constants, single atoms are displaced in a supercell for various configurations based on the symmetry of the crystal. Total energy calculations from the various displaced supercells allows forces, and subsequently IFCs, to be computed. Upon displacement of the individual atoms, applied forces on the remaining atoms in the unit cell are computed and divided by the displacement distance to yield the force-constant. For polar semiconductors, the Born charges are also

added into the formulation to account for non-analytic long-range Coulombic forces. The born charges can be determined experimentally or by means of density-functional perturbation theory (DFPT). This method is sometimes known as the "direct method" [26] and is considered an extension of the "frozen-phonon" method that allows for phonon dispersion to be computed in arbitrary directions and points in the BZ. In this supercell approach, the atomic displacement of the sth atom in the unit cell is displaced in the α direction by a $\pm\delta_s^\alpha$, which can be tuned slightly but often is sufficient at a value of 0.015 Angstroms. The larger the displacement, the smaller the reciprocal space mesh is required to resolve the force-constants accurately, however too large of a value can lead to inaccuracies due to higher order force-interactions becoming dominant. The matrix element of the IFC can then be written as

$$\phi_{su}^{\alpha\beta} = - \left[\frac{F_u^\beta(+\delta_s^\alpha) - F_u^\beta(-\delta_s^\alpha)}{2\delta_s^\alpha} \right] \tag{3.13}$$

This is then used to generate the dynamical matrix at arbitrary points in reciprocal space [26],

$$D_{st}^{\alpha\beta}(\mathbf{q}) = \frac{1}{\sqrt{M_s M_t}} \sum_{\mathbf{R}} \phi_{st}^{\alpha\beta}(\mathbf{R}) e^{i\mathbf{q}\cdot\mathbf{R}} \tag{3.14}$$

this is now diagonalized to compute the square of the phonon frequencies. This method generalizes to arbitrary order force-constants assuming proper numbers of displacements are made. In this work, only up to third-order interactions are considered as they will contain the majority of the relevant phenomena to thermal conductivity. The third-order force-constants require two atomic displacements to be made at a time and higher-order would require more. In general, fourth-order IFCs can be computed using this methodology as well, but it becomes computational prohibitive due to the number of displacements required.

3.2.2   Non-analytic Corrections

It is important to take note of the effect that the ionicity of the crystal plays on the overall lattice dynamical properties. In general, the displacement of an atom in an ionic crystal

generates a dipole moment which can itself couple with other dipoles formed within the crystal by means of a macroscopic electrostatic field, and subsequently effect the longitudinal optical (LO) phonon mode energies. This electrostatic field does not however impact the transverse optical (TO) modes. These dipole-dipole interactions have an impact on the harmonic and anharmonic force constants in such a way that a splitting of the LO/TO modes occurs at the Γ point which is dependent on the direction of approach to the Γ point. These "non-analytical" contributions can be characterized by the non-vanishing Born effective charge (BEC) tensor $Z*$ in the form of a non-analytical correction to the dynamical matrix, $\tilde{D}_{st}^{\alpha\beta}$ which is written in the limit as it approaches the BZ center,

$$
\begin{aligned}
\tilde{D}_{st}^{\alpha\beta}(\mathbf{q} \to 0) &= \frac{4\pi e^2}{\Omega\sqrt{M_s M_t}} \frac{\sum_\gamma Z_s^{*\gamma\alpha} q_\gamma \sum_\nu Z_t^{*\nu\beta} q_\nu}{\sum_{\gamma,\nu} q_\gamma \epsilon_\infty^\nu q_\nu} \\
&= \frac{4\pi e^2}{\Omega\sqrt{M_s M_t}} \frac{(\mathbf{q} \cdot \mathbf{Z}_s^*)_\alpha (\mathbf{q} \cdot \mathbf{Z}_t^*)_\beta}{\mathbf{q} \cdot \epsilon^\infty \cdot \mathbf{q}}
\end{aligned}
\tag{3.15}
$$

Here ϵ^∞ is the high-frequency dielectric tensor and $\mathbf{Z}_s^*$ is born effective charge tensor for the sth atom. Both of these parameters are calculated in this work by density functional perturbation theroy (DFPT) in the QuantumEspresso software package. The force-constants are corrected by this non-analytical term in the phonon dispersion by the following form,

$$
\Phi_{st}^{\alpha\beta}(\mathbf{R}) = \phi_{st}^{\alpha\beta}(\mathbf{R}) + \tilde{\varphi}_{st}^{\alpha\beta}
\tag{3.16}
$$

where the correction is now determined by the condition

$$
\lim_{\mathbf{q} \to 0} \frac{1}{\sqrt{M_s M_t}} \sum_{\mathbf{R}} \tilde{\varphi}_{st}^{\alpha\beta} e^{i\mathbf{q} \cdot \mathbf{R}} = \tilde{D}_{st}^{\alpha\beta}(\mathbf{q} \to 0)
\tag{3.17}
$$

Which results in the final expression for non-analytical correction

$$
\tilde{\varphi}_{st}^{\alpha\beta} = \frac{1}{N} \frac{4\pi e^2}{\Omega} \frac{(\mathbf{q} \cdot \mathbf{Z}_s^*)_\alpha (\mathbf{q} \cdot \mathbf{Z}_t^*)_\beta}{\mathbf{q} \cdot \epsilon^\infty \cdot \mathbf{q}}
\tag{3.18}
$$

Born effective charges represent the first derivative of the macroscopic polarization. The results determined from DFPT calculations is presented in Table 3.1

	xx	yy	zz	xz	zx
ϵ^∞	3.8	4.1	3.9	0.114	0.114
Z^* (Ga1)	2.88	2.74	3.06	0.285	0.155
Z^* (Ga2)	3.44	3.23	3.12	-0.345	-0.180
Z^* (O1)	-2.10	-1.45	-2.50	0.067	0.037
Z^* (O2)	-2.26	-2.26	-1.38	0.205	0.228
Z^* (O3)	-1.96	-2.25	-2.29	-0.217	-0.240

Table 3.1: Born effective charges and high-frequency dielectric tensor determined from density functional perturbation theory (DFPT) for $\beta - \mathrm{Ga_2O_3}$

3.2.3 Other Scattering Mechanisms

There are potentially numerous other sources of scattering which can be present in the crystal that can lower thermal conductivity. All additional scattering will inevitably lead to increased thermal resistance so it is important to consider potentially important phenomena. One such mechanism is the effect of isotopic scattering in which the impurities present due to naturally occurring isotope composition leads to mass differences which effect the overall thermal conductivity. This scattering rate is given by the expression,

$$1/\tau_\lambda^{\mathrm{iso}} = \frac{\pi}{2N_0}\omega_\lambda^2 \sum_\kappa g_\kappa \sum_{\lambda'} \left| \hat{e}_\kappa^\lambda \cdot \hat{e}_\kappa^{\lambda'*} \right|^2 \delta\left(\omega_\lambda - \omega_{\lambda'}\right) \qquad (3.19)$$

where $\hat{e}_\kappa^\lambda$ represents the phonon eigenvector for the κ atom in mode λ. The mass variance term g_κ is the Pearson deviation coefficient of the masses $m_{i\kappa}$ for isotope i of atom κ and is given by

$$g_\kappa = \frac{1}{\overline{m}_k^2} \sum_i f_{i\kappa} \left(m_{i\kappa} - \overline{m}_\kappa\right)^2 \qquad (3.20)$$

with $f_{i\kappa}$ representing the concentration and $\overline{m}_\kappa$ the average mass. The stable isotopes of gallium are found in concentrations of 60.11% for $^{69}\mathrm{Ga}$ and 39.89% for $^{71}\mathrm{Ga}$ which gives a deviation parameter of $g_{\mathrm{Ga}} = 1.97 \times 10^{-4}$. The oxygen isotope variance is very low and will not contribute. The effect of isotopic scattering is important to consider because it is one of the potentially tunable parameters for controlling thermal conductivity. The ability to increase thermal conductivity by isotopic enrichment has recently been demonstrated [29].

Additionally, because this parameter is the only empirical input to the first principles thermal conductivity workflow, it can be adjusted freely to attempt to characterize a measured samples isotopic concentration. The last scattering mechanism which can be easily included is scattering from an ideal boundary. This is done by means of a relaxation time,

$$\tau_\lambda^B = \frac{L_{\text{eff}}}{v_{\text{ave}}} \tag{3.21}$$

where L_{eff} is the effective phonon mean free path which will be on the order of the sample size when boundary scattering is relevant. The average velocity of acoustic phonons, v_{ave} is defined by a sum of the transverse, v_T, and longitudinal velocities v_L,

$$v_{ave} = \left[\frac{1}{3} \left(\frac{2}{v_T} + \frac{1}{v_L} \right) \right]^{-1} \tag{3.22}$$

In both cases, the scattering rates are incorporated into the full solver by combining them with the anharmonic scattering rate for a given point by Matthiessen's rule,

$$1/\tau_\lambda = 1/\tau_\lambda^{\text{anharm}} + 1/\tau_\lambda^{\text{iso}} + 1/\tau_\lambda^{\text{boundary}} \tag{3.23}$$

3.2.4 Gaussian Smearing

One of the more computationally demanding and complex aspects of this workflow lies in the Brillouin zone integration scheme when integrating properties of interacting phonons. The reason for this complication is that generally, the three-phonon scattering process for a point on the sampling mesh will almost always be composed of modes which are not on the $N_1 \times N_2 \times N_3$ q-point mesh to remain energy conserving, $\omega_\lambda - \left(\pm \omega_{\lambda'} + \omega_{\lambda''} \right) = 0$. Several approaches have been utilized to attempt to solve this issue and allow for the delta functions in the lifetime calculations to be integrated over. One of the more advanced methods is known as the tetrahedron method [30]. This method entails decomposing a BZ into tetrahedral regions and using a piecewise linear interpolation on the matrix elements for integration. The method is generally very accurate however can also be expensive and can be more difficult to achieve a full convergence. The second method, which is adopted

in this work, is a broadening technique which replaces the dirac delta functions with some smearing function with a finite broadening width that can be tuned. The smearing function is generally chosen to be a gaussian of the form:

$$g\left(\omega_\lambda - W\right) = \frac{1}{\sqrt{2\pi}\sigma} e^{-\frac{(\omega_\lambda - W)^2}{2\sigma^2}} \tag{3.24}$$

where the width of the gaussian is controlled by the parameter σ and will approach a dirac delta function as σ tends to zero. The quality of this approach then becomes a delicate balance between keeping σ small enough to approximate a delta function, and keeping it large enough such that it diminishes the probability of not completing all the scattering channels needed for fully integrating the points on the sampling grid. This method is extended into an adaptive smearing framework in the work of [24] where the authors introduce how the σ parameter can be determined and adjusted automatically. Readers are referred to work of [24] for complete details on the adaptive smearing technique.

3.2.5 Convergence

Due to the infancy of the first-principles thermal transport work-flow, it is important to establish convergence criteria for the calculations to provide validation. Especially in the finite-displacement super-cell approach utilized in this work, there are many parameters that can be adjusted in the first-principles methodology. Ideally, the largest possible supercell would be used as this is more likely to assure that all atoms in the unit-cell are considering all force-interactions with neighboring cells until they have reached a radius where the magnitude is negligible. If this were not the case, there is a risk of contributions from images in neighboring supercells to be included in the FCs. In practice however, it is not realistic to increase the supercell beyond what is feasible for first-principles calculations. On the other hand, using the smallest possible supercell that would sufficiently capture force interactions would require a higher density k-space mesh to be used for sampling reciprocal space. For crystals with 80 atoms or greater, only sampling at the Γ point in reciprocal space is suffi-
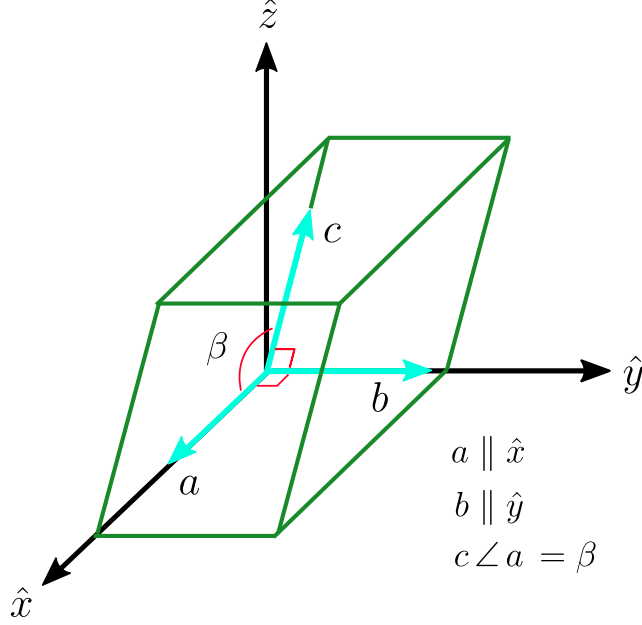
Figure 3.2: Orientation of crystal axes used in this work for monoclinic Ga_2O_3 , spacegroup C2/m

cient There is no single solutions for these problems and there are trade-offs with whatever convergence criteria is chosen. This convergence criteria becomes even more sensitive for the case of third-order force-constants where more nearest neighbor interactions also must be converged. For monoclinic $\beta - \text{Ga}_2\text{O}_3$ the largest supercell that was feasible for harmonic phonon (second-order force-constants) calculations was 3x3x3 (270 atoms) while anharmonic (third-order force-constants) was 2x2x2. In both cases, Γ-point sampling was sufficient.

3.3 $\quad \beta - \text{Ga}_2\text{O}_3$

In this section, the previously outlined methodologies are applied to $\beta - \text{Ga}_2\text{O}_3$ to determine a theoretical prediction of thermal conductivity from first-principles[31]. To compare the anisotropic material properties with the available measured results, the crystallographic orientation must be established and is illustrated in Figure 3.2.

For a monoclinic crystal, the second-rank material property tensor takes the form:

$$\kappa_{ij} = \begin{pmatrix} \kappa_{xx} & 0 & \kappa_{xz} \\ 0 & \kappa_{yy} & 0 \\ \kappa_{xz} & 0 & \kappa_{zz} \end{pmatrix}. \tag{3.25}$$

3.3.1 Phonon Dispersion

Firstly, structural optimization is performed using the plane-wave pseudopotential technique implemented in [8] using the projector augmented waves method with the generalized gradient approximation [32, 33]. Published lattice parameters were used as the initial structure for performing structural optimization [34]. A plane-wave cut-off of 125 Ryd with a $16 \times 16 \times 8$ k-point grid was used to relax the structure such that the forces on all atoms were below $1\,\text{mRyd/a.u.}$ The Born effective charges and dielectric tensor required to resolve the LO-TO splitting at the Γ point were evaluated using density functional perturbation theory [35]. The structural parameters are used for the calculations of the IFCs, both harmonic and third order, which were evaluated using a $2 \times 2 \times 2$ supercell containing 80 atoms. Due to the 10 atom primitive unit cell, there will be 30 phonon modes overall which will likely result in significant scattering to occur as many energy and momentum conserving transitions become possible. The computed phonon dispersion along the high symmetry path is presented in Figure 3.3. This dispersion shows a significant anisotropy with acousto-optical gaps being significant (approximately 15 meV) along the [001] direction which limits the possible scattering channels for high energy optical modes along this direction. Meanwhile, the [100] and [010] directions do not possess this gap but do however experience optical modes with significant group velocities. In general, optical modes are not expected to have significant group velocities and are assumed to be effectively flat and without dispersion but this is not the case here. This implies the optical modes may potentially carry a non-negligible amount of heat and could contribute to the thermal conduction. In all directions, there exists relatively steep acoustic modes with group velocities similar to GaN [20]. One distinct feature which
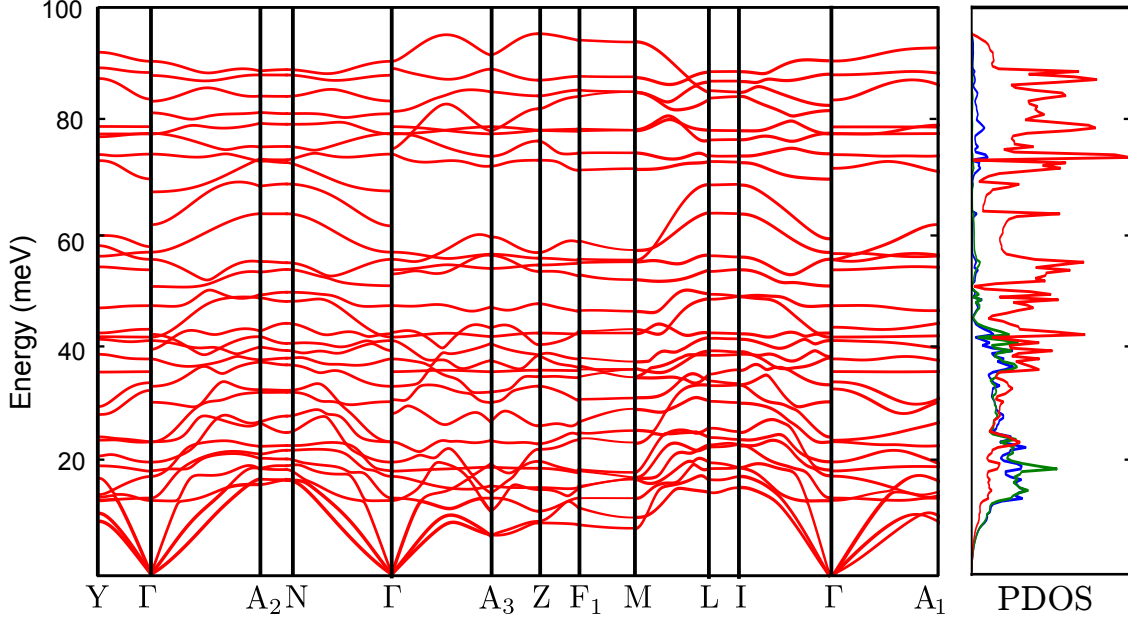
Figure 3.3: Phonon dispersion of Ga_2O_3 using a real-space finite-displacement approach. Perturbative calculations are used to resolve LO/TO splittings. $\Gamma \rightarrow A_1$, A_2, and A_3 corresponds to propagation in the directions of the conventional unit cell basis vectors.

can be seen near the Γ point, is the mixing of low lying optical modes with the acoustic modes near the BZ center.

3.3.2 Thermal Conductivity

After phonon dispersion is established, the computation can be extended to the anharmonic force-constant calculation in a similar manner outlined previously with scattering rates being calculated subsequently for use in the phonon BTE. In the calculation of thermal conductivity, the RTA and linearized form of the BTE is solved in an iterative manner. Anharmonic IFCs are used to compute scattering rates and the mean free path (MFP) parameters for each mode which are then used to compute κ. For this calculation, a $11\times11\times11$ **k**-space sampling mesh is utilized for solving the BTE over temperatures ranging from $25\,\mathrm{K}$ to $1050\,\mathrm{K}$.

The calculated values at 300K are $\kappa_{[100]}$=16.06, $\kappa_{[010]}$=21.54 and $\kappa_{[001]}$=21.15 W/mK. These values compare well with the measured values of $\kappa_{[100]}$=13 and $\kappa_{[010]}$=21 W/mK.[12, 20–22] The theoretical results systematically overestimate κ owing to the various minority

sources of scattering found in experimental samples, e.g., boundary effects at low temperatures. The temperature dependence of κ is plotted in Figure 3.4 along with fits for low and high temperature behavior.

Each range is fitted to $\kappa = \mathrm{AT}^{-\mathrm{m}}$ where A and m are fit parameters shown in the Figure 3.4b inset. For high temperatures, the system is expected to be Umklapp dominated and to exhibit a T^{-1} dependence [36], and that is the trend of the results presented here.

There is good agreement with the experimentally observed trends, especially the degree of anisotropy in the [010] and [100] directions. At low temperature (approaching 25 K) those results were not in agreement with the experimentally observed value for the [100] and [001] directions from Guo et al. This is not surprising given the importance of boundary scattering in that range and the lack of explicitly considered boundary effects considered in this BTE description. At very low T, optical modes contribute less than 1 % to κ and acoustic modes near Γ dominate transport. To capture the relevant behavior near the center, very dense k-meshes are required. Unfortunately, very dense k-meshes are computationally unfeasible due to memory scaling issues.[37]

3.3.3   Scattering Rates

The scattering rates are presented in Figure 3.5 with a temperature dependence. Overall, there is a significant dependence on temperature which is an expected trend. This is explained by analogy of the phonon gas model, in which a very strong temperature dependence exists in the Umklapp processes. Generally, the phonon scattering rate is dependent on the phonon density in the gas. Using a bose-einstein description of the phonon number density as has been done throughout this work, there is an inherent temperature dependence in the distribution function. This leads to a phonon gas density which will be low for temperatures smaller than the Debye temperature in which phonon-phonon interactions become effectively zero. This is seen in Figure 3.5a when compared to Figure 3.5d which show nearly an order of magnitude difference in scattering rate. As the temperature increases, the Umklapp
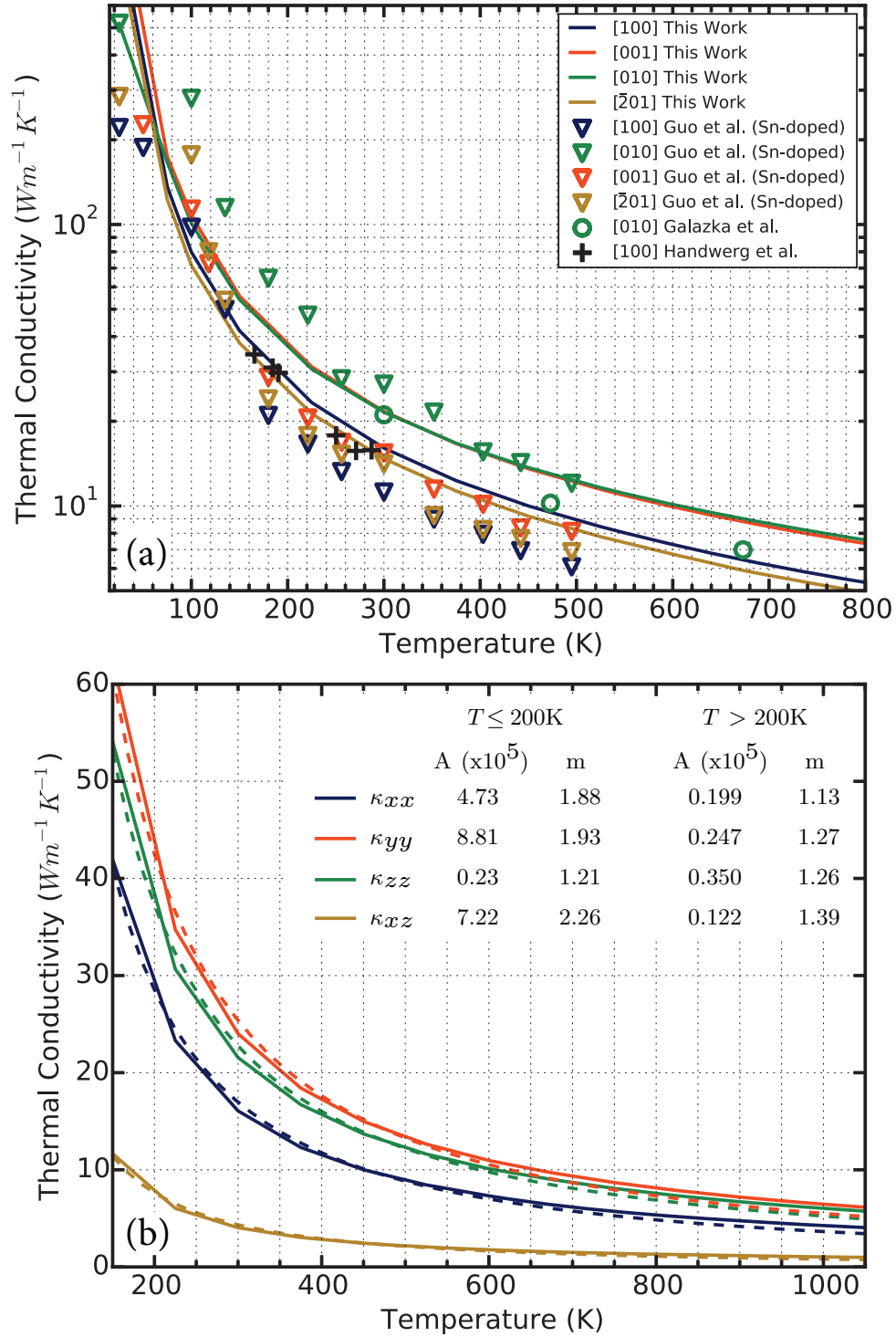
Figure 3.4: (a) Calculated and published experimental thermal conductivities vs. temperature for various crystal orientations. (b) The fitting function $\kappa = AT^{-m}$ is plotted with a dashed line (and parameters) for each κ tensor component.

processes dominate and the normal processes become negligible.

(a) 100K (b) 300K

(c) 500K (d) 800K
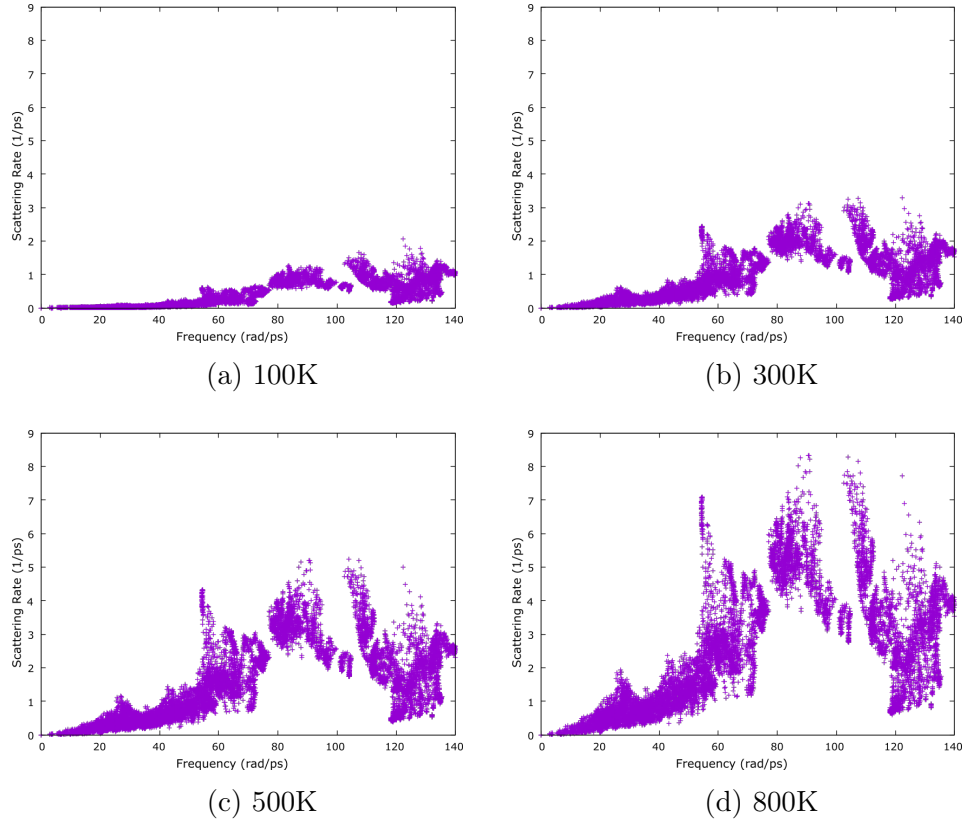
Figure 3.5: Total anharmonic scattering rate for $\beta - \mathrm{Ga_2O_3}$ at series of temperatures.

In the analysis of measured data, some have concluded that the acoustic modes dominate thermal transport and that the optical modes contribute negligibly due to low group velocities.[20, 21] It is found that this assumption cannot explain the comparatively large value of $\kappa_{[010]}$. From Figure 3.3, there is no optical phonon gap in the dispersion for states propagating along [010] while gaps exist in the dispersions for [100] and [001]. Gaps are often attributed to atomic mass differences [28] and can suppress the interaction of acoustic phonons with optical phonons above the gap. This can be seen in Figure 3.6, which plots each mode and irreducible q-point's dimensionless scattering phase space volume, $P_3^j(\mathbf{q})$, satisfying energy and momentum conservation in the three phonon processes[38]. This parameter
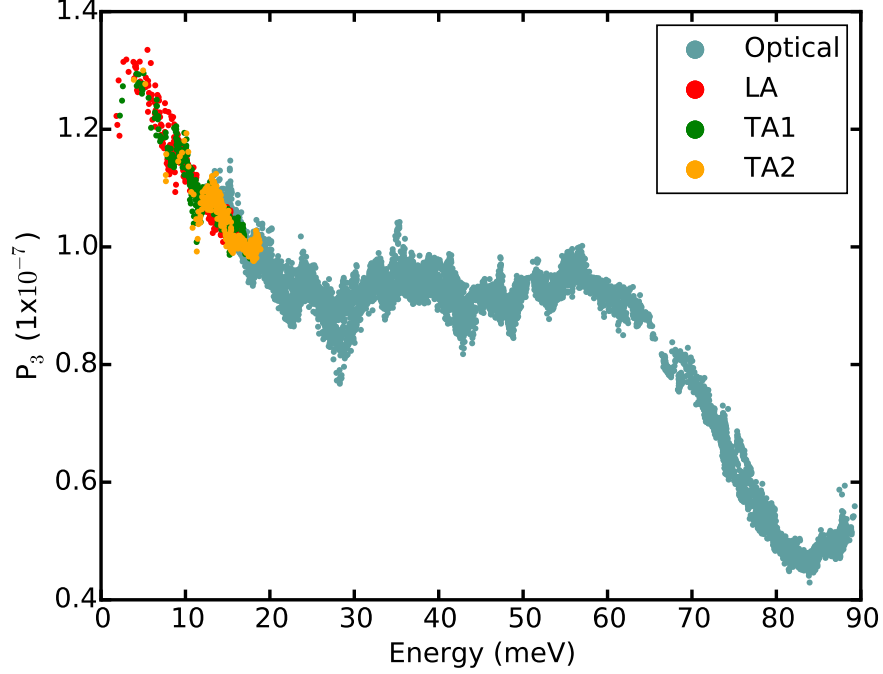
Figure 3.6: Dimensionless phase space volume available for each mode (j) and irreducible q-point ($\mathbf{q}$) to participate in three-phonon scattering processes[38]. Above the acoustic-optical phonon gap energy the available phase space is small, leading to reduced optical phonon scattering.

can be expressed as

$$P_3 = \frac{2}{3\Omega}\left(P_3^{(+)} + \frac{1}{2}P_3^{(-)}\right) \tag{3.26}$$

where,

$$P_3^{(\pm)} = \sum_j \int d\mathbf{q} D_j^{(\pm)}(\mathbf{q}) \tag{3.27}$$

and,

$$D_j^{(\pm)}(\mathbf{q}) = \sum_{j',j''} \int d\mathbf{q}' \delta\left(\omega_j(\mathbf{q}) \pm \omega_{j'}(\mathbf{q}') - \omega_{j''}(\mathbf{q} \pm \mathbf{q}' - \mathbf{G})\right) \tag{3.28}$$

In general, the smaller the phase space, the larger the phonon lifetimes and the higher the thermal conductivity. One important feature seen here is the phonon energy gap in the optical modes at around 65 meV. The lack of a gap in the [010] direction in addition to the lower TA mode v_G along [010] than [001] would lead to lower values of κ under the

	300 K			1050 K		
	[100]	[010]	[001]	[100]	[010]	[001]
LA (%)	21	20	31	21	19	30
TA1 (%)	42	20	23	40	19	22
TA2 (%)	20	16	21	20	15	20
Optical (%)	17	44	25	19	47	28

Table 3.2: Percentage of modal contributions to thermal conductivity for 300 and 1050 K. There is significant anisotropy in these contributions with the [010] having a significantly larger dependence on optical modes. The composition does not change significantly as temperature is increased.

assumption that acoustic modes dominate. To investigate further, an examination of the contributions to κ of each mode is performed using our BTE solution in Table 3.2.

At 300K, optical phonon modes contribute over 44% of the total κ_{010}. At high temperatures their contribution increases to nearly 50%. These compositions are consistent with the behavior predicted from the computed v_G for acoustic modes, which would not support higher κ without other contributions.

Contributions from optical modes are not completely surprising and have been found in many complex materials [28]. One source of the strong optical phonon contribution may arise from the hybridization of low energy optical modes with the longitudinal acoustic (LA) mode. This causes a flattening of the LA dispersion for states away from the zone center and therefore a reduction in v_G leading to reduced thermal transport from LA phonons. In this case, the contribution from optical modes may be strongly influenced by the existence of impurities[28], where deformations to the chemical bonding in the crystal can significantly alter the ability of the optical phonons to carry heat.[39] Referring to the PDOS in Figure 3.3 it is seen that at optical phonon energies, O atoms are the dominant contribution. Standard point defects in Ga_2O_3 have been via O vacancies or substitutional impurities at O sites (like Sn), so it can be expected that these impact the mode composition and thereby κ [40, 41]. This potentially opens up an opportunity for engineering of thermal conductivity through impurities and defects.

To determine length scales of relevant phonon transport, the cumulative contributions are

parameterized using $\kappa/\kappa_{accum} = 1 + \Lambda_0/\Lambda_{\max}$ where κ_{accum} is the conductivity associated with accumulated contributions up to a MFP cutoff of $\Lambda_{\max}$. The full value is κ and Λ_0 can be interpreted as representative of the MFP of relevant heat-carrying phonons.[24] The parameterized contributions are shown in Figure 3.7 for each mode as a function of $\Lambda_{\max}$. This is informative for determining the length scales at which each phonon mode becomes relevant for carrying heat.[28] Results for each mode are summarized in Table 3.3.

	Λ_0^{300K} (nm)				Λ_0^{1050K} (nm)			
	LA	TA1	TA2	Optical	LA	TA1	TA2	Optical
[100]	187	320	331	8	44	79	75	2
[010]	62	63	82	11	15	16	21	2
[001]	380	174	384	10	92	45	88	2

Table 3.3: Characteristic MFP, Λ_0, indicating the length scale above which each phonon mode contributes to κ.

There is a significant directional dependence on the MFP. This indicates an anisotropy in the influence boundary effects will have as a function of length. This effect has been experimentally observed for Ga_2O_3 thin films were used as gate contacts for high frequency GaN devices. It was shown that κ spanned 1.5 orders of magnitude when an interface was introduced [42].

3.3.4 Memory Scaling

There are several parameters that can be tuned in the workflow presented. It is important to verify the set of parameters used is converged. Firstly, the sampling mesh for the DFT calculation in this work was chosen to be a 2x2x2 k-mesh in reciprocal space for the harmonic force constants and gamma point only for anharmonic force constants. The mesh was confirmed to converge for the 2x2x2 case by comparing with a gamma only mesh for harmonic force constants. The force constants experience a change of at most .1% and thus are sufficiently converged even with just a gamma point sampling. This is expected considering the large
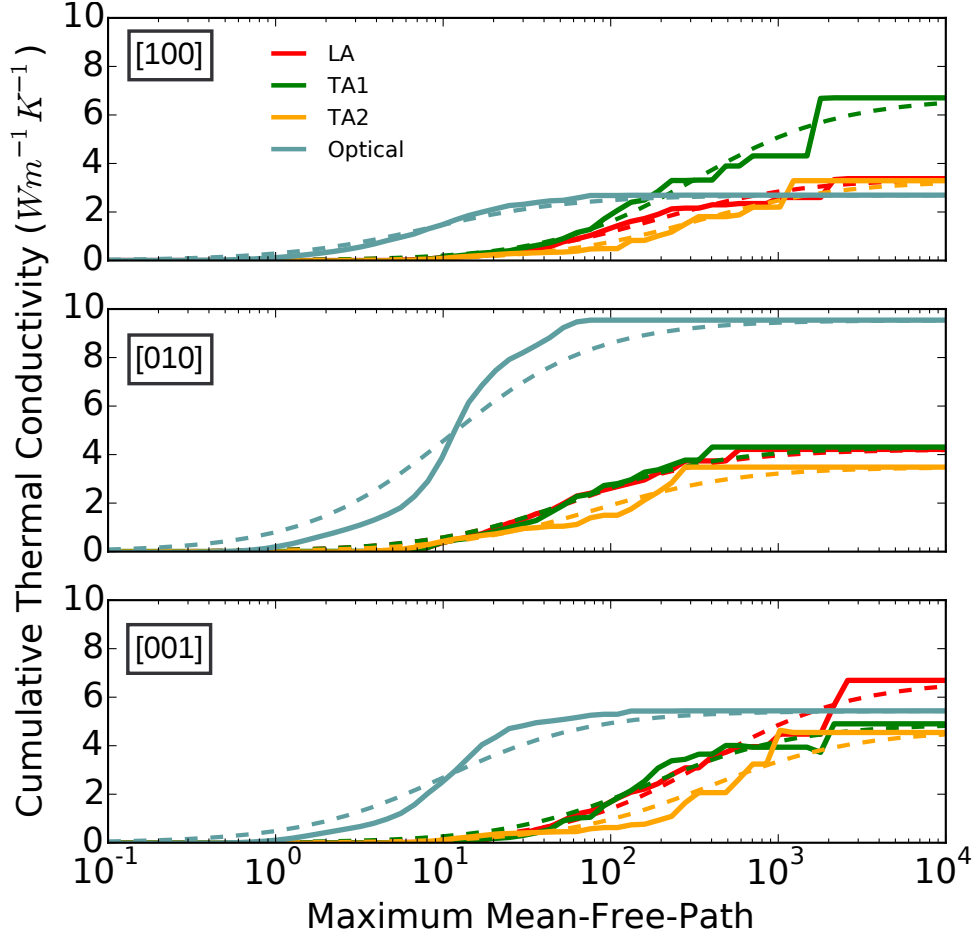
Figure 3.7: Accumulated thermal conductivity in three crystallographic directions for each mode as Λ_{max} is increased. Fits to a parametric function are shown by the dashed lines.

size of the unit cell for β-Ga$_2$O$_3$ which grows considerably larger when using a supercell. This large volume in real space shrinks the volume of reciprocal space considerably. When reciprocal space is sufficiently small, gamma point only sampling will sufficiently sample the brillouin zone for our purposes. The same principle applies to the anharmonic force constant calculation. For the anharmonic calculation a comparison was performed analyzing the effect of increasing the nearest neighbor interactions from 3 to 6 and have not found significant changes to the final thermal conductivity (under 1 Wm^{-1}K^{-1}).

The algorithm for solving the BTE is not easily parallelizable and scales poorly with respect to the size of the sampling mesh which will be discussed in more detail in a later section. For this reason it becomes prohibitively expensive to use a dense sampling mesh. To
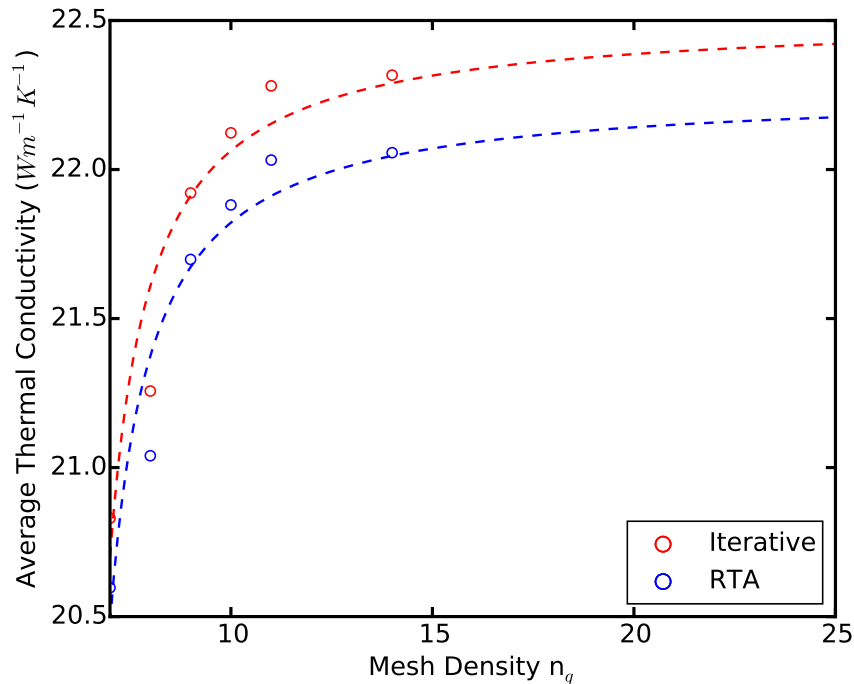
Figure 3.8: Convergence of Iterative and RTA methods with increasing mesh density

validate the convergence of the result with respect to the sampling mesh, an extrapolation procedure can be used as explained in [24]. Results are computed for several mesh densities (6x6x6, 7x7x7, 8x8x8, 9x9x9, 10x10x10, 12x12x12 and 14x14x14) and fitted using:

$$\kappa_{n_q} = \kappa_\infty (1 - \frac{c}{n_q}) \tag{3.29}$$

where n_q is the number of q-points sampled in each direction, κ_{n_q} is the corresponding thermal conductivity, c is fitting parameter and κ_∞ is the final thermal conductivity approximated to an infinitely dense mesh. Results for this extrapolation at 300K in both the iterative and relaxation time approximation (RTA) are shown Figure 3.8

The final convergence parameter that must be addressed is the size of the supercell used in both force constant calculations. Upon testing, the chosen supercell size is a 2x2x2 supercell based on published literature [43]. This cell consists of 80 atoms. Expanding this cell to a 3x3x3 supercell is computationally very demanding due to the number of atoms increasing to 270. Additionally, the size of the 3x3x3 cell will lead to configurations contain-

ing displacements too small to be resolved without increasing the convergence threshold to smaller than 10^{-5}. Which becomes prohibitively expensive with such a large cell. Increasing the displacement size can be a solution but can also potentially induce a anharmonic content which will not be accounted for. For supercells larger than 2x2x2, it is likely that a perturbation theory approach would be more computationally feasible and accurate.

The low symmetry of the monoclinic structure in addition to the large number of atoms in the supercell introduces very large memory requirements. Additionally, the algorithm requires a full set of phonon eigenvectors to be loaded into memory on each node for computation. So the number of processors cannot be very large for this structure. This particularly input file required approximately $64\,\mathrm{GB}$ of memory per node. Additionally, the memory scaling behaves as N^5 where N is the number of k-mesh points in a single direction. So increasing the mesh density further is unrealistic without access to very large memory nodes or running on very few processors. The latter introduces issues with computational time. After testing a sequence of mesh densities, It was found the 11x11x11 mesh to give the best solution with reasonable resource requirements. The temperature was swept for a sequence of 20 temperatures, so it was important to conserve resources when possible. The majority of the simulations performed in this work were performed on two 256GB memory nodes and utilized 4 Xeon E5-2670 2.5GHz cores.

3.3.5   Choice of Functional

One topic that has not been explored in detail thus far is the effect of the exchange-correlation term on the anharmonic force-constants and subsequently the thermal conductivity. This effect is largely unstudied in even simple materials but its effect can potentially be important. The effect of the LDA vs GGA functionals has proven to be significant in the determination of mechanical properties such elastic constants due to the underestimation and overestimation of the lattice constants respectively. Recent studies investigating the effect have found the predictions of LDA and GGA to be nearly equivalent for thermal conductivity [44]. This

result is non-intuitive considering the LDA formulation over-binds while the GGA under-binds and softens the IFCs. It was speculated in [44] that this phenomena arises from the cancellation of errors in the respective approximation methods for the exchange-correlation functionals. The LDA case generates larger third-order IFCs due to the overbinding but is cancelled by the increased acousto-optical gap in the phonon dispersion, decreasing phase-space for phonon-phonon scattering events and vice-versa for the GGA predictions.

3.4 $\alpha - \mathrm{Ga_2O_3}$

There does not currently exist any literature on thermal properties of single crystal α phase due to the difficulty in maintaining the metastable phase for measurement. The recent surge of interest in $\alpha - \mathrm{Ga_2O_3}$ as an alternative to $\beta - \mathrm{Ga_2O_3}$ has increased the need for a theoretical understanding analogous to this chapters treatment of $\beta - \mathrm{Ga_2O_3}$. The complexity of the alpha phase is less than that of the beta phase due to the higher symmetry the crystal possesses so the computational requirements are less restrictive.

3.4.1 Phonon Dispersion

The phonon dispersion for $\alpha - \mathrm{Ga_2O_3}$ is computed using a 3x3x3 supercell and 2x2x2 mesh in reciprocal space to determine force-constants. The results along high-symmetry path are presented in Figure 3.9 The non-analytical correction were again computed within a DFPT framework in QuantumEspresso and give the born effective charges as well as the high-frequency dielectric function summarized in Table 3.4 Overall the phonon dispersion behaves similarly to the β phase, with comparable group velocities. The most distinct feature is the lack of a sizable acousto-optical gap for any of the high-symmetry directions. The lack of a gap implies smaller IFCs and softer bonds with an increased phase-space for anharmonic scattering. The reduction in IFCs likely stems from the lack of an tetrahedrally coordinated gallium cation present in the corundum structure. The lack of a gap is likely to cause a reduction in thermal conductivity compared to the β phase.
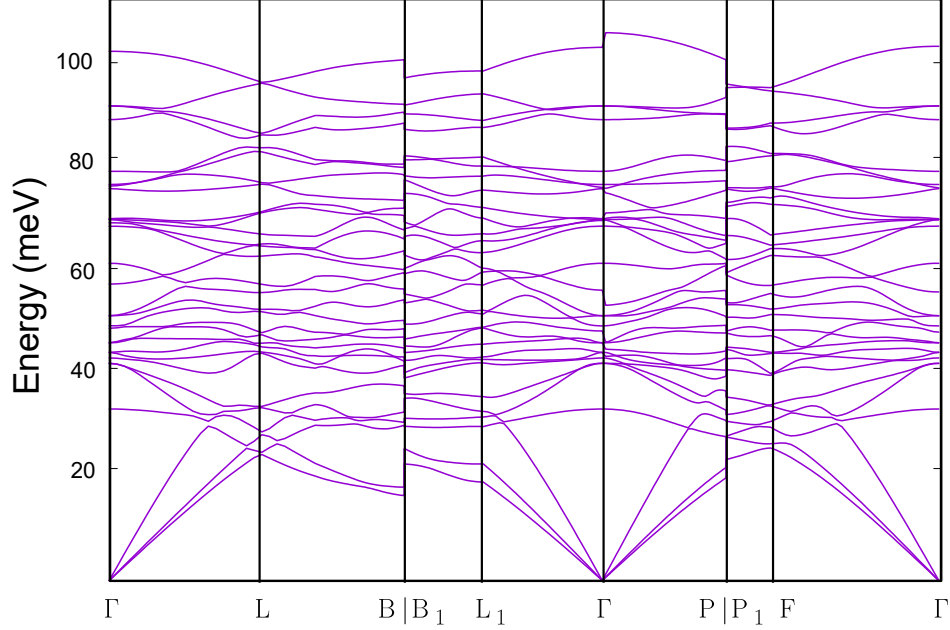
Figure 3.9: Calculated phonon dispersion of $\alpha - Ga_2O_3$.

	xx	yy	zz
ϵ^∞	3.9	3.9	4.0
Z^* (Ga1)	3.20	3.23	3.23
Z^* (Ga2)	3.20	3.23	3.23
Z^* (O1)	-2.48	-1.88	-2.08
Z^* (O2)	-1.96	-2.40	-2.08
Z^* (O3)	-1.96	-2.18	-2.30

Table 3.4: Born effective charges and high-frequency dielectric tensor determined from density functional perturbation theory (DFPT) for $\alpha - Ga_2O_3$

3.4.2 Scattering Rates

Anharmonic force-constants were computed and used in determining the phonon-phonon scattering rates which are presented in Figure 3.10. The lack of a pronounced gap is evidenced further by these plots, as well as the increased overall scattering, with the magnitudes increasing as much as 60% over the β phase. As temperature increases, the magnitude grows more rapidly than the β phase as well.

(a) 100K

(b) 300K

(c) 500K

(d) 800K
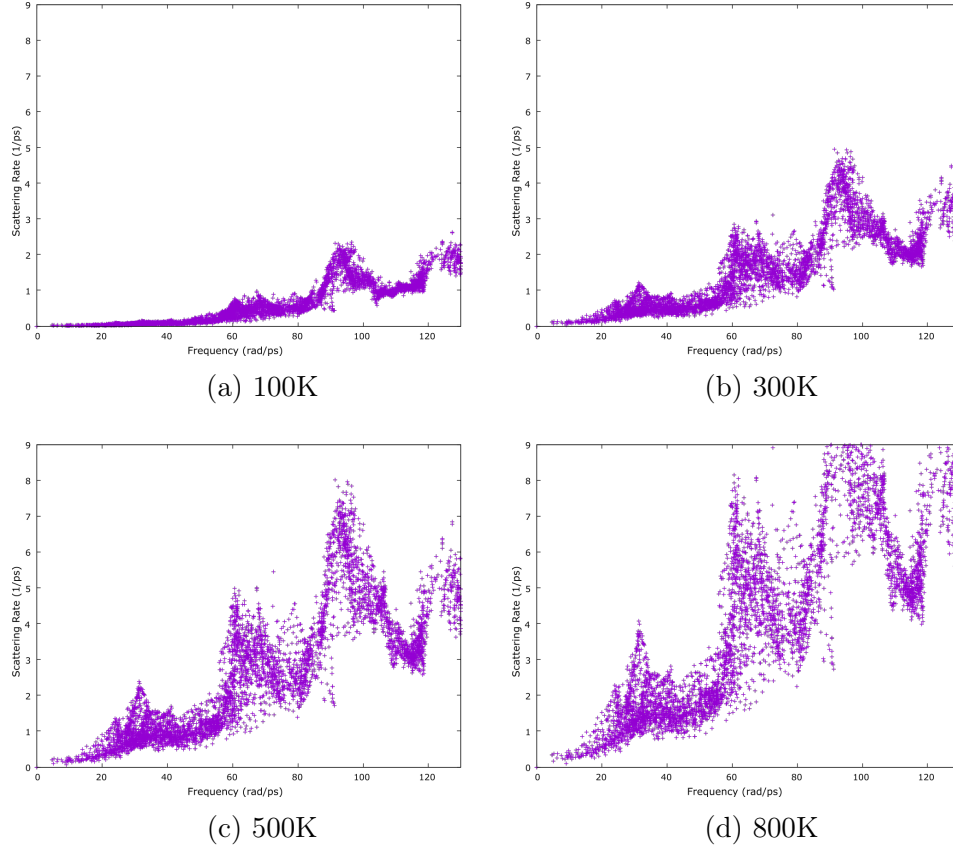
Figure 3.10: Total anharmonic scattering rate for $\alpha - \mathrm{Ga_2O_3}$ at series of temperatures.

3.4.3 Thermal Conductivity

Solving the BTE in the RTA framework gives the thermal conductivity tensor presented in Figure 3.11. Unlike the β phase, the thermal conductivity is relatively isotropic with a negligible anisotropy along crystallographic directions. Most importantly however, the thermal conductivity is approximately half of the magnitude of the β phase. This is not surprising given the larger scattering rates and lower phonon lifetimes.

The $\alpha - \mathrm{Ga_2O_3}$ polytype is most often grown and used in thin-film form, and it is important to characterize what thermal conductivity suppression may arise from the size of the film thickness. This also can be done within the first-principles framework presented here following the methodology of [45]. Firstly, the in-plane ($\kappa_{\parallel}$) and cross-plane ($\kappa_{\perp}$) is
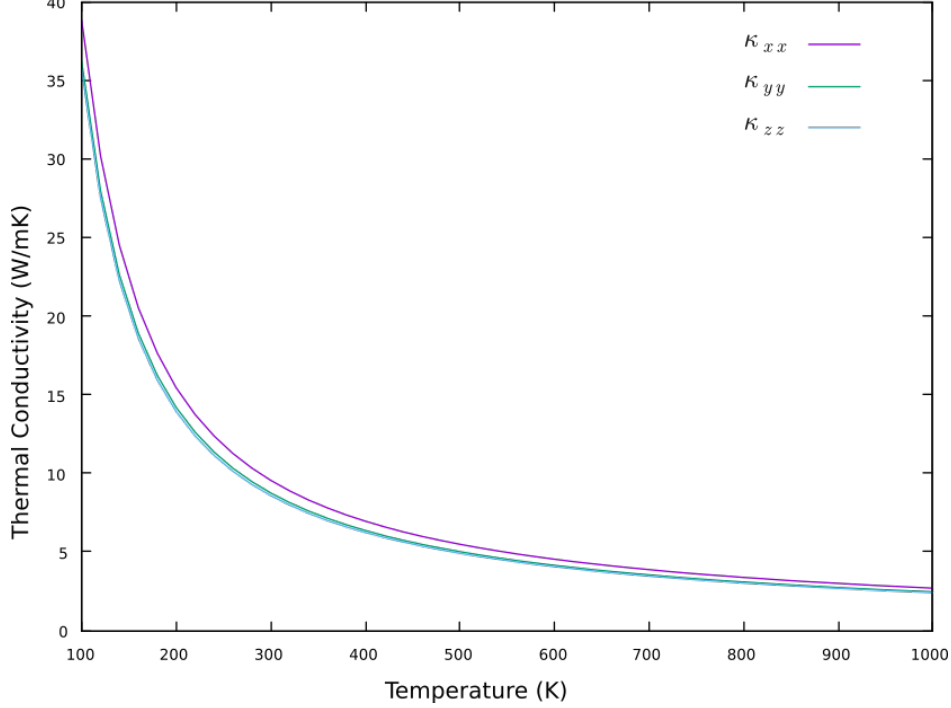
Figure 3.11: Calculated thermal conductivity of $\alpha - \mathrm{Ga_2O_3}$. Unlike the monoclinic counterpart, the axes are nearly isotropic

expressed within the RTA as an effective thermal conductivity of the form, eb

$$\kappa_{\mathrm{eff}}(L) = \sum_k S_k(L) C_k \, \|v_k\| \, \Lambda_k \cos^2 \vartheta_k \tag{3.30}$$

where the film thickness is L, and a suppression function $S(L)$ is constructed to incorporate the additional phonon scattering that a film boundary will provide. Additionally, ϑ represents the angle between group-velocity vector and the direction of transport and Λ_k is the MFP. The in-plane suppression function is formulated as,

$$S_\| = \frac{1 - p \exp\left(-\frac{1}{K}\right) - (1-p)K \left[1 - \exp\left(-\frac{1}{K}\right)\right]}{1 - p \exp\left(-\frac{1}{K}\right)} \tag{3.31}$$

where the parameter p indicates the specularity of the film, ranging from 0 to 1. For $p = 0$, the film boundaries are perfect absorbers and for $p = 1$, perfect reflectors. The Knudsen parameter is given by K and is computed within a transformed coordinate system [45] as,

$$K = \frac{(\hat{v}_{\hat{z}}/\|\boldsymbol{v}\|) \cdot \Lambda}{L} = \frac{\hat{\Lambda}_{\hat{z}}}{L} \tag{3.32}$$
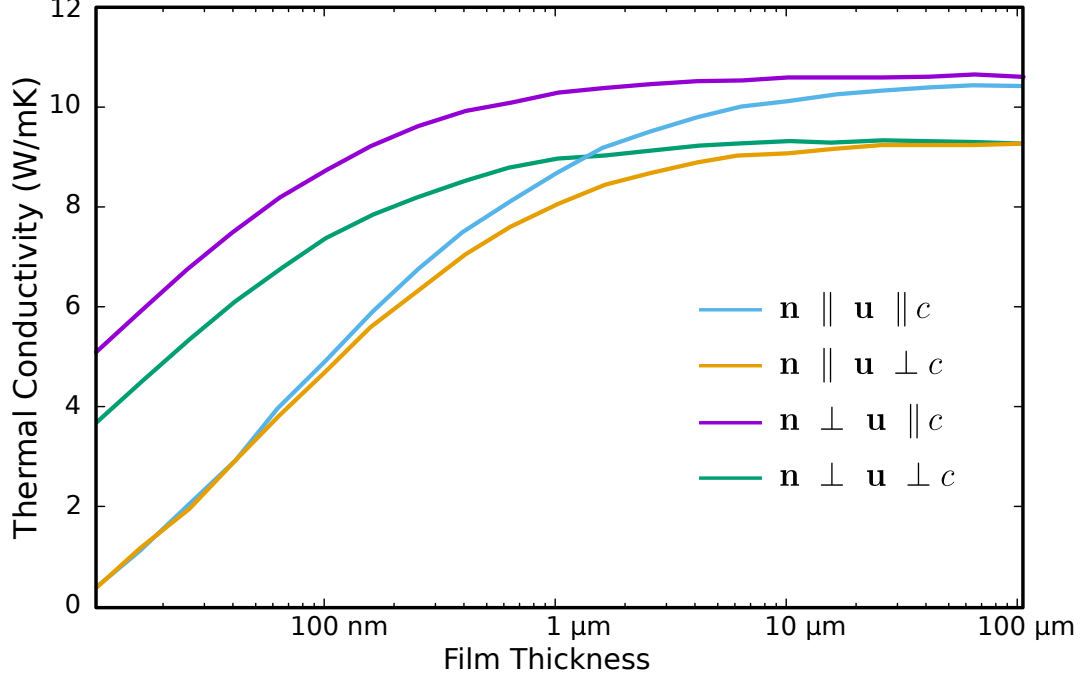
Figure 3.12: Effective thin-film thermal conductivities for in-plane and cross-plane transport with respect to the c-axis of $\alpha - Ga_2O_3$. Specularity was set to p=0.2

In the cross-plane direction, the transport vector u is along the normal direction n and hence the film boundaries act as perfect absorbers and no specularity appears in the suppression function expression,

$$S_\perp = \frac{1}{1 + 2K} \tag{3.33}$$

with a Knudsen number that is simpler to calculate and can be written as,

$$K = \Lambda |\cos \vartheta| / L \tag{3.34}$$

Using the IFCs and subsequent scattering rates from the bulk thermal conductivity calculation, the effect of the thin-films are assessed and presented in Figure 3.12. It is seen that the effect of the thin-film scattering is relatively strong and the thermal conductivity is nearly half of its bulk value for 100 nm film thickness for cross-plane thermal conductivity. The in-plane reduction is slightly less due to the nature of the suppression function formulation. This reduction in thermal conductivity is at length-scales well in excess of what has already begun to see engineering applications. For example, the recent success of a metal-
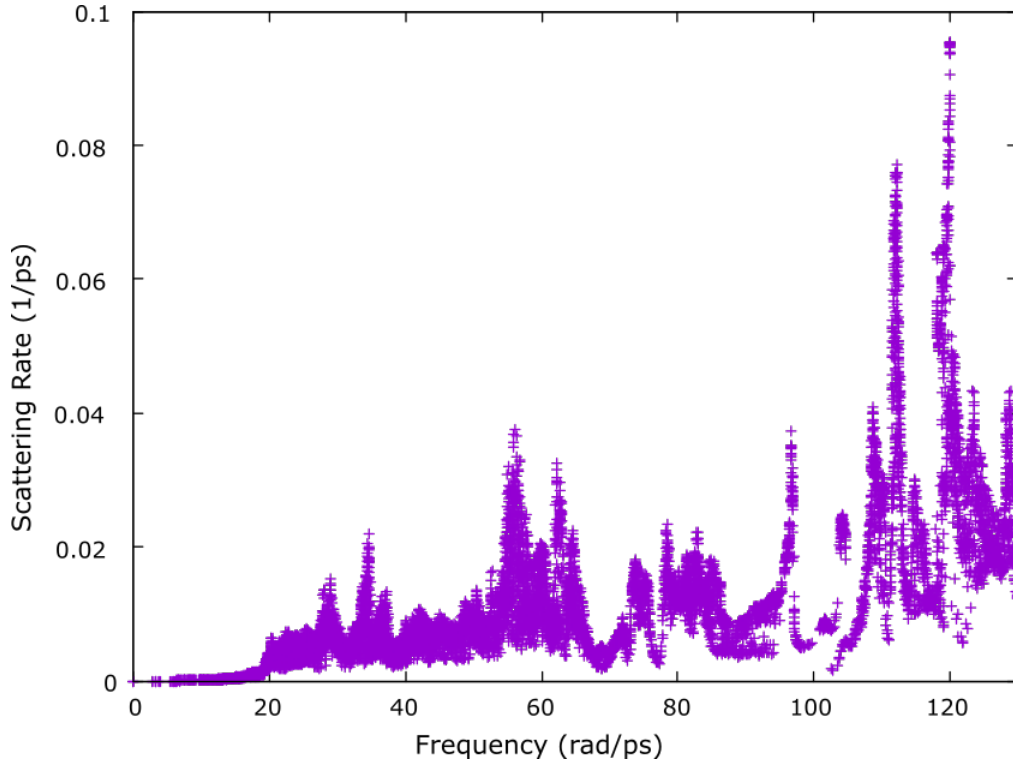
Figure 3.13: Isotopic scattering rates using natural isotopic distributions for $\beta - \mathrm{Ga_2O_3}$

semiconductor-metal photodetector in [46] utilizes an $\alpha - \mathrm{Ga_2O_3}$ thin layer thickness of only 10 nm, an order of magnitude lower than where the thermal conductivity was found to be halved.

3.4.4 Isotope Effect

The effect of the naturally occurring isotope scattering for various Gallium based semiconductors has recently been investigated in [29] where it was determined that in the case of GaN for example, the thermal conductivity can be increased as much as 65% through isotopic enrichment from a naturally occurring isotope concentration to pure isotope. This isotopic scattering mechanism plays the role of a mass-disorder scattering term similar to the effect an impurity would have. The effect of isotope concentration has been analyzed and is presented here. The isotopic scattering rates are also presented in Figure 3.13 for the β phase, And for the α phase in Figure 3.14 to be notably different than what was found in the
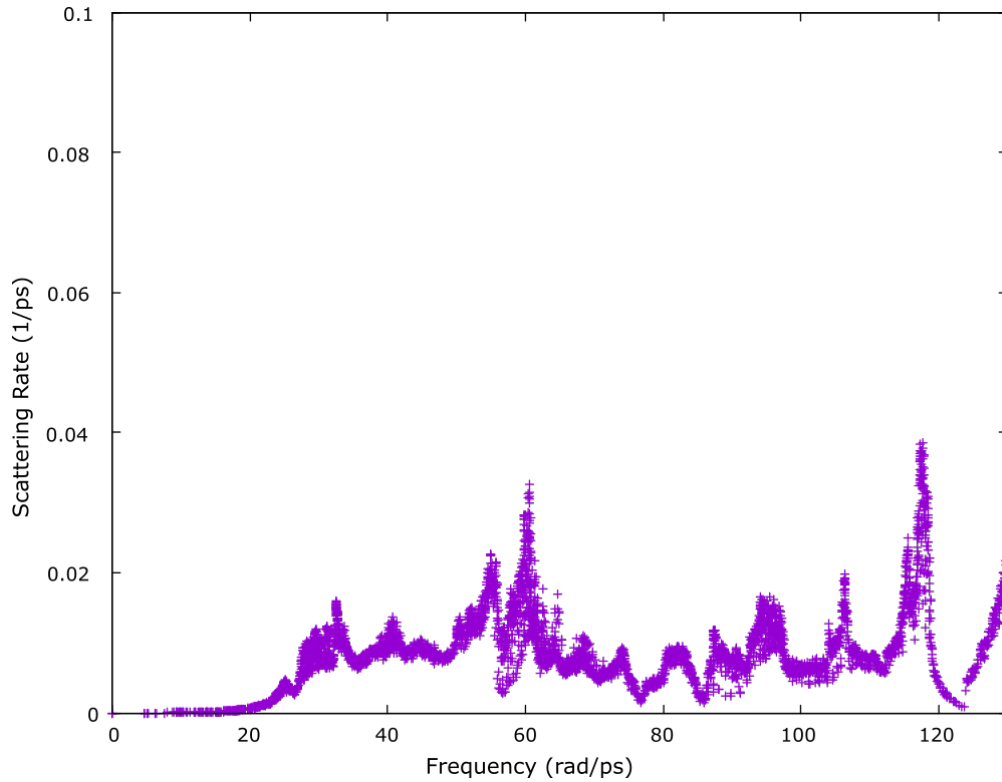
Figure 3.14: Isotopic scattering rates using natural isotopic distributions for $\alpha - Ga_2O_3$

β phase with lower magnitude of scattering rates for the whole range of frequencies. Overall, the effect the isotopic scattering has on the thermal conductivity can be seen in Figure 3.15 and appears to be a minor effect. The disparity between pure and natural isotope mixtures is more prevalent at lower temperatures, where the effect of impurities is in general more relevant. At most there is a 20% increase in thermal conductivity in the β phase with the notably less in the α phase which is consistent with the isotopic scattering rates presented. Considering the difference between the two crystal structures, it can be inferred that the effect of isotope variation throughout the structure has more impact on the tetrahedrally coordinated Gallium cations found in $\beta - Ga_2O_3$ which are not present in $\alpha - Ga_2O_3$.
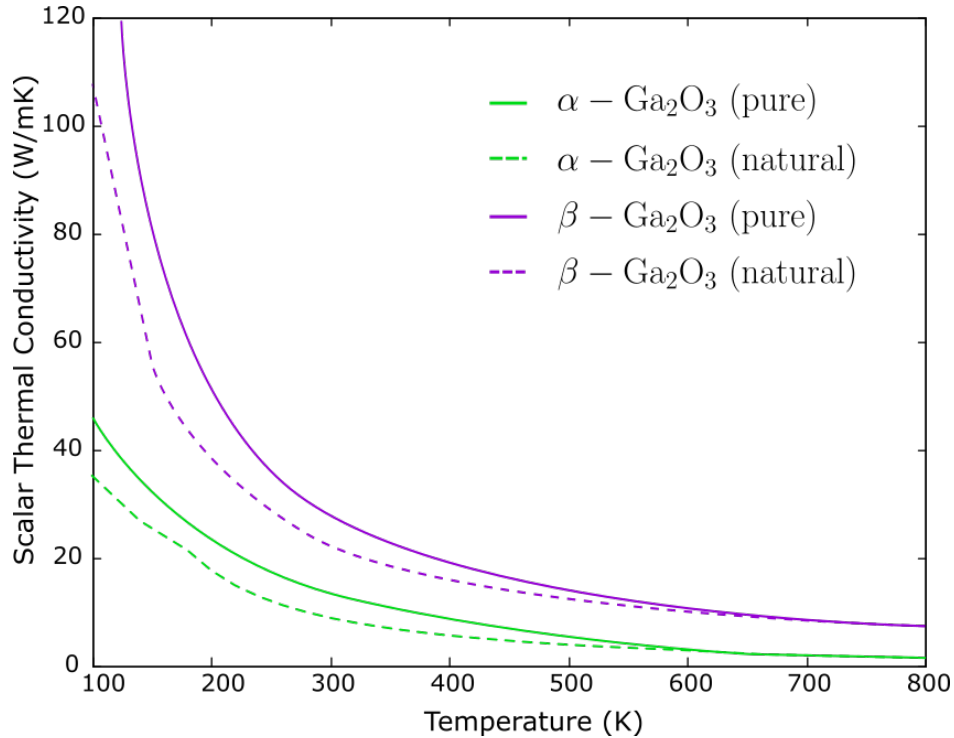
Figure 3.15: Thermal conductivity of $\alpha - \text{Ga}_2\text{O}_3$ and $\beta - \text{Ga}_2\text{O}_3$ using both nautral and pure isotope mixtures.

3.5   Layered Structures

Use of a high thermal conductivity heat-sink for thermal management has been speculated to be the only practical solution of remedying self-heating effects in Ga_2O_3 devices. One could assume using as highly conductive a substrate/heat-sink as possible would yield the greatest results but this has not been the case in practice [1]. In the case of nitride semiconductors, CVD diamond has been used for heat removal and it was found that the quality of the interface between the materials was limiting. There has been some preliminary success with Ga_2O_3 self-heating reduction experimentally by using higher thermal conductivity heatsink materials, however it is difficult to characterize and predict what materials will prove to be effective at heat removal due to the difficulty in achieving a strong adhesion of metal contacts to the semiconducting material. Considering this limitation, it becomes important to produce a more complete phonon model that incorporates boundary/interface scattering effects in addition to simply phonon-phonon scattering. Realistic electronic de-

vices are typically made from layering of various semiconductor materials as well as metallic ohmic contacts and this leads to a complicated temperature distribution which is controlled primarily by how the energy carrying particles, whether it be phonons or electrons, behave at an interface. Traditionally the multilayer problem could be simulated for basic material layers using a very simplified Fourier model with some approximate model for the effect of an interface. This however does not consider the atomistic properties of the underlying material and assumes the layers to be isolated from one another in terms of quantum mechanical considerations. The more accurate method to represent a realistic structure would be using a molecular dynamics style simulation with a full description of atomic interactions. This is often unrealistic however due to the very large number of atoms which would be required and the corresponding computational expense. The solution then becomes to find an accurate way to utilize the BTE approach outlined previously while still considering the interface.

As a remedy of the curse of dimensionality, there has been recent success at combining the linearized BTE with a deviational monte-carlo solver that performs calculations orders of magnitude faster than the traditional MC counterpart. In this case, the equilibrium component of the system is determined using the established linearized phonon BTE and the non-equilibrium components split into particle-like wave packets with stochastic trajectories that can be determined statistically, with MC techniques [45].

3.5.1 Variance-Reduced Monte-Carlo

Firstly, it is important to understand why traditional MC techniques are inefficient for computations of properties such as thermal conductance by introducing a simple toy problem. Suppose there is a spherical domain in which the center is fixed at a temperature of 301 K and the rest of the domain is fixed at 300 K. As with many particle MC techniques, the problem can be discretized and phonons can be lumped into "superparticles" which are computational constructs to represent a larger population of phonons with similar properties. These particles are assigned an occupation given by the Bose-Einstein distribution and the

local temperature. The heat flux of this system is then determined by allowing particles to move and scatter until they have reached a steady-state condition and the subsequent heat-flux can be determined by summing the net particle number gain/loss for each "cell" of the system. This is a very inefficient method of simulation due to how close the particles already are to the equilibrium distribution function with respect to the very small temperature gradient they experience. This then requires a very fine resolution for simulation with a very large number of computational particles to simulate. The problem becomes significantly more complex when considering extrinsic events such as an electron-phonon scattering event in which the resolutions required for the electron scale differ significantly from the phonon scale.

Recently, a solution to one-dimensional thermal transport of multi-layered structures with isothermal boundary conditions was introduced in [47]. The methodology implements a variance-reduced Monte-Carlo scheme to solve the boltzmann equation for phonons. The main idea behind these methods is to solve the phonon BTE using an approximation of the nonequilibrium component, g_k, of the distribution of individual modes. This is a feasible approximation in situations such as the previously outlined example, where the phonon distribution functions are very nearly the equilibrium Bose-Einstein condition, which is of course trivially obtained analytically. This concept is illustrated in Figure 3.16

This approximate g_k consists of a sum of a number of delta functions (energy packets) all with the same energy and each with a well defined position. These packets are then tracked using a stochastic monte-carlo method and their trajectories can be analyzed. Rather than being actual phonons or super-particles of phonons, these packets are a mathematical construct and labelled as "deviational particles". They are simply abstract representations of corrections to the Bose-Einstein distribution function which can be represented as positive or negative depending on whether they are emitted from the hot or cold thermal reservoir. It is also important to note that the solutions of trajectories of deviational particles is performed in the linear approximation, where the temperature deviations are small. This assumption
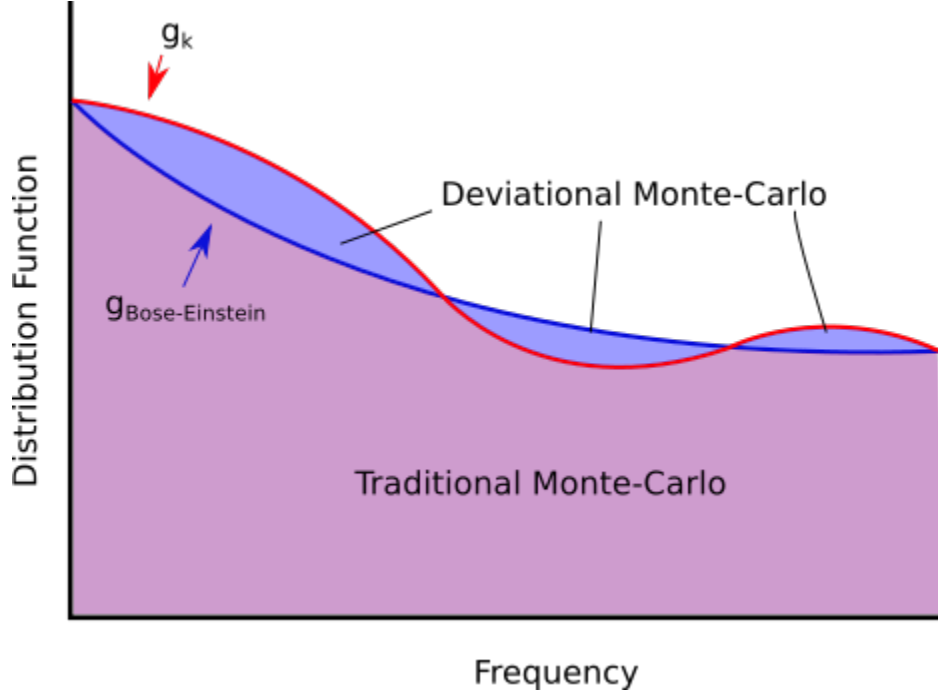
Figure 3.16: Overview of the distribution function of a computational particle and the simplification of the deviational particle approach. The blue shaded area represents the actual deviation from equilibrium which is simulated in VRMC. Only a very small deviation from the Bose-Einstein is common in problem where the thermal gradient is small.

is necessary to prevent a location dependence of phonon properties within the respective materials and the deviational particles are independent of each other.

The lifetime of the deviational particles is illustrated, including the possible scattering events that a particle experiences, in Figure 3.17.

This amounts to the following workflow,

1. **Launch Event** - This is the initial source function essentially, where we impose a deviational intensity function from the reservoirs given by

$$I_{\text{iso}} = \frac{\hbar}{V} \sum_{k} (\boldsymbol{v}_k \cdot \boldsymbol{n}) \, H\,(\boldsymbol{v}_k \cdot \boldsymbol{n}) \, \omega_k \left[f_{\text{BE}}\,(\omega_k, T_{\text{iso}}) - f_{\text{BE}}\,(\omega_k, T_{\text{ref}}) \right]$$

   Particles are randomly assigned to reservoirs with a corresponding probability

$$p_{\text{hot}} = |\mathcal{I}_{\text{hot}}| \, / \, (|\mathcal{I}_{\text{hot}}| + |\mathcal{I}_{\text{cold}}|)$$

$$p_{\text{cold}} = 1 - p_{\text{hot}}$$

60
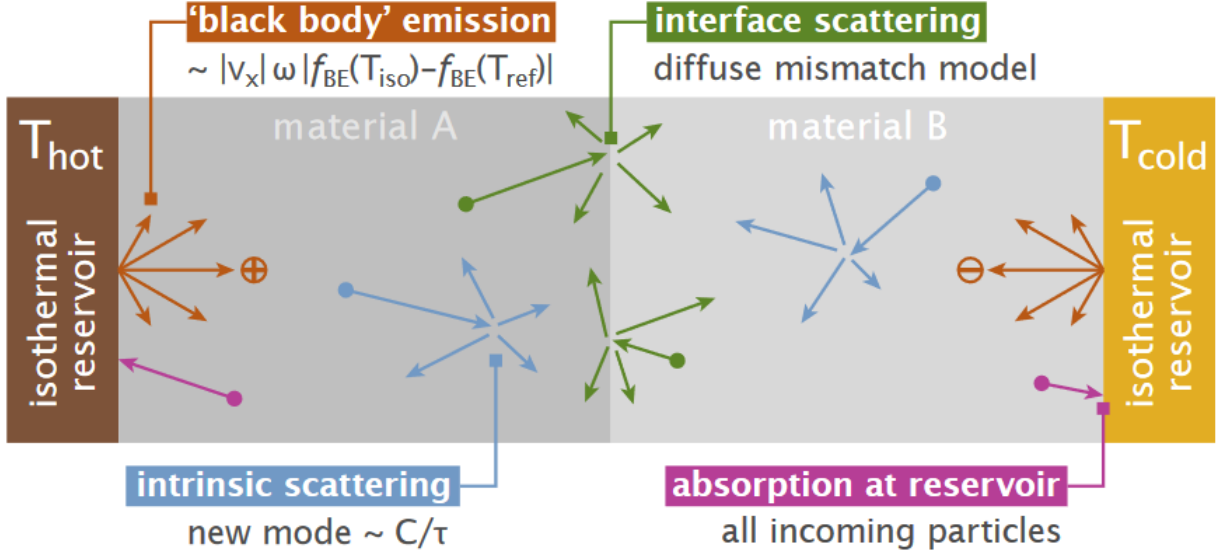
Figure 3.17: Overview of lifetime of deviational particle in the variance-reduced MC scheme. Orange arrows represent the initial deviations imposed by a source intensity function. Green shows the interface scattering mechanisms, pink the reservoir absorption and blue an intrinsic scattering event where no interface effects are necessary to include.

2. **Advection steps** - Advancing the particle in time is the primary step of the MC process. Using the group velocities of the particle v_x, a random time step, χ, is generated from an exponential distribution and the particle advances its position $\Delta x = \chi v_x$, from here there are several possible final states depending on what the particle experiences,

   a) Layer/interface - the particle is reflected/transmitted according to a diffuse mismatch model and the particle is assigned a new phonon mode while conserving energy. For two materials M_1 and M_2 the incident particle is assigned a new phonon mode from the distribution[45],

   $$= \left(\boldsymbol{v}_k^M \cdot \boldsymbol{n} \right) H \left(\boldsymbol{v}_k^M \cdot \boldsymbol{n} \right) G^M \left(\omega_k \right) / \left(V^M N_{\text{tot}}^M \right) \tag{3.35}$$

   where G is the gaussian regularization of the delta function and the total number

61

of modes is given by

$$N_{\text{tot}} = N_A \times N_B \times N_C \times N_{\text{branches}} \tag{3.36}$$

b) Boundary - when the particle reaches a boundary, it has completed the trajectory and is considered terminated. The iterative process moves on to the launch of the next particle and stores the heat flux contributions for post-processing

c) Pure advection - if the particle does not experience any boundary or interfaces along the trajectory, it is assigned a new phonon mode solely based on the intrinsic phonon lifetimes (determined from the phonon-phonon scattering rates)

3. **Summing heat flux** - To analyze the trajectories, the system is partitioned into bins. At each bin, the total number of deviational particles which successfully crossed can be summed to determine the total heat flux. From this, an effective thermal conductivity for the entire structure can be expressed:

$$\kappa_{\text{eff}} = \frac{q_{\text{net}}}{(T_h - T_c)/L_{\text{tot}}} \tag{3.37}$$

Traditionally, the effectiveness of a thermal contact is more readily expressed by the thermal conductance.

$$r_{\text{eff}} = \frac{T_{\text{hot}} - T_{\text{cold}}}{q_{\text{net}}} = \frac{L_{\text{tot}}}{\kappa_{\text{eff}}} \tag{3.38}$$

This parameter characterizes the amount of heat which crosses an interface in a given temperature gradient. In other terms, it can be described as the ratio of the temperature discontinuity at an interface to the heat flux flowing across the interface. Often it is solely this parameter which determines the effectiveness of a thermal coating and the ability to tailor the TBC is crucial for thermal management engineering. On the atomic scale, TBC is determined by the mismatch of phonon density of states of the two materials of the interface. However in practice, the TBC can be significantly dependent on properties which describe the quality of the interface mechanically. For example, the specularity, interfacial roughness,

interface chemistry and chemical bonding all can play a significant role potentially. In the work performed here, an idealized model is used in which none of these chemical and mechanical factors are considered explicitly. With respect to these factors, any idealized model adopted here would theoretically serve as an upper-bound estimate, in practice however this is very dependent on the type of mismatch model which is adopted to represent the effect of the interface.

3.5.2   Diffuse Mismatch Model

Traditionally, the effect of an interface can be modelled in a couple of different ways. The method described previously, which is utilized in the VRMC, is essentially a form of diffuse mistmatch model (DMM). In this method, the scattering at the interface is assumed to be completely diffuse and elastic. The transmission probabilities are determined solely from the phonon dispersion available on each side of the interface and the phonons have no "memory" of the mode it represented before scattering with the interface. The alternative model commonly adopted for representing interfaces is the acoustic mismatch model (AMM) which treats phonons in their planewave representation in a continuum model. Then, an acoustic impedance can be assigned for each side of the interface. This method has shown success for very low temperatures but is not an effective solution for the temperatures of realistic device operation or for instances where optical phonons are also contributing to thermal transport. As was previously shown throughout this chapter, the optical phonons in $\beta - \mathrm{Ga_2O_3}$ do contribute a non-negligible amount of group velocity to allow for heat to be carried by them and thus cannot be easily ignored. One important restriction of the DMM is the mentioned requirement of elastic scattering mechanisms only. The method does not consider inelastic sources of scattering such as an electron-phonon scattering event which are in general difficult to characterize [48]. In this work, the AlmaBTE [45] package is utilized which is restricted to the assumption of fully elastic scattering such the an incident phonon can feasibly undergo elastic mode conversion in a timely manner. In other words, if the discrepancy in phonon

63
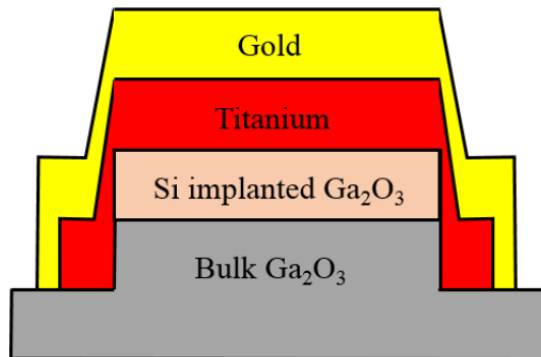
Figure 3.18: Ohmic contact of Au/Ti on Si-implanted Ga_2O_3

density of states between the two materials of the interface are significantly different, it is unlikely to experience primarily elastic phonon scattering.

3.5.3 Source-Drain Thermal Conductance

Using the previously outlined methodology for the case of $\beta - Ga_2O_3$ it is now possible to estimate the thermal conductance for a real thermal contact in a transistor between source and drain. The most basic interface in this scenario that has been experimentally considered [42] has been a direct $Au/\beta - Ga_2O_3$ contact achieved by e-beam evaporated and sputtered Au layers. Knowing the low thermal conductivity of $\beta - Ga_2O_3$, this direct ohmic contact will make a very poor thermal conductor. To improve this ohmic contact, an adhesive layer is generally added as shown in Figure 3.18 with titanium as an example. In general, reactive metals such as chromium and titanium can make for good adhesion layers.

In this setup, the layer thickness is an important variable to control the magnitude of the thermal conductance. As the layer increases in thickness, it can potentially add more resistance by increasing the amount of intrinsic phonon scattering which occurs before a phonon reaches an interface. In this work, the VRMC algorithm is used with first-principles determined force-constants and scattering rates for $\beta - Ga_2O_3$ with the contact materials chromium and titanium to assess how well $\beta - Ga_2O_3$ can form thermal contacts and if the thermal boundary conductance (TBC) is a limiting factor in thermal management. The

64

reason for these materials is two-fold, firstly they are known to make good adhesive materials for metal-dielectric interfaces. Titanium in particular is perhaps the most common metal-dielectric adhesive layer material. It has recently been shown however that chromium can significantly improve the TBC of Ga_2O_3 interfaces due to the overlap it has in the phonon density of states. In general, the metal-dielectric interface will be dominated by elastic phonon scattering incidents, as discussed previously. In these events, phonons of the same frequency will couple at the interface, hence the higher overlap between phonon density of states functions, the more phonon transmission will occur and the higher the TBC will be. In the debye model the phonon DOS functions can be roughly sketched as Figure 3.19. The
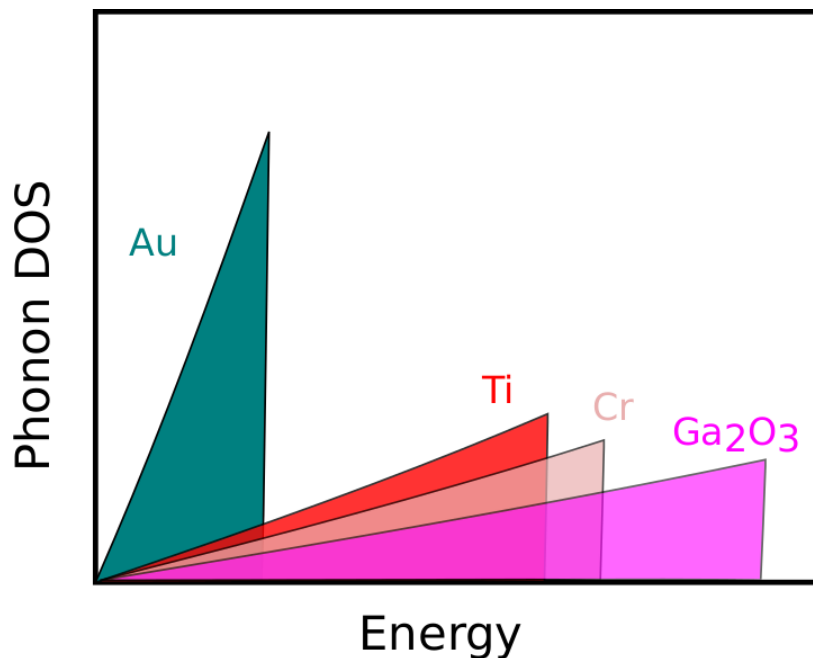
Figure 3.19: Debye phonon density of states comparison for $\beta - Ga_2O_3$ and the interface materials. Chromium and Titanium both contain a significantly improved overlap in the density of states, leading to increased elastic scattering and phonon transmission at the interface.

VRMC calculation is run for a sweep of layer thickness for the chromium and titanium, with the $\beta - Ga_2O_3$ thickness being held at 400nm. This setup was analyzed experimentally in [42] where a structure similar to that shown in Figure 3.20 was used. The number of computational particles used is in the VRMC solver $N = 10000$ with the thermal boundaries
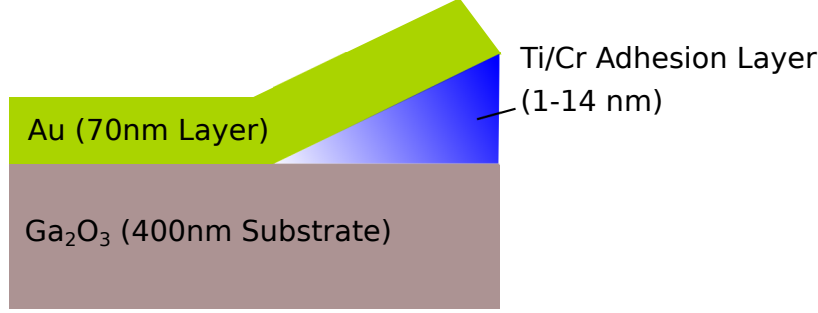
Figure 3.20: Thermal contact for $\mathrm{Au}/\beta - \mathrm{Ga_2O_3}$ using a wedge adhesive. This illustrates the experimental setup of [42] this work compares to. In this work, successive simulations are run for the range of layer thickness presented in the wedge of adhesive Ti/Cr.

being held at $300\,\mathrm{K}$ for the cold side and $300\,\mathrm{K}$ for the warm side. The scattering rates for $\beta - \mathrm{Ga_2O_3}$ were computed from a 12x12x12 grid in reciprocal space. These simulations represent a perfect boundary which in practice is unrealistic. Surface roughness and surface chemistry effects can often change the TBC significantly. An initial calculation for the TBC using a direct $\mathrm{Au}/\mathrm{Ga_2O_3}$ interface is computed with a resulting phonon TBC value of $G_p = 61\ \mathrm{MW/m^2K}$ which is comparable to the experimentally determined value of of $G_p^{\mathrm{exp}} = 80\ \mathrm{MW/m^2K}$ [42]. This value is generally low for a metal-dielectric interface, which is expected considering the small density of states overlap between these two materials. Maximizing this value is crucial to device engineering as the heat dissipation controls the stability of integrated circuits. To further investigate, the Kapitza length can be defined by

$$L_k = \frac{\kappa_{\mathrm{avg}}}{G_p} \tag{3.39}$$

This length determines the required thickness of the material with average thermal conductivity κ_{avg} to have an equivalent resistance with the interface. The Kapitza length For the direct $\mathrm{Au}/\mathrm{Ga_2O_3}$ interface is found to be $L_k = 344$ nm, which can be restrictive for device engineering depending on the applications.
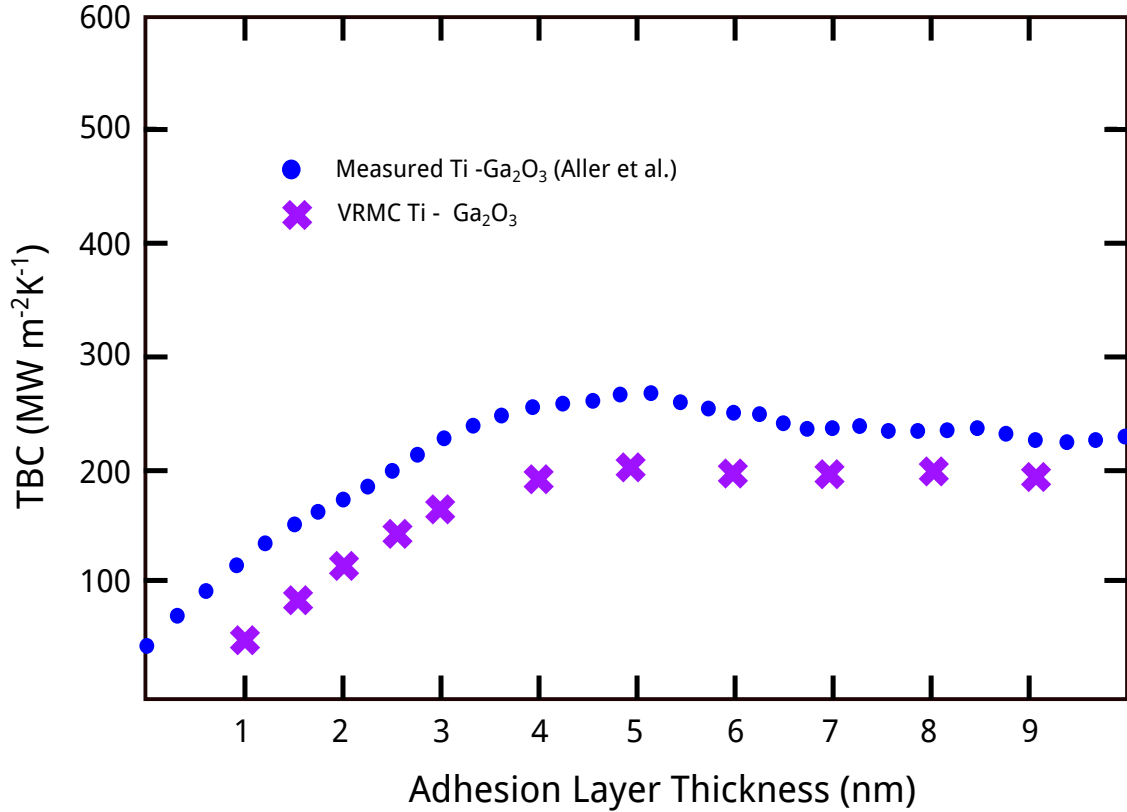
Figure 3.21: VRMC results for Ti/Ga_2O_3 interface with a Ga_2O_3 layer thickness of 400 nm and an increasing layer thickness for titanium. Results are compared to FDTR measurements of [42]. VRMC results under predict measured data moderately and follow a similar trend in layer thickness, with an increasing conductance until around 4 nm Ti.

3.5.4 Au/Ti/Ga$_2$O$_3$ Thermal Contact

To evaluate the effect of titanium as an adhesion layer, the VRMC method is performed sequentially for the layer thickness in increments of $\Delta L = 0.5$ nm. Results are presented in Figure 3.21 and compared to the frequency-domain thermoreflectance (FDTR) results of [42] Overall, there is a relatively good agreement with the measured trends. The magnitude of the TBC differs in the VRMC prediction by about 60 MW/m^{2}K, or approximately 30%. The predicted and measured values reach their peak values of $G_p = 190$ MW/m^{2}K and $G_p = 254$ MW/m^{2}K respectively, at around 4 nm in both cases. For the VRMC results, this corresponds to a Kapitza length of $L_k = 110$ nm which is over a factor of 3 improvement to the direct Au/Ga$_2$O$_3$ contact. This is a very significant improvement to the thermal

boundary conductance for engineering applications. Discrepancies between measured and predicted results are most likely due to the lack of inelastic scattering mechanisms considered at the boundary. It is also possible that the simulation would require a more dense reciprocal space mesh, beyond 12x12x12, for computing the anharmonic scattering rates however this is computational prohibitive.

3.5.5   Au/Cr/Ga$_2$O$_3$ Thermal Contact

For the chromium layer example, it is expected that the TBC will improve if the density of states model is sufficiently predictive and indeed the primary method of phonon transmission at the interface is due to elastic phonon-phonon scattering. The results for the chromium case, using the same simulation cell as the titanium example, are presented in Figure 3.22. Compared to both the Au/Ga$_2$O$_3$ contact and the Au/Ti/Ga$_2$O$_3$ contact, the effect chromium has on the TBC is significant with the plateau value at 5 nm being $G_p = 395$ MW/m^{2}K. This compares well with the measured value of $G_p = 454$ MW/m^{2}K at the same width, differing only by 13%. This corresponds to over a factor of 6 improvement to the Au/Ga$_2$O$_3$ contact and a corresponding Kapitza length of only 53 nm. This is a very large value for boundary conductance which significantly exceeds even many GaN interfaces [50]. This implies that in thermal engineering of Ga$_2$O$_3$ devices, the interface will not prove to be a significant obstacle. The trend seen in Figure 3.22 is consistent with the Al$_2$O$_3$ measurements but differ slightly with the Ga$_2$O$_3$ measurements. Notably, the peak at around 2 nm in the measured results is unusual. It was speculated in [42] that due to the high heat of formation of Ga$_2$O$_3$, it is likely that a thin amorphous layer is forming at the interface. This phenomena is not seen in the Al$_2$O$_3$ measurements due to the lower heat of formation found in Al$_2$O$_3$. Surface chemistry phenomena such as this will not be considered in simulation, and hence the peak is not present in the computed result.
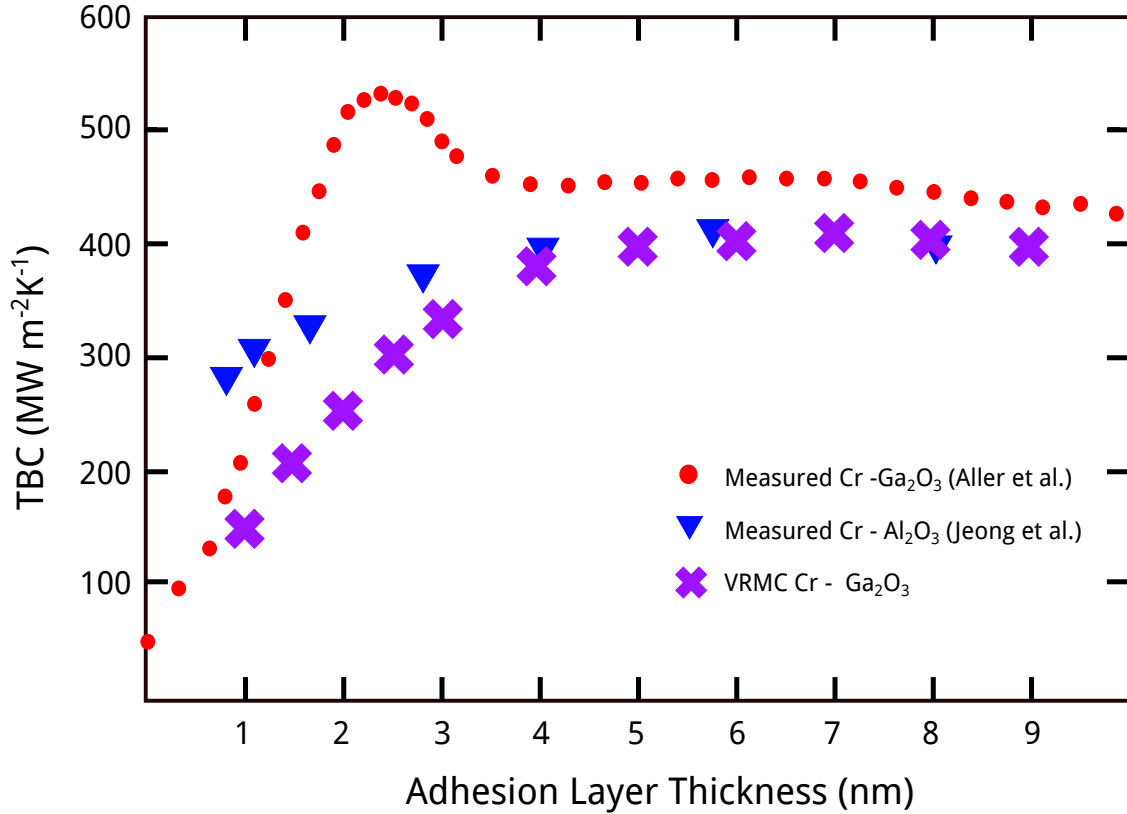
Figure 3.22: VRMC results for Cr/Ga_2O_3 interface with a Ga_2O_3 layer thickness of 400 nm and an increasing layer thickness for chromium. Results are compared to FDTR measurements of [42] as well the Cr/Al_2O_3 measurements for the same structure [49]. VRMC results under predict measured data moderately and reach a similar plateau value at 5 nm. The peak in the measured Cr/Ga_2O_3 results is predicted to be from amorphous layer formation[42]

3.5.6 Temperature Dependence

To investigate the temperature dependence of the TBC, the VRMC computation is fixed at the 4 nm plateau value for titanium and 5 nm plateau value for chromium and repeated for a series of temperatures between RT and 600 K. From the bulk thermal conductivity results in $\beta - Ga_2O_3$, it is not expected that there will be a sizable temperature dependence in the anharmonic scattering rates and hence the TBC will not be strongly temperature dependent. The results for both Ti and Cr interfaces as well as measured results is presented in Figure 3.23. Overall, the temperature dependence is small when considering only up to third-order phonon-phonon scattering mechanism. In general, it is possible that at higher temperatures (above 700 K), the effect of fourth-order phonon scattering may become more
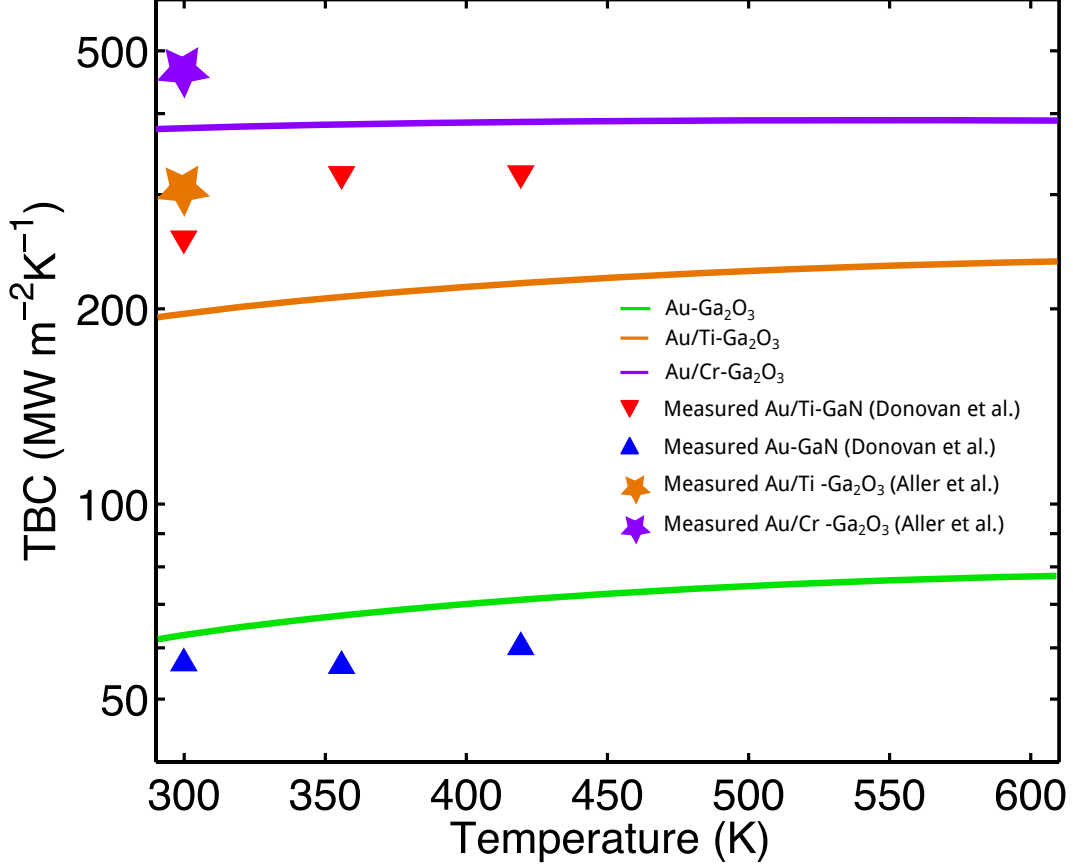
Figure 3.23: Thermal boundary conductance for fixed layer spacing as a function of temperature. GaN Measurements taken from [50] and $\beta - Ga_2O_3$ measurements from [42]

influential which has been reported to be the case for GaN [51].

3.5.7 Role of Electron-Phonon Interaction

Electronic contributions to the thermal conductivity were not considered so depending on the importance of the electron-phonon scattering channel at the interface, the transmission can be underrepresented compared to experiment. If the thermal conductance is expressed as G_{tot}, the contributions sum in parallel,

$$G_{tot} = (G_{e-p}G_p)/(G_{e-p} + G_p) \qquad (3.40)$$

The role of electron-phonon scattering at the interface is not fully understood however. Many authors have speculated that electron-phonon scattering at interface is negligible and

the interaction only becomes relevant for transport solely within the metal, and only phonon-phonon scattering is relevant at the boundary. Simultaneously however, comparisons between theory and experiment such as the results of this work, demonstrate an underestimation of TBC when electron-phonon interactions are neglected. Although the metals used in this study are known to possess a low electron-phonon coupling constant, the large range of phonon frequencies available in Ga_2O_3 lead to more numerous possible scattering channels involving an electron-phonon scattering event. However, it is difficult to draw a conclusion from this trend alone considering the complexity of the transport problem and the difficulty in characterizing the exact surface chemistry of a metal-dielectric interface in an experimental setup. As was mentioned, the possible formation of amorphous layers, can be difficult to observe but can influence the TBC and this phenomena will not appear in a computational model without explicit inclusion. Additionally, in a realistic setup, the surfaces will never truly make a perfect contact, and there will certainly be some degree of roughness at the interface. The surface roughness will contribute an additional scattering term in theory which will further increase the thermal resistance. In general, the problem is very difficult to solve without a fully coupled electron-phonon Monte-Carlo solver using first-principles inputs which is a considerably complex computational problem that has not yet been solved.

CHAPTER 4

THERMODYNAMICS AND MECHANICAL PROPERTIES

An analysis of the elastic and thermodynamic properties is critical for a complete under-standing of the mechanical stability of Ga_2O_3 . The elastic stiffness tensor characterizes the linear response to applied stresses and accurate values allow for the analysis of structural and lattice dynamical properties in an elastic continuum model. One common application of elastic constants for electronic device design is to predict the acoustic deformation po-tential. Recently, deformation potential estimation was used to predict the electron impact ionization coefficients.[52] However, due to the lack of available data on the elastic prop-erties of Ga_2O_3 the elastic properties of gallium nitride were used as a substitute. That approximation was justified under the assumption that under high electric field conditions the non-polar optical phonon contribution was negligible.[52] However, it has recently been shown that this non-polar optical phonon scattering is the dominant contribution to electron mobility,[53] and a full understanding of elastic properties is needed for such an analysis.

Unfortunately, measuring these quantities is quite challenging due to the variability of growth quality as well as the anisotropy of monoclinic crystals.[12, 54] Only recently, elastic stiffness constants were measured at room temperature[55] and also theoretically predicted.[14, 56] Since the proposed applications for Ga_2O_3 lead to a wide range of oper-ating temperatures and the scarcity of measured data, the temperature dependencies of the elastic properties are also considered in the present investigation.

Advances in first-principles DFT calculations have made robust computations for elastic constants in any crystal symmetry possible with minimal computational overhead.[57] In this work calculations were performed for the linear thermal expansion coefficient and elastic stiff-ness constants (C_{ij}) which are used to evaluate the complete set of elastic moduli including the bulk modulus, shear modulus Young's modulus, Vicker's hardness, and Poisson's ratio. Additionally, temperature effects are considered by use of the quasi-static approximation[58]

72

and further evaluation of the isothermal and isentropic C_{ij}.

More recently, Ga_2O_3 has become a material of great interest for its various applications in optoelectronics, e.g. it has been used in solar-blind UV photodetector applications[59] due to the wide optical bandgap. Characterizing the optical properties in practice is a challenge for low-symmetry crystals as they exhibit biaxial optical responses and possess significant birefringence. There have been several recent investigations detailing this intricate geometry dependence [60] as well as the incident wavelength dependence in the context of absorption spectra. The effects of mechanical strain have not been considered in the literature thus far but have been theorized to potentially play a significant role in optical characteristics [60] and are generally an area of great interest for the development of crystal growth methodologies[55].

The response of optical properties to strain is commonly known as the elasto-optic effect, or photoelastic effect, and is characterized by strain dependence of the dielectric function. Measurements of photoelasticity are notoriously difficult for even the simplest of crystals due to the many sets of strains that must be individually applied to resolve the tensor. For low-symmetry crystals with significant anisotropy it is challenging to control strain at the precision required for resolving measurements and it is challenging to distinguish the response in individual crystallographic directions. Optical interferometry can possibly be used, but requires a large number of measurements on precisely cut crystals for all orientations which is unrealistic for Ga_2O_3 at present. In this work calculations were performed from first-principles for the dielectric function spectrum under strained conditions to resolve the elasto-optic properties.

4.1 Methodology

In this work, a first principles based approach as implemented in the Quantum Espresso package using the projector augmented wave method is utilized. Comparisons are made between the effect of local density approximation (LDA) and the modified generalized gradient

approximation of Perdew-Burke-Ernzerof (GGA-PBEsol) on the elastic stiffness constants. A plane wave basis with a kinetic energy cut-off of 125 Ryd was used for all calculations. Brillouin zone integration was performed with a $16 \times 16 \times 8$ k-point grid for structural relaxation and $8 \times 8 \times 8$ grid for calculating the stress in the elastic constants calculations. Figure 3.2 shows the orientation of the monoclinic structure.

The method adopted here computes the stress tensor (σ_{ij}) directly from first principles after applying a strain (ε_{ij}) and uses the stress-strain form of Hooke's law, $\sigma_{ij} = C_{ijkl}\varepsilon_{kl}$ to compute the elastic stiffness constants.[61, 62] This approach was chosen over the "stress approach" [57] because it reduces the number of calculations required for a low symmetry structure such as the monoclinic phase being studied in this work. The ElaStic[57] software package is used to identify the required strained configurations for this crystal. Total energy calculations were then performed on these strained configurations and post-processed using ElaStic. Phonon calculations for determining the free-energy in the quasi-harmonic approximation (QHA) are done in the real-space finite-displacement supercell method as implemented in Phonopy[7]. Using this methodology, force-constants were computed using a $2 \times 2 \times 2$ supercell containing 80 atoms with a $4 \times 4 \times 3$ k-point grid. The phonon density of states was determined for seven volumes and used to compute the vibrational contribution to the Helmholtz free energy.

In the Voigt notation there are 13 independent elastic constants[63] for this structure and the elastic stiffness constants relate the stress and strain by

$$
\begin{pmatrix} \sigma_1 \\ \sigma_2 \\ \sigma_3 \\ \sigma_4 \\ \sigma_5 \\ \sigma_6 \end{pmatrix} = \begin{pmatrix} C_{11} & C_{12} & C_{13} & 0 & C_{15} & 0 \\ C_{21} & C_{22} & C_{23} & 0 & C_{25} & 0 \\ C_{31} & C_{32} & C_{33} & 0 & C_{35} & 0 \\ 0 & 0 & 0 & C_{44} & 0 & C_{46} \\ C_{51} & C_{52} & C_{53} & 0 & C_{55} & 0 \\ 0 & 0 & 0 & C_{46} & 0 & C_{66} \end{pmatrix} \begin{pmatrix} \varepsilon_1 \\ \varepsilon_2 \\ \varepsilon_3 \\ \varepsilon_4 \\ \varepsilon_5 \\ \varepsilon_6 \end{pmatrix} \tag{4.1}
$$

where σ_{1-3} represent normal stresses and σ_{4-6} shear stresses. The notation is consistent

with the axes definitions in Figure 3.2. This choice is not unique and some literature uses a second viable notation based on a different labeling of lattice vectors.

To minimize the set of strains required to fully determine C_{ij}, the universal linear-independent coupling strains are used which results in 5 strains for the monoclinic crystal for a given magnitude of Lagrangian strain. [64] The strain values chosen are $\eta = \pm 0.007$ and $\eta = \pm 0.013$ for all calculations as in the work by Shang et al..[61, 62] Finite temperature effects were considered by using the QHA which has been discussed in detail[65].

Elastic moduli were computed from the C_{ij} using the Voigt-Reuss-Hill method[66][67]. Vicker's Hardness (H_V) was computed using the simplified phenomenological model[68] which depends solely on the shear modulus. Sound velocities along different crystallographic directions were evaluated from C_{ij} and compared with those obtained directly from the phonon dispersion of Ga_2O_3 . [69]

4.1.1 Elastic stiffness

The methodology adopted in this work requires several steps which are briefly described. Firstly, the elastic stiffness constants at $0\,K$ can be determined using one of two methods, both of which require DFT calculations to be performed on a series of strained structures. The first method[57] uses the strain energy density vs strain relationship. This method only requires total energy to be computed for the strained structures. The method requires many energy calculations to be performed and is computationally expensive for low-symmetry structures. For this reason this work adopts the second method, which directly computes the stress tensor (σ_{ij}) from first principles after applying a strain (ε_{ij}) and uses the stress-strain form of Hooke's law, $\sigma_{ij} = C_{ijkl}\varepsilon_{kl}$, to compute elastic stiffness constants (C_{ijkl}). This reduces the number of calculations required for low symmetry structures[57]. Choosing a minimal set of strains to apply is heavily dependent on crystal symmetry. Hence, in this work the "universal linear-independent coupling strains" (ULICS) [64] were utilized. The ULICS basis is a linearly independent set of strains that span the "strain space" and consequently

represent the minimal set of strains required to fully determine C_{ij}. For monoclinic this results in 5 strains to apply to the crystal for a given magnitude. Applying several values of strain is required in practice to assure the result is converged. The values of Lagrangian strain used range from $\eta = \pm 0.007$ and $\eta = \pm 0.013$ for all calculations performed here.

4.1.2 Quasi-harmonic approximation

To consider finite temperature properties using DFT, this work utilizes the quasi-harmonic approximation. This approximation assumes the dominant anharmonic contribution to the phonon disperion be contained within the volumetric expansion rather than the explicit temperature dependence of anharmonic force constants. This allows the Helmholtz energy to be written as:

$$F(V,T) \approx E(V) + F_{\text{phonon}}(V,T) \tag{4.2}$$

Where $E(V)$ is the equation of state function and $F_{\text{phonon}}(V,T)$ is the free energy contribution due to vibrations about the ground state. Both contributions will require DFT calculations for several unit-cell volumes. The former is determined by fitting total-energy of the various volume configurations to an equations of state (EOS), while the latter contribution requires the phonon density of states to be computed at these volumes. Bulk modulus (B_0), volume-temperature relationship $V(T)$, and heat capacity at constant pressure (C_P) or constant volume (C_V) can be determined from the computed $F(V,T)$. Once the free-energy function is determined, minimizing results in the Gibbs free-energy function which can be used within several thermodynamical relations for bulk thermodynamic quantities, such as bulk modulus:

$$B = V \left(\frac{\partial^2 F}{\partial V^2} \right)_T \tag{4.3}$$

heat capacity at constant pressure,

$$C_P = -T \left(\frac{\partial^2 G}{\partial T^2} \right)_P \tag{4.4}$$

76

and heat capacity at constant volume,

$$C_V = -T \left(\frac{\partial^2 F}{\partial T^2} \right)_V \tag{4.5}$$

These quantities are used to compute the bulk thermal expansion coefficient α_V:

$$C_P(T) - C_V(T) = \alpha_V^2 V(T) T B_0(T) \tag{4.6}$$

QHA analysis is necessary for determining the volumetric thermal expansion relationship and subsequent thermodynamic properties such as heat capacity. It is also capable of predicting bulk modulus as a function of temperature which can be compared to a similar prediction made by direct computation of elastic stiffness constants. With an accurate representation of the volumetric thermal expansion, it is then possible to estimate the temperature dependence of mechanical properties such as elasticity withing the so-called quasi-static approximation. Additionally, the QHA enables the computation of a macroscopic Gruneisen parameter without needing to consider microscopic behaviors of interatomic force-constants. Hence, a direct comparison between the anharmonic force-constant approach presented in the previous chapter can be made with the macroscopic thermodynamic properties presented here. This type of calculation requires successive phonon calculations to be performed within DFT and the reader is referred to the previous chapter for the phonon calculation details. Generating the strained-unit cells required to resolve a volumetric dependence entails applying hydrostatic strain followed by geometric relaxation within DFT. It is important that a hydrostatic strain is used to adjust the volume as this ensures a minimal change lattice parameters while retaining the desired volume change. Significant changes to any one lattice parameter in an anisotropic crystal structure can lead to improper geometry optimization that can more readily result in an unintended, and possibly artificial, phase transformation. The determined free energy curves from a series of 20 different volumes in which phonon properties are computed is presented in Figure 4.1.

The corresponding bulk modulus as a function of temperature in the QHA is now presented in Figure 4.2. The $0\,\mathrm{K}$ value of $B_0 = 166.5\,\mathrm{GPa}$ compares relatively well to the
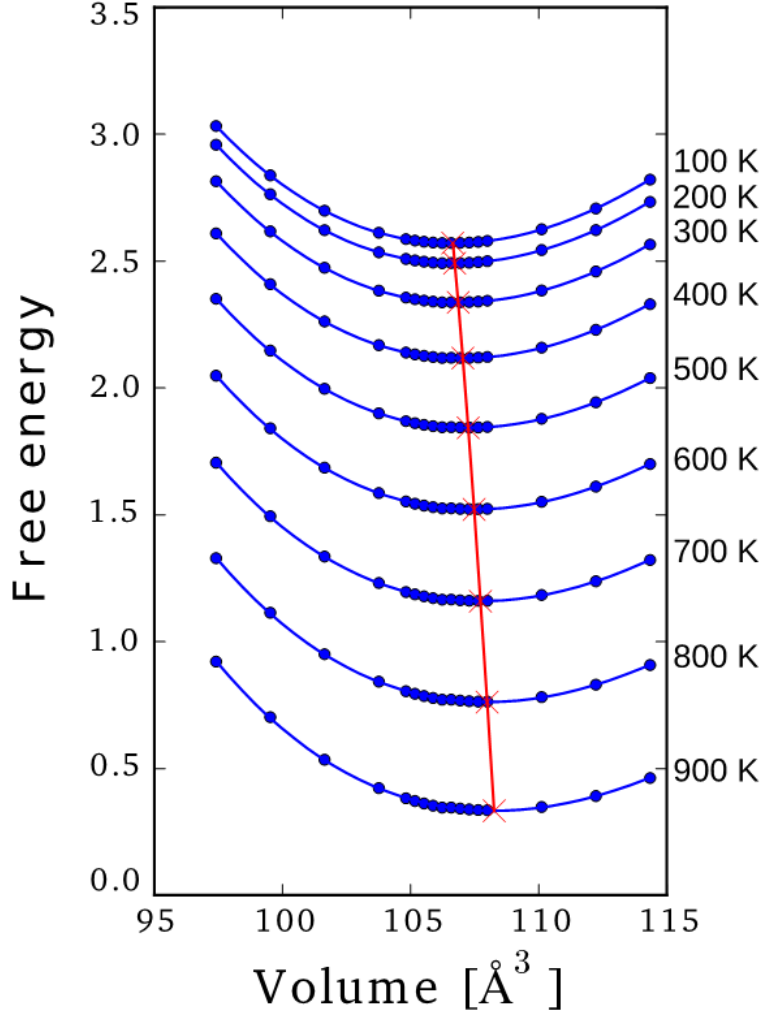
Figure 4.1: Free-energy curves computed within QHA for $\beta - Ga_2O_3$ and minimized to determine the Gibbs free energy function (red line).

recently measured data of Ref.[70] which gives a value of $B_0 = 182.6\,\text{GPa}$. This value is notably lower than $\theta - Al_2O_3$ which possesses the same crystal structure and spacegroup, where $B_0 = 202.7\,\text{GPa}$ [70]. This is not particularly surprising considering the volume of $\theta - Al_2O_3$ is as much as 20% lower than its gallium counterpart. The combination of a smaller volume and lighter atoms leaves the crystal with less overall compressibility and stiffer bonds which is seen in the significantly larger debye temperature of $\theta - Al_2O_3$ [61].
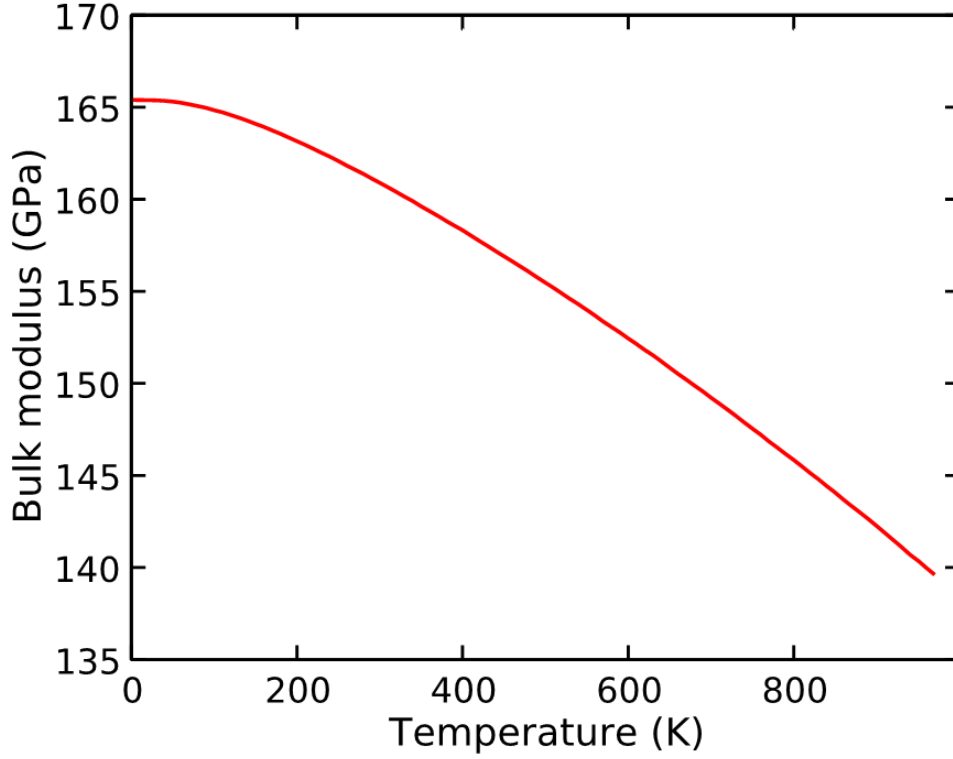
Figure 4.2: Bulk modulus computed within QHA for $\beta - Ga_2O_3$. At $0\,K$ the bulk modulus value is $B_0 = 166.5\,GPa$

4.1.3 Microscopic vs Macroscopic Gruneisen

To characterize the anharmonicity of the crystal in both the QHA and the phonon-phonon scattering frameworks, the Gruneisen parameters can be computed. Large Gruneisen parameters are associated with strong anharmonicity where atomic motion breaks periodicity of normal modes. In general they are a material property which can be defined in several different ways which measure how the phonon frequencies change with volume. They can be computed microscopically using the 3rd order IFCs,

$$\gamma_j(\mathbf{q}) = -\frac{1}{6\omega_j^2(\mathbf{q})} \sum \Phi_{\alpha\beta\gamma}^{0\kappa;l'\kappa';l''\kappa''} \frac{e_{\alpha\kappa}^{j*}e_{\beta\kappa'}^{j}}{\sqrt{M_\kappa M_\kappa'}} \times r_{l''\kappa''\gamma} e^{i\mathbf{q}\cdot\mathbf{R}_{l'}} \tag{4.7}$$

where in this context they act as a measure of how the restoring forces of harmonic motion change as the crystal expands. For direct comparison with measured data, it is more easy

to express this in an averaged scalar form.

$$\overline{\gamma} = \frac{\sum \gamma_j C_V^j}{\sum C_V^j} \tag{4.8}$$

Additionally, the effect of a changing volume can be computed more directly in the QHA framework,

$$\gamma_j(\mathbf{q}) = -\frac{\partial \ln \omega_j(\mathbf{q})}{\partial \ln V} \tag{4.9}$$

with the averaged scalar form being determined by,

$$\overline{\gamma} = B\frac{\alpha V}{C_V} \tag{4.10}$$

Computing the Gruneisen parameters using both of these methods allow for a more direct validation and comparison to be performed between the microscopic and macroscopic calculations. This should serve as a validation of convergence of the 3rd order IFCs as well as a check that the volumetric dependence within the QHA is consistent. The direct comparison of the averaged scalar quantities is presented in Figure 4.3. Overall the parameters were relatively small which is expected in stiff crystals. More importantly, there is a very consistent match between the two methods for a modest range of temperatures. The growing disparity for increasing temperatures is likely due to the onset of higher order anharmonic effects in the microscopic formulation arising from fourth-order phonon scattering. This effect although small can be important to consider for high temperatures. However in this case, the temperatures where the higher-order scattering become relevant would approach the phase transition temperatures. The spectrum averaged mode Gruneisen parameters is provided in Figure 4.4 where a minimal temperature dependence is seen.

4.1.4   Linear Thermal Expansion

Finite temperatures introduce anharmonic effects due to thermal expansion as has been demonstrated in the previous section. This is especially the case in a monoclinic unit-cell, where a high degree of anisotropy in the thermal expansion is expected along crystallographic
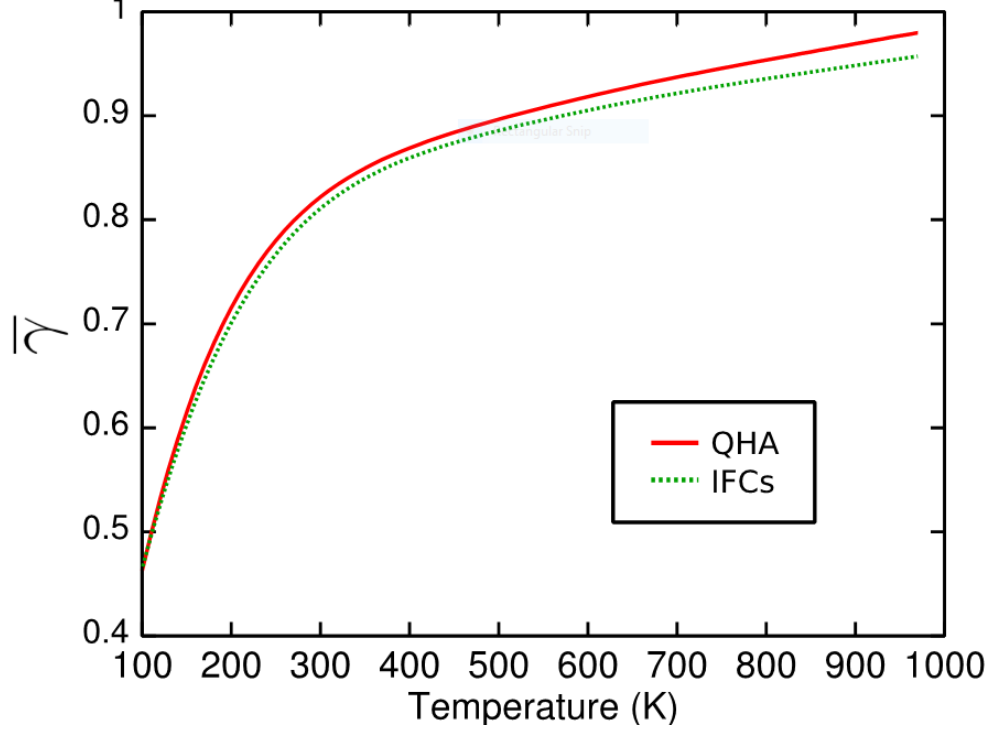
Figure 4.3: Average value of Gruneisen parameter of $\beta - Ga_2O_3$ computed macroscopically through the QHA method compared to the microscopic formulation utilizing 3rd order IFCs

directions. Determining the linear thermal expansion coefficients (TEC) can be done by the quasi-static approximation[58]. In this approximation, the thermal expansion is determined by the optimized lattice vectors for several strained configurations of the unit-cell at $0\,K$ combined with the volumetric thermal expansion determine with the QHA. The strain definition of thermal expansion at constant pressure[63] (using Voigt notation),

$$\alpha_i = \left(\frac{\partial \varepsilon_i(T)}{\partial T} \right)_P \tag{4.11}$$

Depending on the symmetry of the crystal, there will be applied strains ε_j which are uniquely parallel to an individual direction j. Along these directions, the linear thermal expansion (ε_j) relation and their corresponding temperatures defined by the QHA $V(T)$. Using the computed $0\,K$ values for $V(\varepsilon_j)$ with the inverse relationship $T(V)$ produces a form of the temperature dependence $T(V(\varepsilon_j))$ that relates to a specific direction through its corresponding strain.
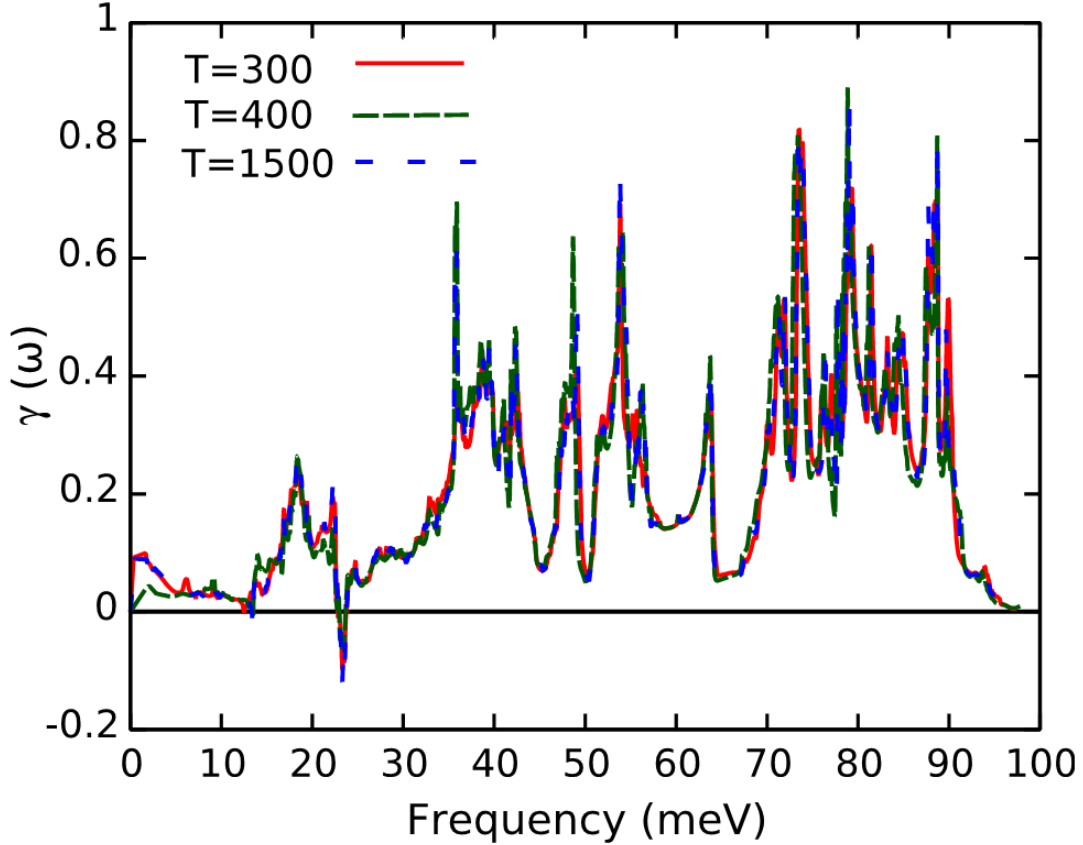
Figure 4.4: Frequency-dependent average mode Gruneisen parameters in $\beta - \mathrm{Ga_2O_3}$ for a sequence of temperatures computed within QHA.

4.1.5 Isothermal elastic stiffness

Calculating the temperature dependence quasi-statically is done analogously to the linear thermal expansion. Elastic stiffness constants, $C_{ij}(V)$, is computed for several volumes and combined the quasi-harmonic $V(T)$. Then, $C_{ij}(T)$ can be computed by interpolation.

4.1.6 Isentropic elastic stiffness

Often it is the case that experimental measurements for C_{ij} at high temperatures are not isothermal but isentropic. For example, the commonly used resonance method[61] results in higher elastic wave speed relative to the heat diffusion, which results in adiabatic (constant entropy for a reversible system) behavior. Therefore, this work uses an expression to compute

the isentropic stiffness constants, $C_{ij}^S(T)$ in terms of the isothermal constants $C_{ij}^T(T)$, the heat capacity C_V and the linear thermal expansion α_j[71]:

$$C_{ij}^S = C_{ij}^T + \frac{TV\lambda_i\lambda_j}{C_V} \tag{4.12}$$

$$\lambda_i = -\sum_{k=1}^{6} \alpha_k C_{ik}^T \tag{4.13}$$

4.1.7 Elastic moduli

Using C_{ij} and the corresponding elastic compliance S_{ij}, the bulk modulus (B) and shear modulus (G) can be computed the Voigt-Reuss-Hill method[66]. Voigt's approximation considers a uniform strain as opposed to a uniform stress as in Reuss' approximation. The approximations serve as a lower and upper bound respectively. Hence, the average (Hill approach) of these two approximation will be used. These approximations are shown below[67]

$$B_{\text{Voigt}} = \frac{1}{9}((C_{11} + C_{22} + C_{33}) + \frac{2}{9}(C_{12} + C_{13} + C_{23}))$$

$$G_{\text{Voigt}} = \frac{1}{15}((C_{11} + C_{22} + C_{33}) - (C_{12} + C_{13} + C_{23}))$$

$$+ \frac{1}{5}(C_{44} + C_{55} + C_{66})$$

$$B_{\text{Reuss}} = [(S_{11} + S_{22} + S_{33}) + 2(S_{12} + S_{13} + S_{23})]^{-1}$$

$$G_{\text{Reuss}} = 15[4(S_{11} + S_{22} + S_{33}) - 4(S_{12} + S_{13} + S_{23})$$

$$+ 3(S_{44} + S_{55} + S_{66})]^{-1}$$

$$B_{\text{Hill}} = \frac{1}{2}(B_{\text{Reuss}} + B_{\text{Voigt}})$$

$$G_{\text{Hill}} = \frac{1}{2}(G_{\text{Reuss}} + G_{\text{Voigt}})$$

Poisson's ratio (ν) and Young's modulus (E) are then computed with

$$\nu = \frac{1}{2}\left[\frac{B - \frac{2}{3}G}{B + \frac{1}{3}G}\right] \tag{4.14}$$

$$E = \frac{9BG}{G + 3B} \tag{4.15}$$

Lastly, Vicker's Hardness (H_V) can be computed using the simplified phenomenological model [68] which depends solely on the shear modulus,

$$G = 6.78 \, H_V \tag{4.16}$$

This model has been demonstrated to be effective in covalent materials such as oxides[68].

4.1.8 Sound velocities

Thermodynamic quantities can often be accurately estimated from sound velocities and the Debye temperature (Θ_D). Additionally, they are easily measured and thus can support the validity of the computed elastic constants. In the bulk case, there are simple relationships depending only on previous calculations for bulk and shear modulus

$$\Theta_D = \frac{h}{k} \left[\frac{3n}{4\pi} \left(\frac{N_A \rho}{M} \right) \right]^{1/3} v_m \tag{4.17}$$

where the mean velocity is written as

$$v_m = \left[\frac{1}{3} \left(\frac{2}{v_l^3} + \frac{1}{v_t^3} \right) \right]^{-1/3} \tag{4.18}$$

with the longitudinal velocity, $v_l = \sqrt{(B + \frac{4}{3})/\rho}$, and transverse velocity $v_t = \sqrt{G/\rho}$. Obtaining the sound velocity along a specified direction is more complicated and requires the solution of the Christoffel equation [72]:

$$(\Gamma_{ij} - \rho v^2 \delta_{ij}) u_j = 0 \tag{4.19}$$

$$\Gamma_{ij} = \sum_{k=1}^{3} \sum_{m=1}^{3} C_{ikjm} l_k l_m \tag{4.20}$$

where l_k and l_m represent the direction cosines, u_j is the displacement vector, and v is the sound velocity eigenvalue that is solved for by diagonalization. The direction cosines in

in our orientation are with respect to the x-axis, $l_1 = \cos\alpha$, y-axis, $l_2 = \cos\beta$ and z-axis, $l_3 = \cos\gamma$. For a monoclinic crystal, the solution in an arbitrary direction will result in a two mixed modes (labelled v_- and v_+ for the slower and faster respectively), and a transverse mode (v_t)[69]. Along the crystallographic directions, the solutions can be expressed as:

[100] :

$$v_t = \sqrt{C_{66}/\rho}$$

$$v_+ = \sqrt{\frac{(C_{11} + C_{55}) + (C_{11}^2 + 4C_{15}^2 - 2C_{11}C_{55} + C_{55}^2)^{1/2}}{2\rho}}$$

$$v_- = \sqrt{\frac{(C_{11} + C_{55}) - (C_{11}^2 + 4C_{15}^2 - 2C_{11}C_{55} + C_{55}^2)^{1/2}}{2\rho}}$$

[010] :

$$v_t = \sqrt{C_{22}/\rho}$$

$$v_+ = \sqrt{\frac{(C_{44} + C_{66}) + (C_{44}^2 + 4C_{46}^2 - 2C_{44}C_{66} + C_{66}^2)^{1/2}}{2\rho}}$$

$$v_- = \sqrt{\frac{(C_{44} + C_{66}) - (C_{44}^2 + 4C_{46}^2 - 2C_{44}C_{66} + C_{66}^2)^{1/2}}{2\rho}}$$

[001] :

$$v_t = \sqrt{C_{44}/\rho}$$

$$v_+ = \sqrt{\frac{(C_{33} + C_{55}) + (C_{33}^2 + 4C_{35}^2 - 2C_{33}C_{55} + C_{55}^2)^{1/2}}{2\rho}}$$

$$v_- = \sqrt{\frac{(C_{33} + C_{55}) - (C_{33}^2 + 4C_{35}^2 - 2C_{33}C_{55} + C_{55}^2)^{1/2}}{2\rho}}$$

4.2 Quasiharmonic Approximation

Calculated lattice parameters for both LDA and GGA as well as their respective bulk moduli determined from our QHA calculations, are given in Table 4.1.

	a	b	c	β	B	
LDA	12.181	3.029	5.772	103.73	0 K:	176
					300 K:	172
					950 K:	157
GGA	12.276	3.054	5.813	103.71	0 K:	161
					300 K:	157
					950 K:	136
Expt.	12.233	3.038	5.807	103.82	199	

Table 4.1: Calculated lattice parameters (Å) at $0\,K$ and bulk moduli, B (GPa), at $T = 0, 300, 1000\,K$ as calculated within the QHA. Results using LDA and GGA functionals as well as the measured values of Ref. [73] are listed.

Unsurprisingly, lattice parameters calculated using GGA are over-estimated while the LDA parameters are under-estimated. GGA over-prediction is a common phenomena,[33] and in this case the LDA resolves a more accurate value for the bulk modulus just as it does in the Al_2O_3 isostructure.[61] Overestimation of lattice constants is important to note as it
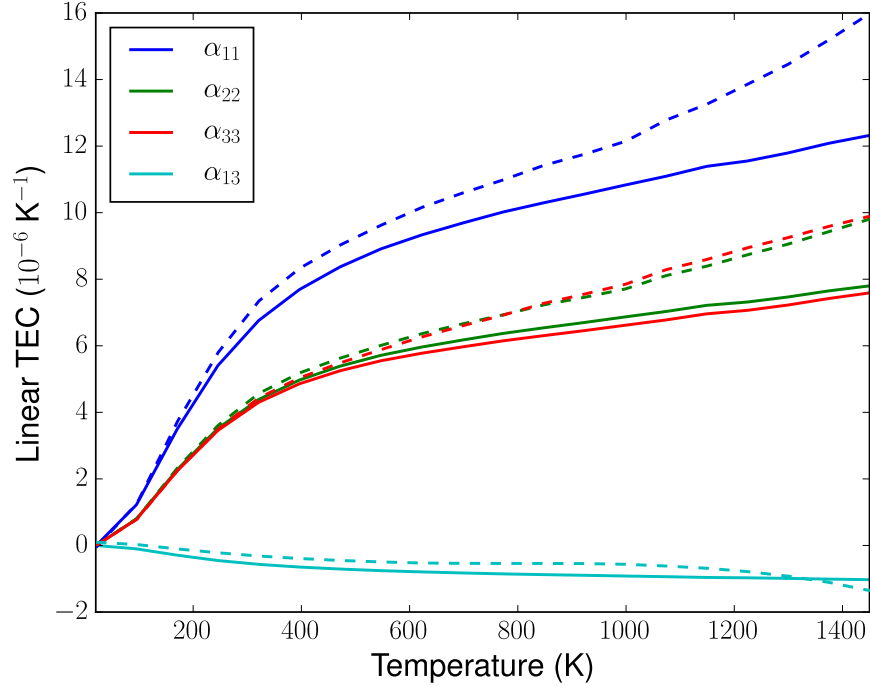
Figure 4.5: Linear thermal expansion coefficient for LDA (solid lines) and GGA (dashed lines) calculations corresponding to applied strains ε_i as a function of temperature. Due to symmetry, ε_4 and ε_6 are zero.

can lead to larger changes in the thermal expansion.

Linear thermal expansion for the applied strains was calculated for both GGA and LDA. The results are summarized in Figure 4.5. As per our previously defined monoclinic orientation, [31] an applied strain ε_2 is parallel to the b-direction and ε_3 to the c-direction. Using these definitions, the linear TEC in the b and c direction can be written as $\alpha_b = \alpha_{\varepsilon_2}$ and $\alpha_c = \alpha_{\varepsilon_3}$. Similar values from experimental measurements of ($\alpha_b = 3.37 \times 10^{-6} \, \text{K}^{-1}$ and $\alpha_c = 3.15 \times 10^{-6} \, \text{K}^{-1}$) and ($\alpha_b = 4.2 \times 10^{-6} \, \text{K}^{-1}$ and $\alpha_c = 4.2 \times 10^{-6} \, \text{K}^{-1}$) have been reported previously.[22, 54] In both measurements the lattice constants were fit as linear functions of temperature, yielding single temperature-independent TEC values that are considered to be valid over approximately $100 - 700\text{K}$[54]. The LDA functional is found to more accurately predicts measured values. This can be attributed to the GGA over-estimating the lattice constants[33]. The origin of the anisotropy in the TEC is likely to be purely geometric[54].

the heat capacity at constant pressure (C_p) and volume (C_V) are presented in Figure 4.6 and compared to [20] where good agreement is found.

Heat capacity in general is an important indicator of thermal performance in a semiconductor for use in power electronics. It is a parameter which represents the amount of thermal energy which can be stored in the material, hence it directly effects the thermal management and subsequent performance of the device. Comparing to Gallium Nitride, a commonly used power electronic material with a thermal conductivity exceeding 200 W/mK, the heat capacity is actually very similar. This is somewhat surprising when only considering the phonon dispersion and crystal complexity. There is a significantly more complex crystal structure in Ga_2O_3 which contains 30 phonon modes compared to GaN which only has 12 phonon modes due to the 4 atom hexagonal unit cell. The number of modes has a direct impact on the total volumetric heat capacity, as the more phonon modes available, the more energy can be stored. In fact, the heat capacities only differ by less than 20% which does not explain the significant disparity (an entire order of magnitude) in thermal conductivities. It
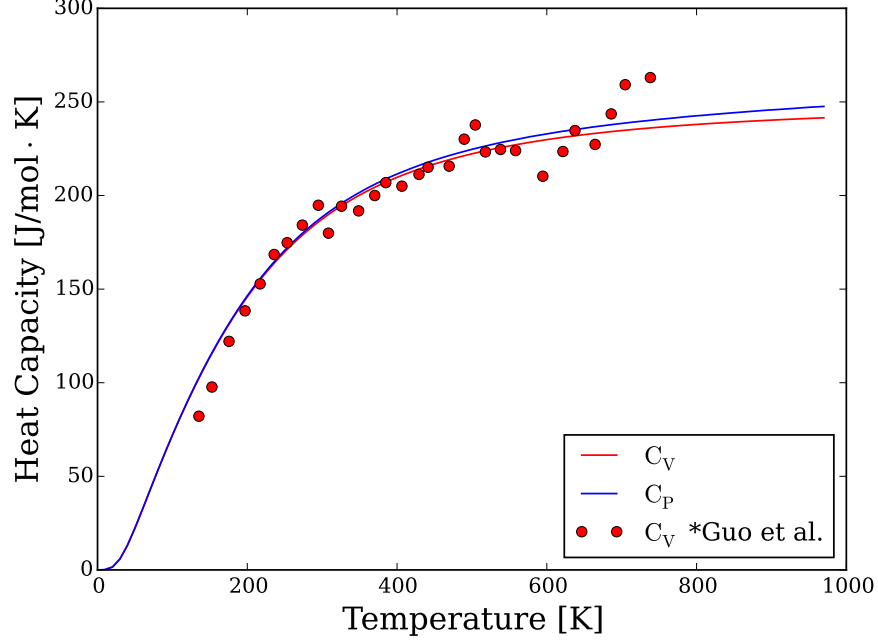
Figure 4.6: Heat capacity for $\beta - \text{Ga}_2\text{O}_3$ at constant pressure (blue) and constant volume (red) computed within the QHA compared to recently measured data of [20].

can thus be inferred that the average phonon lifetime in GaN is likely to be significantly higher in GaN than Ga_2O_3 and this higher lifetime leads to more thermal energy storage before phonon-phonon scattering occurs and heat is dissipated or transported through low energy acoustic modes. This explanation is consistent with the phonon dispersion of GaN which shows a significant bandgap. These gaps limit the anharmonic phase space for phonon-phonon scattering events and thus create less resistance from phonon scattering and a higher overall thermal conductivity regardless of the heat capacity [20].

4.2.1   Mechanical and elastic properties

The 13 independent elastic stiffness constants for Ga_2O_3 are listed in Table 4.2 for the DFT equilibrium value ($0\,\text{K}$) using both LDA and GGA exchange correlation functionals. Our results are compared to the recent C_{ij} calculations that used LDA[56] and GGA.[14] GGA tends to underestimate C_{ij} as compared to LDA since LDA also predicts smaller cell sizes. [61, 62] The three principle elastic constants C_{11}, C_{22} and C_{33} compare closely with

| | This Work | | Ref. [14] | Ref. [56] | Ref. [55] | Ref. [70] | $\theta - Al_2O_3$ [61] |
	LDA	GGA	GGA	LDA	Expt.	Expt	Expt
C_{11}	237.9	222.0	223.1	237	238	240	283
C_{22}	347.9	327.3	333.2	354	359	349	420
C_{33}	356.7	333.6	330.0	357	346	345	435
C_{44}	66.7	58.8	50.3	54	49	48	86
C_{55}	79.5	78.3	68.6	67	91	87	104
C_{66}	112.4	108.4	94.2	95	107	103	124
C_{12}	139.1	125.2	116.5	125	130	128	119
C_{13}	118.8	112.9	125.3	147	152	160	159
C_{23}	92.6	79.9	75.0	95	78	72	83
C_{15}	-1.8	-1.7	-17.4	-18	-4	-1.6	-30
C_{25}	5.6	5.2	12.2	11	2	0.3	12
C_{35}	7.8	7.0	7.3	6	19	1	16
C_{46}	9.1	9.0	17.4	19	6	5	23

Table 4.2: Comparison of calculated elastic stiffness constants C_{ij} (GPa) of $\beta - Ga_2O_3$.

the corresponding references. The remaining diagonal constants C_{44}, and C_{66} are larger within our approach while C_{55} is slightly smaller. The off-diagonal elastic constants show significant variation among the reports.

There is a notable difference between the LDA and GGA functionals predicted results which is an expected disparity. This can be attributed to the predicted lattice constants using each functional, where the LDA resolves a closer approximation to the measured lattice constant. As such, it can be seen that the LDA approximation more accurately matches the experimentally measured results. It is worth pointing out however that there is a relative spread in Table 4.2 within the off-diagonal portions of the tensor where the shearing strains modulate the anisotropy of the structure. To resolve these tensor components, many measurements must be performed on several different samples cut in precise configurations to encapsulate the proper crystallographic orientation. This very complex measurement has only very recently been achieved in the work of [70].

From these computed stiffness constants, the effect of anisotropy can be analyzed in

(a) (001)-plane   (b) (010)-plane
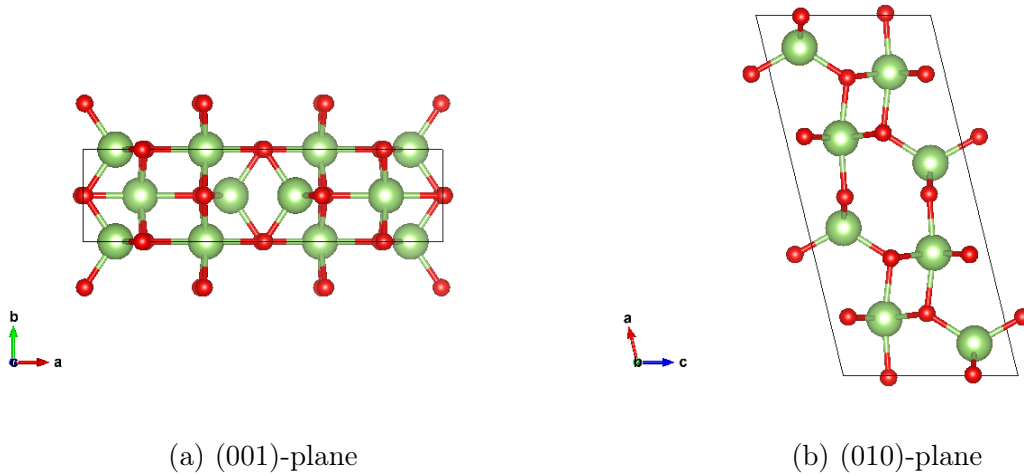
Figure 4.7: Crystallographic orientations of $\beta - \mathrm{Ga_2O_3}$ planes

more detail. One notable feature which stands out is the significant disparity between the C_{11} and C_{22} or C_{33} values. There is a nearly 30% decrease in the value of the stiffness constant in the [100] direction implying a higher compressibility along the x-direction and weaker chemical bonding along that direction. Referring to Figure 4.7a, it is seen that the [100] direction aligns with the largest number of octahedrally coordinated Gallium atoms (as opposed to the alternative tetrahedral sites). These octahedral polyhedra are more stable and will resist deformation. Application of a strain along this direction will result in less deformation of these polyhedra than along for example the [010] direction as seen in Figure 4.7b. This will lead to a higher resistance to strain deformation along the [010] which in turn results in a lower compressibility. This concept applies similarly to explaining the anisotropy in thermal conductivity, where the [100] direction also exhibits the lowest thermal conductance. This is consistent with the idea that a higher compressibility along this direction will allow for a lower frequency oscillation to occur in atomic vibrations due to the lower rigidity of the bonds. The octahedrally coordinated Gallium atoms can vibrate more freely with less returning forces due to the increased ability to compress without perturbing the coordination polyhedra. To illustrate the significant anisotropy, the Young's modulus ellipsoid is projected along each plane and presented in Figure 4.8. This anisotropy is

(a) (yz)-plane   (b) (xz)-plane   (c) (xy)-plane
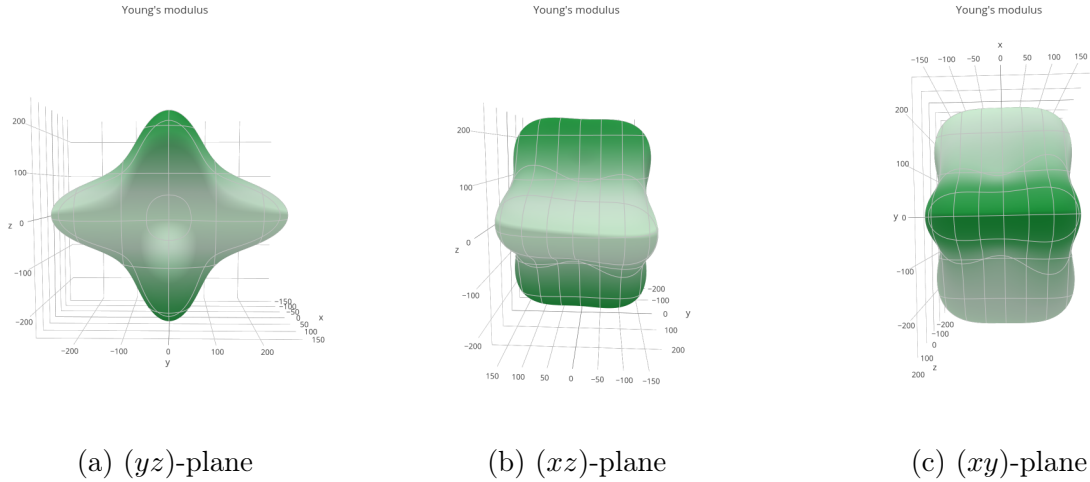
Figure 4.8: Tensor projection of Youngs modulus of $\beta - \mathrm{Ga_2O_3}$

important to consider for engineering purposes where directional phenomena can be utilized to control material properties. Conversely, it is also important to be aware of for unintended effects as may be the case when forming thin-film surfaces along certain orientations. It is seen in the figure that the [100] or x direction contains a significantly lower Young's modulus value then the [010] and [001] directions. This behavior is consistent with the anisotropy also calculated within the elastic stiffness constants. According to the results of [70], this behavior is also found in $\theta - \mathrm{Al_2O_3}$, which possess the same spacegroup. However, for similar monoclinic structures such as $\mathrm{BiMnO_3}$ this degree of anisotropy is not seen. This alludes to the anisotropy not being due to geometry alone and likely has more to due with the nature of the chemical bonding. This discrepancy is investigated in further detail by considering the linkage of the coordination polyhedron of each material. In Figure 4.9 the polyhedral linkage is illustrated and it can be seen that among the two distinct species of Gallium atoms, the octahedrally coordinated variety has a unique linkage network along the [100] direction which is not seen along the other primary crystallographic directions. Specifically, the octahedral polyhedron share edge with one another along [100] which will likely lead to higher binding energies. Comparing to the $\mathrm{BiMnO_3}$ system with similar crystallography, the linkage is vastly different as shown in Figure 4.10. None of the octahedrally coordinated cations' polyhedron
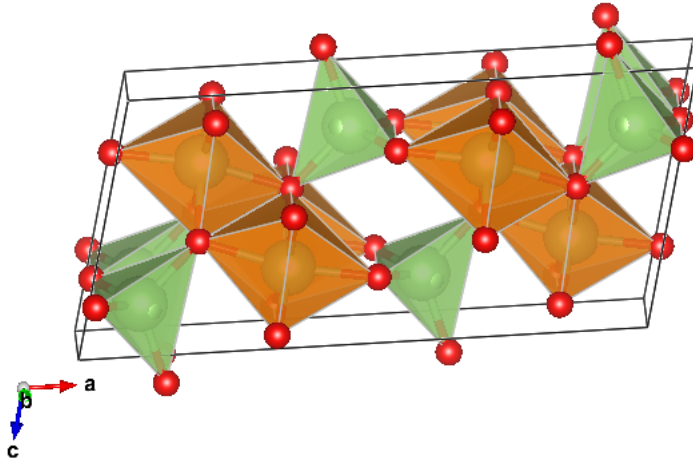
Figure 4.9: Monoclinic $\beta-\mathrm{Ga_2O_3}$ polyhedral linkage illustrating the unique bonding mechanism between octahedrally coordinated Gallium atoms. Edges of the octahedrally coordinated Gallium atoms' polyhedrons are shared.

have any shared edges or faces. This phenomena is analyzed in more detail in [70], where the authors speculate that the [100] direction is able to produce a longitudinal deformation with less bond length changes among cation-anion due to the flexibility of the linkage to bend between tetrahedron and octahedron. It was also revealed in this work that the bondlength change along this direction to achieve a set value of strain is notably smaller than that of the [010] and [001] directions. This behavior is not seen in $\mathrm{BiMnO_3}$ which is further verified by the projections of the Youngs' Modulus ellipsoid presented in Figure 4.11 which shows very little relative anisotropy.

It is also interesting to note the anisotropy reported on here matches the anisotropy seen within the thermal conductivity tensor, where the [100] direction demonstrates a notably smaller thermal conductivity (nearly half of the [010]). This anisotropy is visible in the phonon dispersion and leads to less acousto-optical gaps in the [100] which leads to an increased likelihood of anharmonic scattering events which provide thermal resistance. To consider the finite temperature effects that may be present in the elastic moduli, the isothermal and isentropic C_{ij} for $\beta-\mathrm{Ga_2O_3}$ were predicted and are plotted in Figure 4.12 as a
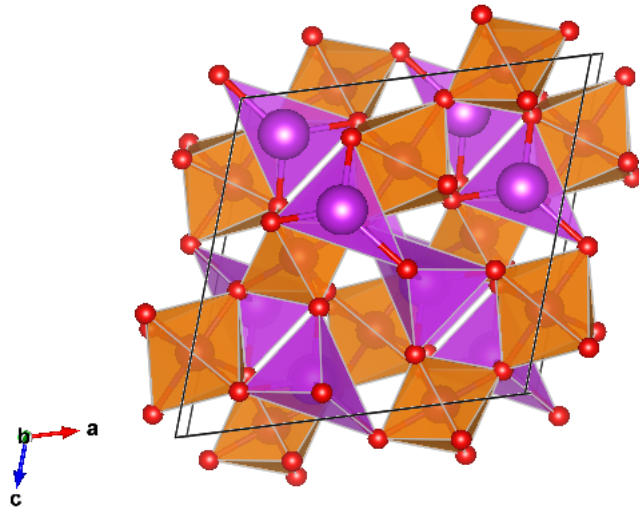
Figure 4.10: Monoclinic BiMnO3 polyhedral linkage contrasts the behavior seen in $\beta - $ Ga$_2$O$_3$ regardless of the material possessing the same crystal type. There are no shared edges among the octahedrally coordinated cations' polyhedron which is predicted to be the cause of the anisotropy difference.

(a) (yz)-plane   (b) (xz)-plane   (c) (xy)-plane
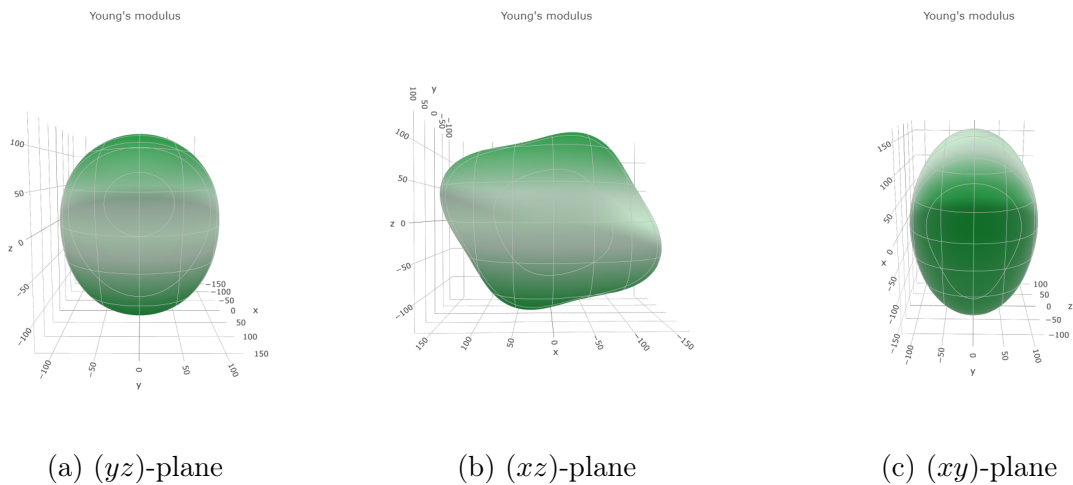
Figure 4.11: Tensor projection of Youngs modulus of Monoclinic BiMnO3 illustrating the significantly lower anisotropy compared to similar monoclinic structure $\beta - $ Ga$_2$O$_3$
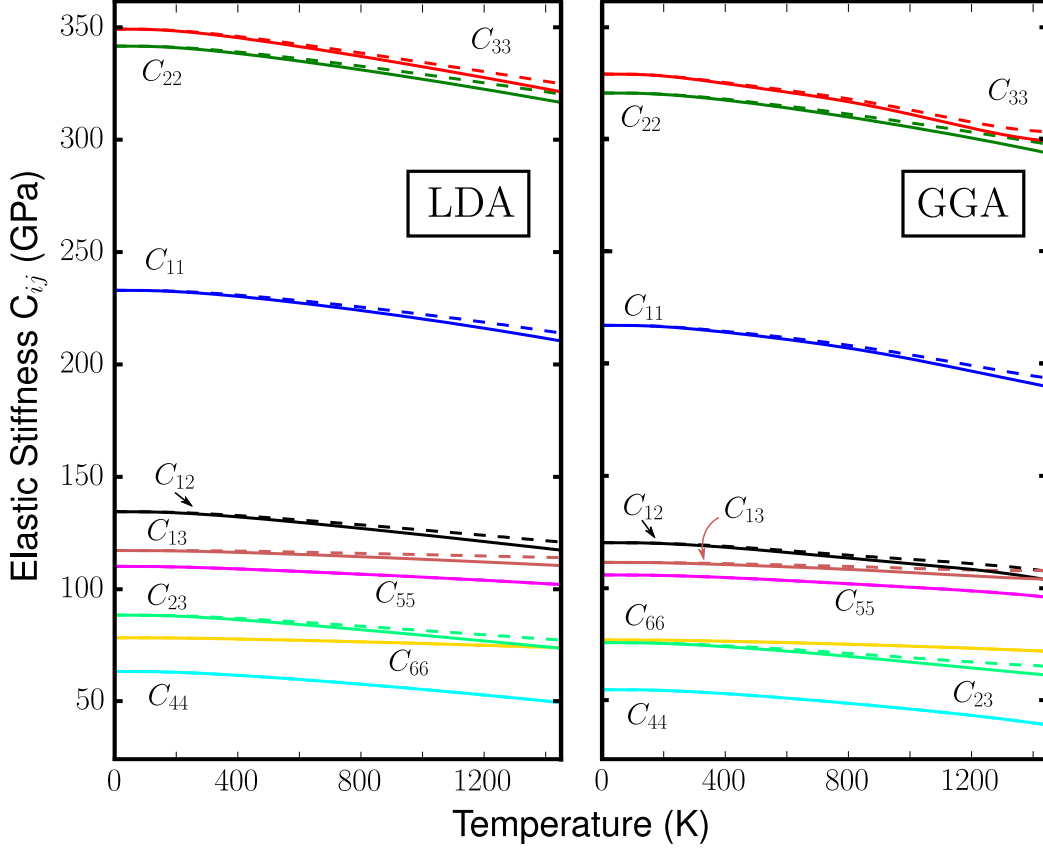
Figure 4.12: Isothermal (solid) and isentropic (dashed) elastic stiffness constants for LDA (left) and GGA (right) functionals for $\beta - \mathrm{Ga_2O_3}$.

function of temperature for both GGA and LDA functionals. The GGA calculated values are consistently lower when compared to LDA, as expected. The predicted isentropic C_{ij}s are almost always greater than the isothermal values. The differences in magnitude of isothermal and isentropic C_{ij} becomes significant above $400\,\mathrm{K}$. The isentropic and isothermal stiffness constants C_{44}, C_{55}, and C_{66} are identical for the entire temperature range considered here.

Using C_{ij} and the corresponding elastic compliance S_{ij}, the bulk modulus (B), shear modulus (G), Poisson's ratio (ν) and Vicker's hardness (H_V) were computed and are shown in Table 4.3 at $0\,\mathrm{K}$ for $\mathrm{Ga_2O_3}$ using both the LDA and PBEsol (GGA) functionals.

Figure 4.13 shows the temperature dependencies of the elastic moduli computed quasistatically. None of the reported values exhibit significant temperature dependencies. For example, from $0\,K$ to $950\,K$ the bulk modulus only decreases about $10\,\mathrm{GPa}$ for LDA and

		B	G	E	ν	H_V
LDA	Voigt:	182	91	234	0.29	13.4
	Reuss:	179	83	216	0.30	12.2
	Hill:	180	87	225	0.29	12.8
GGA	Voigt:	168	86	222	0.28	12.7
	Reuss:	165	78	203	0.30	11.5
	Hill:	167	82	212	0.29	12.0
Measured (Ref. [74])				233		

Table 4.3: Calculated equilibrium values for bulk modulus B, shear modulus G, Young's modulus (E), Vicker's hardness (H_V), and Poisson's ratio (ν). All values determined by C_{ij} and are reported in GPa except the dimensionless ν.

	LDA			GGA		
	v_t	v_+	v_-	v_t	v_+	v_-
[100]	3.61 (2.87)	6.23 (6.48)	4.28 (3.88)	3.63 (2.47)	6.08 (6.32)	4.25 (3.84)
[010]	7.54 (7.51)	3.71 (3.64)	3.12 (2.02)	7.39 (7.27)	3.70 (3.59)	2.96 (1.96)
[001]	3.23 (2.86)	7.63 (7.15)	4.28 (3.61)	3.04 (2.72)	7.49 (7.09)	4.25 (3.39)

Table 4.4: Sound velocities in $\beta - \text{Ga}_2\text{O}_3$ along different crystallographic directions for the transverse (v_t), fast mixed mode (v_+), and slow mixed mode (v_-). Velocities are given in units of $\times 10^5$ cm/s. Comparisons to the lattice dynamical results extracted directly from the phonon dispersion are given in parentheses.

18 GPa for GGA. Comparing to Table 4.1, the temperature dependence of the bulk modulus using the QHA is noticeably larger, decreasing 15 GPa from 300K to 900K as opposed to the 7 GPa decline in the elastic stiffness approach.

Table 4.4 shows the sound velocities in $\beta - \text{Ga}_2\text{O}_3$ evaluated from the elastic constants along the crystallographic directions.[69] In all the three directions there is a pure transverse mode (v_t) and two mixed modes (v_+ and v_-). In the [100] and [001] directions v_t has the lowest velocity and the mixed v_+ mode has the highest. Only in the [010] direction does the transverse mode have the highest energy. A comparison with the sound velocities evaluated directly from lattice dynamical studies (phonon band structure) is also included for completeness.

The Debye temperature in Andersons's model [75] is evaluated from the average sound
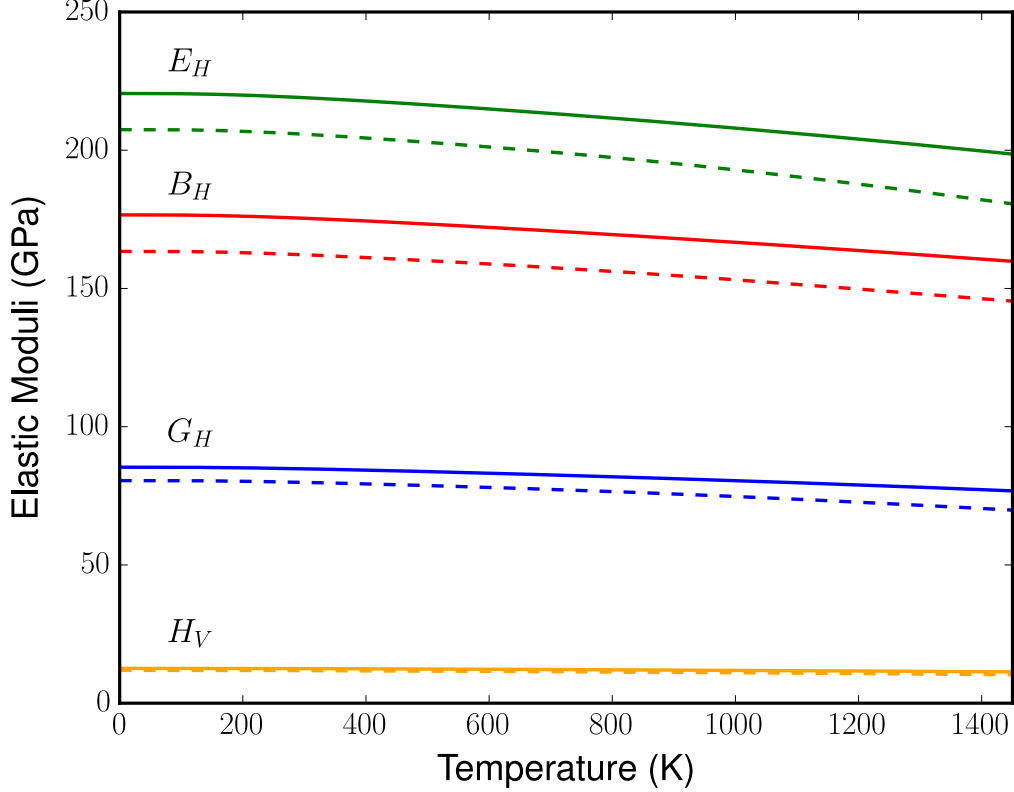
Figure 4.13: Temperature dependence of bulk moduli determined from computed elastic stiffness constants up to $1400\,K$.

	v_L	v_t	v_{avg}	Θ_D
LDA	6.95	3.77	4.21	$723\,\mathrm{K}$
GGA	6.79	3.70	4.13	$557\,\mathrm{K}$

Table 4.5: Calculated bulk sound velocity and computed Debye temperature (Θ_D). The longitudinal (v_L) and transverse mode (v_t) modes were averaged (v_{avg}) and used to compute Θ_D (K). Velocities are given in $\times 10^5$ cm/s.

velocity for both GGA and LDA calculations and is shown in Table 4.5. The average sound velocity was obtained from the longitudinal and transverse sound velocities which were evaluated from the elastic moduli.

4.2.2 Elastic Moduli $\alpha - \mathrm{Ga_2O_3}$

The α phase of $\mathrm{Ga_2O_3}$ has a simpler corundum symmetry and the mechanical properties are generally easier to compute. However very little is known about the mechanical properties

of this phase, with no estimates of the elastic properties at the time of this writing. It can be deduced however that the properties should resemble that of sapphire ($\alpha-\mathrm{Al_2O_3}$) which shares a crystal type. In addition to the shared crystal geometry, sapphire is the material used as a substrate for epitaxial layer growth of $\alpha - \mathrm{Ga_2O_3}$. The lattice mismatch between these structures is relatively low (4%) so it is natural to expect geometric properties such as anisotropy to be very similar between these structures. The elastic stiffness tensor of this structure is expressed generally as

$$
C_{ij}^{\mathrm{rho}} =
\begin{pmatrix}
c_{11} & c_{12} & c_{13} & c_{14} & 0 & 0 \\
 & c_{11} & c_{13} & -c_{14} & 0 & 0 \\
 & & c_{33} & 0 & 0 & 0 \\
 & & & c_{44} & 0 & 0 \\
 & & & & c_{44} & c_{14} \\
 & & & & & \frac{c_{11}-c_{12}}{2}
\end{pmatrix}
\tag{4.21}
$$

This tensor has only six independent components and the form is heavily dependent on the orientation of the crystallographic axes. The most common definition is that the z-axis is parallel to the rhombohedral [111] direction which is also equivalent to the c-axis in the hexagonal representation. In the LDA approximation, the elastic constants are computed and compared to sapphire in Table 4.6

	$\alpha - \mathrm{Ga_2O_3}$	$\alpha-\mathrm{Al_2O_3}$ [61]
C_{11}	364	497
C_{33}	325	493
C_{44}	93	154
C_{12}	128	165
C_{13}	101	129
C_{14}	8	19
B	180	249
G	113	155

Table 4.6: Calculated elastic stiffness (GPa) constants using LDA compared to $\alpha-\mathrm{Al_2O_3}$

Comparing to the monoclinic phase, the elastic constants are considerably larger. This is consistent with the decreased volume of the unit cell in the rhombohedral setting, leading

(a) (yz)-plane   (b) (xz)-plane   (c) (xy)-plane
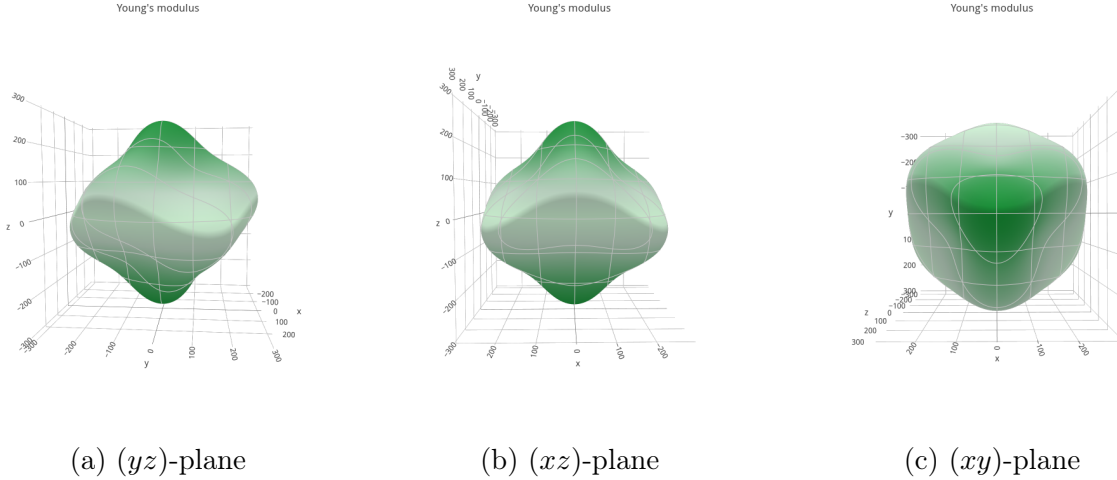
Figure 4.14: Tensor projection of Youngs modulus of Rhombohedral $\alpha - \mathrm{Ga_2O_3}$. Significantly lower anisotropy is seen compared to the monoclinic phase $\beta - \mathrm{Ga_2O_3}$

to a lower compressibility and subsequently higher bulk modulus. Additionally, there is a tighter packing of oxygen cations into the lattice for the α phase due to the hexagonal symmetry. Similar to the $\beta - \mathrm{Ga_2O_3}$ case, the Aluminum isostructure for the α phase shares the overall form however contains larger magnitudes and a larger bulk modulus. This is once again likely due to the smaller occupied volume of the unit cell. One interesting feature that is distinct is the value of C_{11}, which has the highest magnitude for the $\mathrm{Al_2O_3}$ case while $\alpha - \mathrm{Ga_2O_3}$ has a maximum value in the C_{33} constant. Additionally, the anisotropy is slightly different, with $\alpha - \mathrm{Ga_2O_3}$ containing a slightly larger anisotropy in the normal directions, i.e $C_{11}/C_{33} = 1.12$ for $\alpha - \mathrm{Ga_2O_3}$ and $C_{11}/C_{33} = 1.12$ for $\mathrm{Al_2O_3}$. Compared to the monoclinic phase however, the overall anisotropy is also reduced significantly in the 3D representation of the Youngs modulus, which can be seen in Figure 4.14

4.3 Optical Properties

Due to the large bandgap of $\beta - \mathrm{Ga_2O_3}$, there is significant interest in the optical properties which can be expected of the material. Characterizing these properties is considerably more complex for a material with large anisotropy as is the case for monoclinic crystals. The anisotropy of the crystal relates the optical properties to more complex phenomena such

as birefringence and double refraction, wherein electromagnetic waves of different character and velocity can simultaneously propagate through the same crystallographic direction. This leads to a range of possible refractive indices which depend on the direction of propagation. This relationship is often expressed as an ellipsoid which is oriented along the principal axes of the second-rank tensor (in this case, dielectric function) with the refractive indices being the semi-axes of the ellipsoid. This common representation of the index of refraction is referred to as the optical indicatrix and is generally a complicated construct to represent the anisotropy of any material property tensor [63]. This complexity is furthered extensively in situations where the already anistropic crystal is subjected to an external influence such as electric field or strain. However, the effect of geometry also has the potential to simplify the anisotropy of a material property in many cases which has been observed experimentally for thin-film $\beta - \text{Ga}_2\text{O}_3$ [60], where the tensor character of the dielectric function was reduced to an orthorhombic nature as the film width decreased. This shows the complexity of the indicatrix and the need to understand how the material properties will modulate under external influence. Strain in particular is an important parameter to consider due to the infancy of the growth methods and the likelihood of residual strain existing in the crystal post-growth. The effect of these residual strains can significantly influence the optical properties of a semiconductor which has been demonstrated in GaAs for example [76]. Experimentally this is a considerable challenge to characterize and measure.

4.3.1 Dielectric Function

The dielectric function is most commonly described by the sum of the real and imaginary parts

$$\varepsilon(\omega) = \varepsilon_1(\omega) + i\varepsilon_2(\omega) \tag{4.22}$$

where the imaginary part $\varepsilon_2(\omega)$ relates to the energy dissipation as a wave travels through the medium and the real part $\varepsilon_1(\omega)$ relates to the energy stored by the medium. As Ga_2O_3 belongs to the biaxial class of crystals, the dielectric tensor $\epsilon(\omega)$ has several principal

99

optical axes leading to birefringence. This has recently been reported on extensively[60] with particular emphasis placed on how the orientation of optical axes changes with respect to incident photon frequency. In the orientation used here the second rank dielectric tensor takes the form

$$\varepsilon(\omega) = \begin{pmatrix} \varepsilon_{xx} & 0 & \varepsilon_{xz} \\ 0 & \varepsilon_{yy} & 0 \\ \varepsilon_{xz} & 0 & \varepsilon_{zz} \end{pmatrix} \tag{4.23}$$

Several recent works have focused on how influential excitonic contributions to $\epsilon(\omega)$ may be in the visible frequency range. For the case of Ga_2O_3 there has been a sizable correction to the onset frequency when excitonic corrections are added to calculations.[77] These calculations require extensive computational resources and the influence of strain on the method's validity has not been investigated for even simple cases thus far, so they were not included in the current work. In the computations in this work the Drude-Lorentz model[63] was solved for the imaginary component of the dielectric function, ϵ_2 which entails the summing of transitions occurring between the unoccupied and occupied electronic states and is expressed as

$$\varepsilon_2(\omega) = \left(\frac{4\pi^2 e^2}{m\omega^2}\right) \sum_{ij} \int \langle i|M|j\rangle^2 f_i \left(1 - f_i\right) \times \delta \left(E_{j,k} - E_{i,k} - \omega\right) d^3k \tag{4.24}$$

where i is the initial state and j is the final state, f_i is the Fermi-Dirac distribution, and M is the dipole matrix. This is followed by the Kramers-Kronig transformation to determine the real part, ϵ_1:

$$\varepsilon_1(\omega) = 1 + \frac{2}{(\pi)} P \int_0^\infty \frac{\omega' \varepsilon_2 \left(\omega'\right) d\omega'}{\left(\omega'^2 - \omega^2\right)} \tag{4.25}$$

The imaginary part of dielectric function is evaluated within the LDA. The effect of temperature is not considered while analyzing the optical properties.
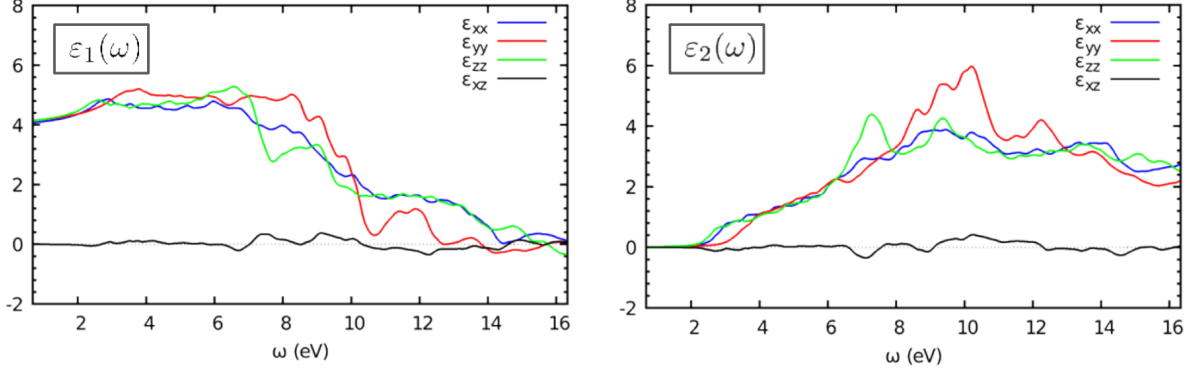
Figure 4.15: Computed Real (left) and imaginary (left) components of dielectric function of $\beta - \text{Ga}_2\text{O}_3$ without external strains

4.3.2 Normal Strain

The application of a normal strain does not reduce the overall symmetry of the crystal. The normal strain in the $\vec{x}$ for example is of the form,

$$\epsilon = \begin{pmatrix} \eta_{11} & 0 & 0 \\ 0 & 0 & 0 \\ 0 & 0 & 0 \end{pmatrix} \tag{4.26}$$

which transforms the lattice vectors as follows,

$$a = a_m(1 + \eta_{11}), \tag{4.27}$$

$$b = b_m \tag{4.28}$$

$$c = c_m\sqrt{1 + 2\eta_{11}\cos^2\beta_m + \eta_{11}^2\cos^2\beta_m}, \tag{4.29}$$

$$\cos\beta = \frac{(1 + \eta_{11})\cos\beta_m}{\sqrt{1 + 2\eta_{11}\cos^2\beta_m + \eta_{11}^2\cos^2\beta_m}} \tag{4.30}$$

The effect of these strains along the cartesian directions does not show a significant effect on the anisotropy or magnitude of the dielectric function even for relatively large strains of 0.75%. The results are summarized in Figure 4.16
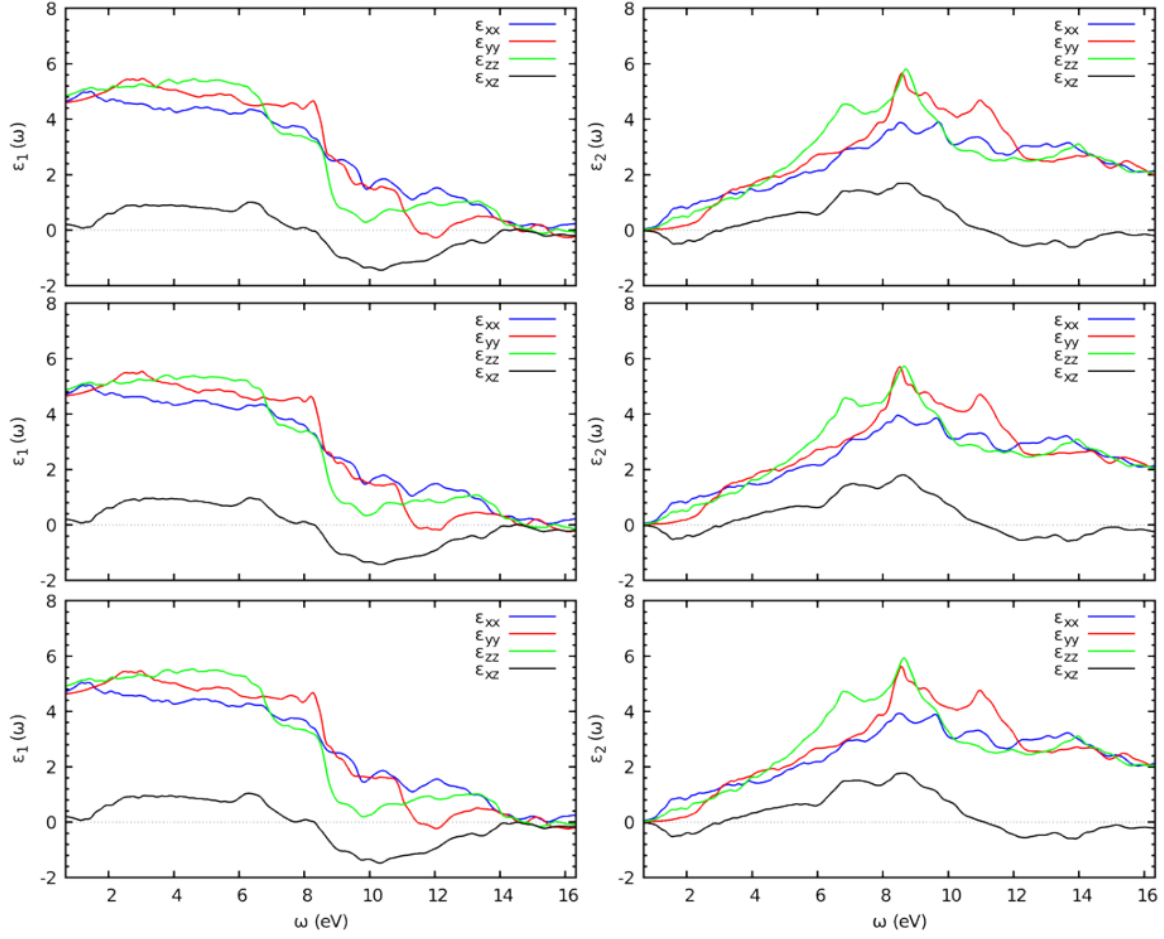
Figure 4.16: Dielectric function (real and imaginary) of $\beta - \text{Ga}_2\text{O}_3$ with normal external strains in the $\vec{x}$ (top), $\vec{y}$ (middle) and $\vec{z}$ (bottom) directions.

4.3.3 Shearing Strain

Applying strain in certain directions breaks the symmetry of the crystal and reduces the lattice to triclinic symmetry. For example a shearing strain in the xy-plane is of the form,

$$\eta = \begin{pmatrix} 0 & \eta_{12} & 0 \\ \eta_{12} & 0 & 0 \\ 0 & 0 & 0 \end{pmatrix} \tag{4.31}$$

which transform the lattice parameters as,

$$a = a_m \sqrt{1 + \eta_{12}^2},$$

$$b = \frac{1}{2} \sqrt{(a_m^2 + b_m^2)(1 + \eta_{12}^2) + 4\eta_{12}a_m b_m},$$

$$c = c_m \sqrt{1 + \eta_{12}^2 \cos^2 \beta_m},$$

$$\cos \alpha = \frac{\cos \beta_m (a_m(1 + \eta_{12}^2) + 2\eta_{12}b_m)}{\sqrt{1 + \eta_{12}^2 \cos^2 \beta_m} \sqrt{(a_m^2 + b_m^2)(1 + \eta_{12}^2) + 4\eta_{12}a_m b_m}}$$

$$\cos \beta = \frac{\cos \beta_m \sqrt{1 + \eta_{12}^2}}{\sqrt{1 + \eta_{12}^2 \cos^2 \beta_m}}$$

$$\cos \gamma = \frac{a_m(1 + \eta_{12}^2) + 2\eta_{12}b_m}{\sqrt{1 + \eta_{12}^2} \sqrt{(a_m^2 + b_m^2)(1 + \eta_{12}^2) + 4\eta_{12}a_m b_m}}$$

Specifically, the shearing strains produce non-negligible changes to the form of the dielectric tensor. This results in significant changes in anisotropy as seen in Figure 4.17.

In both the unstrained and strained cases the results are highly anisotropic and exhibit dichroism. However, unlike the unstrained situation, the strained configuration exhibits sizable dichroism at nearly steady-state frequencies.

4.3.4 Photo-elastic Effect

The strain-dependence of the anisotropy in the dielectric tensor is an important phenomena for a number of applications. For example, one of the more robust methods of characterizing detrimental extended defects which occur during crystal growth is by means of birefringence optical microscopy [78]. To quantitatively analyze using this method, knowledge of the photoelastic constants is necessary. The large strain dependence on optical properties also potentially opens up an unexplored application space for Ga_2O_3 in the field of acousto-optic modulator devices. These devices can be used to control power, frequency, and spatial directions of lasers by modification of the refractive index using acoustic waves. Recently, acousto-optic modulators have become more sophisticated and are included on-chip using integrated optics on materials such as lithium niobate ($LiNbO_3$). Devices of this nature
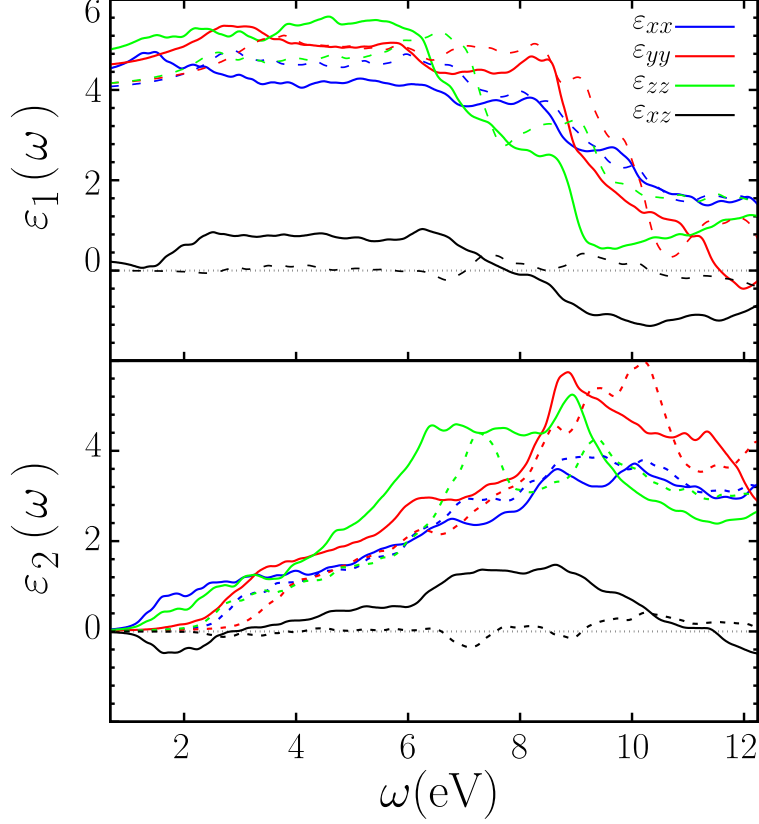
Figure 4.17: Dielectric function of $\beta-\mathrm{Ga_2O_3}$ with applied shearing strains (solid lines) along with the unstrained calculation (dashed lines). There is significantly increased anisotropy when strain is applied, increasing the brirefringence. The strongly fluctuating anisotropy with respect to frequency also indicates dichroism in the refractive index.

can be used in numerous ways such as tunable optical filters and optical switches. The response of the change in inverse dielectric function to strain is referred to as the elasto-optic, or photoelastic effect. It can be derived from the optical indicatrix ellipsoid mentioned previously by defining the impermeability B_{ij} and index of refraction n_{ij},

$$\frac{1}{B_{ij}} = \frac{1}{\varepsilon_{ij}} = \frac{1}{n_{ij}^2} \tag{4.32}$$

where index ellipsoid is written in the standard notation [63],

$$B_{ij} x_i x_j = 1 \tag{4.33}$$

The change in this impermeability gives rise to the photoelastic effect,

$$\Delta B_{ij} = \left(\varepsilon_{\eta_{kl}}^{-1}\right)_{ij} - \left(\varepsilon_0^{-1}\right)_{ij} = p_{ijkl}\eta_{kl} \tag{4.34}$$

The change in the inverse dielectric function can also be expressed by

$$\Delta \left(\frac{1}{\varepsilon}\right)_{ij} = -\frac{\Delta \varepsilon_{ij}}{\varepsilon_{ii}\varepsilon_{jj}} = \sum_{kl} p_{ijkl}\eta_{kl} \tag{4.35}$$

The full strained ellipsoid can now be expressed by

$$\left(B_{ij} + p_{ijkl}\eta_{kl}\right) x_i x_j = 1 \tag{4.36}$$

where η_{kl} is used to represent the strain vectors. Using this definition, the process of computing the photoelastic tensor p_{ijkl} is identical to that of the elastic tensor calculation except it is the stress response with the change in inverse dielectric function that is calculated. Due to the lack of symmetry in the photoelastic tensor in the monoclinic case, the full fourth-rank tensor p_{ijkl} is not easily represented using the more compact voigt notation. Here the most pronounced tensor elements of the unitless p_{ijkl} quantity which result in the largest modulation of dielectric properties is given. The response due to normal applied strain is overall the largest: $p_{1111} = 8 \times 10^{-2}$, $p_{2222} = -31 \times 10^{-2}$, $p_{3333} = -56 \times 10^{-2}$, $p_{1122} = -30 \times 10^{-2}$, $p_{1133} = -35 \times 10^{-2}$ and $p_{3322} = -27 \times 10^{-2}$.

Interestingly, the response due to shearing strains can be significant as well. The non-negligible values being $p_{1113} = 24 \times 10^{-2}$, $p_{2213} = 4 \times 10^{-2}$, $p_{3313} = -10 \times 10^{-2}$, and $p_{1333} = 7 \times 10^{-2}$. These sizable off-diagonal elements, especially p_{1113}, are expected as these strains correspond to symmetry breaking where the dielectric response should be more pronounced as was shown in Figure 4.17.

A material's performance for use in acousto-optical devices can be roughly estimated as a figure-of-merit (M) value.[79] This is essentially a measure of the fraction of light deflected at Bragg incidence and can be represented by

$$M = \frac{p_{\max}^2 n^6}{\rho v_{\mathrm{ac}}^3} \tag{4.37}$$

where n is the index of refraction, $p_{\max}$ is the maximum photoelastic tensor component, ρ is the density, and v_{ac} is the acoustic wave velocity. This value is often normalized to the value $M_0 = 1.51 \times 10^{-15}$ [79]. Utilizing these parameters as calculated and presented earlier,

the figure of merit is determined for Ga_2O_3 to be $M/M_0 = 6.72$. This compares well to the common acousto-optic material $LiNbO_3$ ($M/M_0 = 1.8$)[79] and demonstrates a promising and unexplored application space of $\beta - Ga_2O_3$ materials.

Another method of characterizing the effect of strain is by estimating the birefringence parameter. In general, birefringence stems from the polarization dependence of the refractive index and subsequently the optical axes of the index ellipsoid. The birefringence can be characterized by the expression for an angular rotation of the optical axis defined by

$$\tan 2\phi = \frac{2\varepsilon_{xz}}{\varepsilon_{xx} - \varepsilon_{zz}} \tag{4.38}$$

Using this expression, at DC ($\omega = 0$) the angle of optical axes from the principal axes is $\phi_{\text{unstrained}} \sim 7°$ while the application of a shearing strain increases this value to $\theta_{\text{sheared}} \sim 20°$. This demonstrates a significant dependence on strain even for DC frequencies. The orientation of the dielectric axes can play a significant role in polarization sensitive applications.

CHAPTER 5

CONCLUSION

This dissertation successfully characterized an array of thermal, elastic, and optical material properties of both $\beta - \text{Ga}_2\text{O}_3$ and $\alpha - \text{Ga}_2\text{O}_3$ using only first-principles techniques. This serves to validate the available measured data on these materials as well as predict properties which are not currently well understood experimentally. Additionally, this work sets a benchmark for the robustness of first-principles computation techniques in thermal transport of bulk and layered structures for materials of very low symmetry. In this chapter, the results of this work will be briefly summarized.

5.1 Summary

Both $\alpha - \text{Ga}_2\text{O}_3$ and $\beta - \text{Ga}_2\text{O}_3$ are ultra-wide bandgap semiconductors with very high breakdown fields that has seen applications in high power electronics as well as UV-transparent conductive films. The application space continues to grow especially for $\beta - \text{Ga}_2\text{O}_3$ devices, which has seen significant improvement in crystal growth quality and technique in recent years. Although the material claims many beneficial material properties and a wide bandgap, the low symmetry nature has led to a difficult to characterize anisotropy that is not well understood experimentally. This dissertation has performed a detailed analysis of the electronic structure using first-principles DFT calculations to resolve the bandstructure for both $\alpha - \text{Ga}_2\text{O}_3$ and $\beta - \text{Ga}_2\text{O}_3$ in the LDA, GGA, and hybrid functional frameworks. This leads to an accurate determination of bandgap and effective mass which agree well with measured data in both magnitude and anisotropy. The accurate electronic structure calculations then enabled the investigation of thermal properties, specifically thermal conductivity. It has been speculated for some time that the thermal conductivity will be the largest bottleneck in the development of more sophisticated Ga_2O_3 based devices. The value is very low (around 21 W/mK) compared to other wide bandgap semiconductors such as

GaN, diamond, or SiC and creates a thermal management issue in realistic applications such as on-chip power converters. Using the recently developed finite-displacement supercell approach, this work computes harmonic and anharmonic phonon properties such as phonon dispersion, phonon-phonon scattering rates, and thermal conductivity with no empirical inputs. The magnitude of thermal conductivity tensor was confirmed to be low as predicted from the limited measurements available ranging from 13-22 W/mK. The anisotropy is significant with a factor of 2 difference between the [100] and [010] crystallographic directions. The anisotropy was determined primarily to stem from a few different factors, primarily the importance of a non-negligible group velocity of optical phonon modes in the [010] direction, leading to an overall contribution of 44% of the total thermal conductivity in this direction. Additionally, the existence of an acousto-optical gap in the phonon dispersion along the [010] also limits the scattering phase space and thus increases thermal conductance. Additionally, $\alpha - Ga_2O_3$ was investigated briefly using the same first-principles methodology and was found to have an even lower thermal conductivity (around 10 W/mK) but more isotropic. The effect of the film thickness in the α phase was found to be relevant to thermal conductivity with a significant increase in thermal resistance due to boundary effects for films less than 100 nm.

Managing the poor thermal conductivity of Ga_2O_3 is a crucial issue to facilitate further refinement of Ga_2O_3 devices. One approach, which was explored extensively in this work, is by means of forming an effective thermal contact with some higher thermal conductivity material to act as a heat-sink. By using recently developed first-principles techniques combined with a variance-reduced Monte-Carlo solver, the thermal boundary conductance at a $Au/\beta - Ga_2O_3$ interface was computed and compared with the setups containing an adhesion layer composed of chromium or titanium to increase phonon transmission. The results matched very well with recent measurements and both chromium and titanium were determined to be effective thermal contact layers to increase the thermal boundary conductance significantly. Chromium had the maximum effect on thermal boundary conductance and

this is attributed to the high overlap in the phonon density of states with $\beta - \text{Ga}_2\text{O}_3$, which will lead to a higher phonon transmission within the diffuse mismatch model where only elastic mode conversions are allowed. More generally, this calculation serves as a benchmark for the VRMC method, and demonstrates the feasibility of the workflow for realistic device geometries.

Lastly, the effect of strain on the mechanical and optical properties was characterized. While the material continues to mature and growth methods become more refined, the effect that residual strains may have on the crystal is important to consider. In this work, the elastic stiffness tensor for both α and β phases were computed within a first-principles framework and the anisotropy of the tensor was evaluated. The results matched very well with recently measured results and the distinct anisotropy in the β phase was explained through the unique polyhedral linkage that is present from the existence of multiple coordination complexes among the cations that is not present in other crystals of similar symmetry. Furthermore, the quasiharmonic approximation is utilized which incorporated the phonon free-energy functions of multiple geometric configurations of varying volume. This allowed for an approximation for the temperature dependent elastic moduli to be determined and extended to the temperature dependence of the elastic stiffness constants. Finally, the dielectric function is computed as a function of frequency under a fully spanned set of strains for the crystal. The shearing strains produce a sizable modulation of anisotropy within the dielectric tensor due to the crystal symmetry breaking. This modulation was characterized by means of the photo-elastic tensor, which is then used to compute a figure-of-merit to determine the feasibility of $\beta - \text{Ga}_2\text{O}_3$ as an acousto-optic modulator device material. It was determined that the figure of merit of $\beta - \text{Ga}_2\text{O}_3$ is sizable and exceed that of lithium niobate, which is a workhorse material for acousto-optial materials.

5.2 Future Work

There are still many obstacles that will need to be overcome to facilitate further improvements in device design. From the results presented in this work, the most immediately useful topics to continue research on are outlined in this section. Firstly, while the thermal boundary conductance was determined to be large and overall the potential for $\beta - Ga_2O_3$ to form good thermal contacts is high, this does not alleviate the fact that within the bulk $\beta - Ga_2O_3$ material itself the thermal conductivity is quite low compared to the other WBG semiconducting materials. The self-heating issues will not be inherently solved solely by the inclusion of a good heatsink. It does however imply that by maximizing the area exposed to a heatsink and minimizing the overall layer thickness, there is likely to be a vastly improved over thermal performance of a $\beta - Ga_2O_3$ device structure. In the future, developing an improved Monte-Carlo algorithm allowing for a transient evaluation of temperature profiles would provide a more complete picture of the device geometries self-heating behavior. The next topic would be a more complete evaluation of the strain dependent index of refraction. Including not just the strain-dependent dielectric tensor in the form of the photo-elastic tensor. But by also computing the electro-optic tensor, which characterizes the response of the dielectric tensor to a static or low-frequency electric field. By computing these properties within a DFT framework, the electronic and phononic contributions can be isolated and the influence of phonons, the crystal structure, temperature, and bonding character between individual atoms can be weighted by their contributions to the optical properties of the crystal. Lastly, a topic which was not covered in this work, would be an evaluation of the electron-phonon scattering rates from first-principles. There has been preliminary evidence that polar optical phonon scattering is the dominant mechanism limiting electron mobility in $\beta - Ga_2O_3$ [80]. For example, the electron mobility is 10x lower than GaN while the effective mass is very similar. This was attributed to a large Frohlich interaction stemming from the low energy phonons. Detailing this interaction using a more complete theoretical model, using the electron-phonon wannier interoplation method, would be help isolate

the phonon modes most responsible for this limited mobility. Overall, significant progress is being made on the development of Ga_2O_3 technologies and the work presented in this dissertation serves to provide a more fundamental understanding of the underlying material properties and what bottlenecks must still be overcome in the future.

BIBLIOGRAPHY

BIBLIOGRAPHY

[1] JY Tsao, S Chowdhury, MA Hollis, D Jena, NM Johnson, KA Jones, RJ Kaplar, S Rajan, CG Van de Walle, E Bellotti, et al. Ultrawide-bandgap semiconductors: Research opportunities and challenges. *Advanced Electronic Materials*, 2017.

[2] Masataka Higashiwaki, Kohei Sasaki, Hisashi Murakami, Yoshinao Kumagai, Akinori Koukitu, Akito Kuramata, Takekazu Masui, and Shigenobu Yamakoshi. Recent progress in Ga_2O_3 power devices. *Semiconductor Science and Technology*, 31(3):034001, 2016.

[3] JB Varley, Anderson Janotti, Cesare Franchini, and Chris G Van de Walle. Role of self-trapping in luminescence and p-type conductivity of wide-band-gap oxides. *Physical Review B*, 85(8):081109, 2012.

[4] A Segura, Lluís Artús, Ramón Cuscó, R Goldhahn, and M Feneberg. Band gap of corundumlike α- ga 2 o 3 determined by absorption and ellipsometry. *Physical Review Materials*, 1(2):024604, 2017.

[5] Kentaro Kaneko, Shizuo Fujita, and Toshimi Hitora. A power device material of corundum-structured α-ga2o3 fabricated by mist epitaxy ® technique. *Japanese Journal of Applied Physics*, 57(2S2):02CB18, 2018.

[6] SJ Pearton, Jiancheng Yang, Patrick H Cary IV, F Ren, Jihyun Kim, Marko J Tadjer, and Michael A Mastro. A review of ga2o3 materials, processing, and devices. *Applied Physics Reviews*, 5(1):011301, 2018.

[7] A. Togo, F. Oba, and I. Tanaka. First-principles calculations of the ferroelastic transition between rutile-type and $CaCl_2$-type SiO_2 at high pressures. *Phys. Rev. B*, 78:134106, Oct 2008.

[8] Paolo Giannozzi et al. Quantum espresso: a modular and open-source software project for quantum simulations of materials. *J. Phys.: Condensed Matter*, 21(39), 2009.

[9] Hartwin Peelaers and Chris G. Van de Walle. Brillouin zone and band structure of $\beta - Ga_2O_3$. *physica status solidi (b)*, 252(4):828–832, 2015.

[10] Kristina E Lipinska-Kalita, Patricia E Kalita, Oliver A Hemmers, and Thomas Hartmann. Equation of state of gallium oxide to 70 gpa: Comparison of quasihydrostatic and nonhydrostatic compression. *Physical Review B*, 77(9):094123, 2008.

[11] Richard M Martin. *Electronic structure: basic theory and practical methods*. Cambridge university press, 2004.

[12] Zbigniew Galazka et al. On the bulk $\beta - Ga_2O_3$ single crystals grown by the czochralski method. *J. Cryst. Growth*, 404(0):184 – 191, 2014.

[13] Julia E Medvedeva and Chaminda L Hettiarachchi. Tuning the properties of complex transparent conducting oxides: Role of crystal symmetry, chemical composition, and carrier generation. *Physical Review B*, 81(12):125116, 2010.

[14] J Furthmüller and F Bechstedt. Quasiparticle bands and spectra of ga 2 o 3 polymorphs. *Physical Review B*, 93(11):115204, 2016.

[15] Haiying He, Roberto Orlando, Miguel A Blanco, Ravindra Pandey, Emilie Amzallag, Isabelle Baraille, and Michel Rérat. First-principles study of the structural, electronic, and optical properties of ga 2 o 3 in its monoclinic and hexagonal phases. *Physical Review B*, 74(19):195123, 2006.

[16] Joachim Paier, Martijn Marsman, K Hummer, Georg Kresse, Iann C Gerber, and János G Ángyán. Screened hybrid density functionals applied to solids. *The Journal of chemical physics*, 124(15):154709, 2006.

[17] Jong-Won Song, Koichi Yamashita, and Kimihiko Hirao. Communication: A new hybrid exchange correlation functional for band-gap calculations using a short-range gaussian attenuation (gaussian-perdue–burke–ernzerhof), 2011.

[18] Lucy D Whalley, Jarvist M Frost, Benjamin J Morgan, and Aron Walsh. Impact of non-parabolic electronic band structure on the optical and transport properties of photovoltaic materials. *arXiv preprint arXiv:1811.02281*, 2018.

[19] Sean Knight, Alyssa Mock, Rafał Korlacki, Vanya Darakchieva, Bo Monemar, Yoshinao Kumagai, Ken Goto, Masataka Higashiwaki, and Mathias Schubert. Electron effective mass in sn-doped monoclinic single crystal β-gallium oxide determined by mid-infrared optical hall effect. *Applied Physics Letters*, 112(1):012103, 2018.

[20] Zhi Guo, Amit Verma, Xufei Wu, Fangyuan Sun, Austin Hickman, Takekazu Masui, Akito Kuramata, Masataka Higashiwaki, Debdeep Jena, and Tengfei Luo. Anisotropic thermal conductivity in single crystal β-gallium oxide. *Applied Physics Letters*, 106(11):111909, 2015.

[21] Z. Galazka M. Handwerg, R. Mitdank and S.F. Fischer. Temperature-dependent thermal conductivity in mg-doped and undoped ga2o3 bulk-crystals. *Semi. Sci. and Tech.*, 30(2), 2015.

[22] Encarnación G. Víllora, Kiyoshi Shimamura, Takekazu Ujiie, and Kazuo Aoki. Electrical conductivity and lattice expansion of ga2o3 below room temperature. *Applied Physics Letters*, 92(20), 2008.

[23] G. P. Srivastava H. M. Tutuncu, Subhash L. Shinde. *Length-Scale Dependent Phonon Interactions*. Topics in Applied Physics 128. Springer-Verlag New York, 1 edition, 2014.

[24] Wu Li, Jesús Carrete, Nebil A. Katcho, and Natalio Mingo. Shengbte: A solver of the boltzmann transport equation for phonons. *Comp. Phys. Comm.*, 185(6):1747 – 1758, 2014.

[25] Alistair Ward. *First principles theory of the lattice thermal conductivity of semiconductors.* PhD thesis, Boston College, 2009.

[26] Keivan Esfarjani and Harold T. Stokes. Method to extract anharmonic force constants from first principles calculations. *Phys. Rev. B*, 77:144112, Apr 2008.

[27] A. Ward and D. A. Broido. Intrinsic phonon relaxation times from first-principles studies of the thermal conductivities of si and ge. *Phys. Rev. B*, 81:085205, Feb 2010.

[28] Ruiqiang Guo, Xinjiang Wang, and Baoling Huang. Thermal conductivity of skutterudite cosb3 from first principles: Substitution and nanoengineering effects. *Sci. Rep.*, 5, Jan 2015.

[29] L Lindsay, DA Broido, and TL Reinecke. Thermal conductivity and large isotope effect in gan from first principles. *Physical review letters*, 109(9):095901, 2012.

[30] Mitsuaki Kawamura, Yoshihiro Gohda, and Shinji Tsuneyuki. Improved tetrahedron method for the brillouin-zone integration applicable to response functions. *Physical Review B*, 89(9):094515, 2014.

[31] Marco D. Santia, Nandan Tandon, and J. D. Albrecht. Lattice thermal conductivity in β-ga2o3 from first principles. *Applied Physics Letters*, 107:041907, 2015.

[32] P. E. Blöchl. Projector augmented-wave method. *Phys. Rev. B*, 50(0):17953–17979, 1994.

[33] J. P. Perdew, K. Burke, and M. Ernzerhof. Generalized gradient approximation made simple. *Phys. Rev. Lett.*, 77(0):3865–3868, 1996.

[34] S. Geller. Crystal Structure of Ga_2O_3. *J. Chem. Phys.*, 33:676–684, September 1960.

[35] S. Baroni, S. de Gironcoli, and A. D. Corso. Phonons and related crystal properties from density-functional perturbation theory. *Rev. Mod. Phys.*, 73:515–562, 2001.

[36] J. M. Ziman. *Electrons and phonons : the theory of transport phenomena in solids.* Clarendon Press Oxford University Press, Oxford New York, 2001.

[37] Aleksandr Chernatynskiy and Simon R. Phillpot. Phonon transport simulator (phonts). *Comp. Phys. Comm.*, 192(0):196 – 204, 2015.

[38] L. Lindsay and T. L. Reinecke. Three-phonon phase space and lattice thermal conductivity in semiconductors. *J. Phys.: Condens. Matter*, 20(0):165209, 2008.

[39] Tianli Feng and Xiulin Ruan. Prediction of spectral phonon mean free path and thermal conductivity with applications to thermoelectrics and thermal management: A review. *J. Nanomaterials*, 2014:1–25, 2014.

[40] J. B. Varley, J. R. Weber, A. Janotti, and C. G. Van de Walle. Oxygen vacancies and donor impurities in ga2o3. *Appl. Phys. Lett.*, 97(14), 2010.

[41] Encarnación G. Víllora, Kiyoshi Shimamura, Yukio Yoshikawa, Takekazu Ujiie, and Kazuo Aoki. Electrical conductivity and carrier concentration control in ga2o3 by si doping. *Appl. Phys. Lett.*, 92(20), 2008.

[42] H. Aller, X. Yu, A. J. Gellman, J. A. Malen, and A. J. H. McGaughey. Thermal conductance of ga2o3/metal interfaces. In *2018 17th IEEE Intersociety Conference on Thermal and Thermomechanical Phenomena in Electronic Systems (ITherm)*, pages 567–571, May 2018.

[43] Adam J. Jackson and Aron Walsh. Oxidation of gan: An *ab initio* thermodynamic approach. *Phys. Rev. B*, 88:165201, Oct 2013.

[44] Marco Arrigoni and Georg KH Madsen. Comparing the performance of lda and gga functionals in predicting the lattice thermal conductivity of iii-v semiconductor materials in the zincblende structure: The cases of alas and bas. *Computational Materials Science*, 156:354–360, 2019.

[45] Jesús Carrete, Bjorn Vermeersch, Ankita Katre, Ambroise van Roekeghem, Tao Wang, Georg KH Madsen, and Natalio Mingo. almabte: A solver of the space–time dependent boltzmann transport equation for phonons in structured materials. *Computer Physics Communications*, 220:351–362, 2017.

[46] Seung Hyun Lee, Kang Min Lee, Young-Bin Kim, Yoon-Jong Moon, Soo Bin Kim, Dukkyu Bae, Tae Jung Kim, Young Dong Kim, Sun-Kyung Kim, and Sang Woon Lee. Sub-microsecond response time deep-ultraviolet photodetectors using α-ga2o3 thin films grown via low-temperature atomic layer deposition. *Journal of Alloys and Compounds*, 2018.

[47] Jean-Philippe M Péraud, Colin D Landon, and Nicolas G Hadjiconstantinou. Monte carlo methods for solving the boltzmann transport equation.

[48] Patrick E Hopkins, Pamela M Norris, and Robert J Stevens. Influence of inelastic scattering at metal-dielectric interfaces. *Journal of Heat Transfer*, 130(2):022401, 2008.

[49] Minyoung Jeong, Justin P Freedman, Hongliang Joe Liang, Cheng-Ming Chow, Vincent M Sokalski, James A Bain, and Jonathan A Malen. Enhancement of thermal conductance at metal-dielectric interfaces using subnanometer metal adhesion layers. *Physical Review Applied*, 5(1):014009, 2016.

[50] Brian F Donovan, Chester J Szwejkowski, John C Duda, Ramez Cheaito, John T Gaskins, C-Y Peter Yang, Costel Constantin, Reese E Jones, and Patrick E Hopkins. Thermal boundary conductance across metal-gallium nitride interfaces from 80 to 450 k. *Applied Physics Letters*, 105(20):203502, 2014.

[51] Tianli Feng, Lucas Lindsay, and Xiulin Ruan. Four-phonon scattering significantly reduces intrinsic thermal conductivity of solids. *Physical Review B*, 96(16):161201, 2017.

[52] Krishnendu Ghosh and Uttam Singisetti. Calculation of electron impact ionization coefficient in β-Ga$_2$O$_3$. In *72nd Device Research Conference*. Institute of Electrical & Electronics Engineers (IEEE), June 2014.

[53] Antonella Parisini and Roberto Fornari. Analysis of the scattering mechanisms controlling electron mobility in β-Ga$_2$O$_3$ crystals. *Semiconductor Science and Technology*, 31(3):035023, 2016.

[54] Fabio Orlandi, Francesco Mezzadri, Gianluca Calestani, Francesco Boschi, and Roberto Fornari. Thermal expansion coefficients of β-Ga$_2$O$_3$ single crystals. *Applied Physics Express*, 8(11):111101, 2015.

[55] Wolfram Miller, Klaus Böttcher, Zbigniew Galazka, and Jürgen Schreuer. Numerical modelling of the czochralski growth of ga2o3. *Crystals*, 7(1), 2017.

[56] Yuichi Oshima, Elaheh Ahmadi, Stefan C. Badescu, Feng Wu, and James S. Speck. *Applied Physics Express*, 9(6):061102, 2016.

[57] Rostam Golesorkhtabar, Pasquale Pavone, Jürgen Spitaler, Peter Puschnig, and Claudia Draxl. Elastic: A tool for calculating second-order elastic constants from first principles. *Computer Physics Communications*, 184(8):1861 – 1873, 2013.

[58] Y Wang, J J Wang, H Zhang, V R Manga, S L Shang, L-Q Chen, and Z-K Liu. A first-principles approach to finite temperature elastic constants. *Journal of Physics: Condensed Matter*, 22(22):225404, 2010.

[59] Daoyou Guo, Zhenping Wu, Peigang Li, Yuehua An, Han Liu, Xuncai Guo, Hui Yan, Guofeng Wang, Changlong Sun, Linghong Li, and Weihua Tang. Fabrication of β-ga2o3 thin films and solar-blind photodetectors by laser mbe technology. *Opt. Mater. Express*, 4(5):1067–1076, May 2014.

[60] Chris Sturm and Marius Grundmann. Singular optical axes in biaxial crystals and analysis of their spectral dispersion effects in $\beta - ga_2o_3$. *Phys. Rev. A*, 93:053839, May 2016.

[61] Shunli Shang, Yi Wang, and Zi-Kui Liu. First-principles elastic constants of α- and θ-al$_2$o$_3$. *Applied Physics Letters*, 90(10), 2007.

[62] Shun-Li Shang, Hui Zhang, Yi Wang, and Zi-Kui Liu. Temperature-dependent elastic stiffness constants of α- and θ-al$_2$o$_3$ from first-principles calculations. *Journal of Physics: Condensed Matter*, 22(37):375403, 2010.

[63] J. F. Nye. *Physical properties of crystals : their representation by tensors and matrices*. Clarendon Press Oxford University Press, 1985.

[64] R. Yu, J. Zhu, and H.Q. Ye. Calculations of single-crystal elastic constants made simple. *Computer Physics Communications*, 181(3):671 – 675, 2010.

[65] Marco D. Santia, Nandan Tandon, and J. D. Albrecht. Thermal properties of β-ga2o3 from first principles. *MRS Advances*, 1:109–114, 1 2016.

[66] Gene Simmons. *Single Crystal Elastic Constants and Calculated Aggregate Properties: A Handbook.* M.I.T. Press, Cambridge, Mass, 1971.

[67] Per Söderlind and John E. Klepeis. First-principles elastic properties of α-Pu. *Phys. Rev. B*, 79:104110, Mar 2009.

[68] Xue Jiang, Jijun Zhao, and Xin Jiang. Correlation between hardness and elastic moduli of the covalent crystals. *Computational Materials Science*, 50(7):2287 – 2290, 2011.

[69] J. Feng, B. Xiao, R. Zhou, and W. Pan. Anisotropy in elasticity and thermal conductivity of monazite-type {REPO4} (re = la, ce, nd, sm, eu and gd) from first-principles calculations. *Acta Materialia*, 61(19):7364 – 7383, 2013.

[70] K Adachi, H Ogi, N Takeuchi, N Nakamura, H Watanabe, T Ito, and Y Ozaki. Unusual elasticity of monoclinic β- ga 2 o 3. *Journal of Applied Physics*, 124(8):085102, 2018.

[71] G.F. Davies. Effective elastic moduli under hydrostatic stress—i. quasi-harmonic theory. *Journal of Physics and Chemistry of Solids*, 35(11):1513 – 1520, 1974.

[72] Yingchun Ding and Bing Xiao. Anisotropic elasticity, sound velocity and thermal conductivity of tio2 polymorphs from first principles calculations. *Computational Materials Science*, 82:202 – 218, 2014.

[73] Kristina E. Lipinska-Kalita, Patricia E. Kalita, Oliver A. Hemmers, and Thomas Hartmann. Equation of state of gallium oxide to 70 GPa: Comparison of quasihydrostatic and nonhydrostatic compression. *Phys. Rev. B*, 77:094123, Mar 2008.

[74] VI Nikolaev, V Maslov, SI Stepanov, AI Pechnikov, V Krymov, IP Nikitina, LI Guzilova, VE Bougrov, and AE Romanov. Growth and characterization of β-ga2o3 crystals. *Journal of Crystal Growth*, 457:132–136, 2017.

[75] Orson L. Anderson. A simplified method for calculating the debye temperature from elastic constants. *Journal of Physics and Chemistry of Solids*, 24(7):909 – 917, 1963.

[76] M Herms, M Fukuzawa, M Yamada, J Klöber, G Zychowitz, and JR Niklas. Photoelastic characterization of residual strain in gaas wafers annealed in holders of different geometry. *Materials Science and Engineering: B*, 66(1-3):7–10, 1999.

[77] Kelsey A. Mengle, Guangsha Shi, Dylan Bayerl, and Emmanouil Kioupakis. First-principles calculations of the near-edge optical properties of β-ga2o3. *Applied Physics Letters*, 109(21):212104, 2016.

[78] S Mendelson. Dislocations and plastic flow in nacl single crystals. i. *Journal of Applied Physics*, 33(7):2175–2181, 1962.

[79] D Royer. *Elastic Waves in Solids.* Springer, Berlin New York, 2000.

[80] Nan Ma, Nicholas Tanen, Amit Verma, Zhi Guo, Tengfei Luo, Huili Xing, and Debdeep Jena. Intrinsic electron mobility limits in β-ga2o3. *Applied Physics Letters*, 109(21):212101, 2016.